Materials Design toward High Performance Electrodes for Advanced Energy Storage Applications

Author: Qingmei Cheng

Boston College

The Graduate School of Arts and Sciences

Department of Chemistry

MATERIALS DESIGN TOWARD HIGH PERFORMANCE ELECTRODES FOR ADVANCED ENERGY STORAGE APPLICATIONS

a dissertation

by

QINGMEI CHENG

submitted in partial fulfillment of the requirements

for the degree of

Doctor of Philosophy

August 2018 of graduation

Materials Design toward High Performance Electrodes for Advanced Energy Storage Applications

A Dissertation by Qingmei Cheng

Dissertation Advisor: Prof. Dunwei Wang

Abstract

Rechargeable batteries, especially lithium ion batteries, have greatly transformed mobile electronic devices nowadays. Due to the ever-depletion of fossil fuel and the need to reduce CO_2 emissions, the development of batteries needs to extend the success in small electronic devices to other fields such as electric vehicles and large-scale renewable energy storage. Li-ion batteries, however, even when fully developed, may not meet the requirements for future electric vehicles and grid-scale energy storage due to the inherent limitations related with intercalation chemistry. As such, alternative battery systems should be developed in order to meet these important future applications. This dissertation presents our successes in improving Li-O_2 battery performance for electric vehicle application and integrating a redox flow battery into a photoelectrochemical cell for direct solar energy storage application.

Li-O_2 batteries have attracted much attention in recent years for electric vehicle application since it offers much higher gravimetric energy density than Li-ion ones. However, the development of this technology has been greatly hindered by the poor cycling performance. The key reason is the instability of carbon cathode under operation conditions. Our strategy is to protect the carbon

cathode from reactive intermediates by a thin uniform layer grown by atomic layer depostion. The protected electrode significantly minimized parasitic reactions and enhanced cycling performance. Furthermore, the well-defined pore structures in our carbon electrode also enabled the fundamental studies of cathode reactions.

Redox flow batteries (RFB), on the other hand, are well-suited for large-scale stationary energy storage in general, and for intermittent, renewable energy storage in particular. The efficient capture, storage and dispatch of renewable solar energy are major challenges to expand solar energy utilization. Solar rechargeable redox flow batteries (SRFBs) offer a highly promising solution by directly converting and storing solar energy in a RFB with the integration of a photoelectrochemical cell. One major challenge in this field is the low cell open-circuit potential, mainly due to the insufficient photovoltages of the photoelectrode systems. By combining two highly efficient photoelectrodes, Ta_3N_5 and Si (coated with GaN), we show that a high-voltage SRFB could be unassistedly photocharged and discharged with a high solar-to-chemical efficiency.

Table of Contents

Acknowledgement

First of all, I owe my deepest thanks to my advisor, Prof. Dunwei Wang, for his continuous guidance and support during all of my Ph.D. study. His passion for science, insightful view and hard-working attitude has been really inspiring and helpful. He is a great mentor who has helped me tremendously to overcome difficulties and improve myself with his patience, challenges and encouragements.

Besides, I want to thank Prof. Chia-Kuang (Frank) Tsung, Prof. Udayan Mohanty and Prof. Matthias Waegele for being my committee members. Thank you for taking time and providing constructive suggestions for this dissertation. Specially, I want to thank Prof. Frank Tsung and Prof. Udayan Mohanty for their advice and support during my qualification exam.

I also would like to acknowledge Prof. Wei Fan, Prof. Zetian Mi, Prof. Pratap Rao, Prof. Kenneth Burch and members in their groups for their insightful discussions and tremendous help in our collaborative projects. I want to acknowledge all the administrative and technical staffs in the Chemistry Department, Physics Department and the Integrated Sciences Cleanroom and Nanofabrication Facility of Boston College for their help with my projects. Additionally, I also thank Harvard CNS and the MIT CMSE for their shared facilities.

Next, I am grateful for tremendous help from all of the members in Wang Group during the past five years. Dr. Jin Xie and Dr. Xiahui Yao were mentors who guided me through battery field. I have learned so much from them about how to be a good researcher. Prof. Weiqiang Fan helped me incredibly in the solar rechargeable redox battery project. Da He, James Thorne and Yumin He offered much help to gain my knowledge and perform experiments in photoelectrochemistry field. I would like to thank Qi Dong, Haochuan Zhang, Bryan McCloskey and Ian Madden, who have worked very closely with me and made enormous contributions to my projects. Also, I want to thank all other current and former group members, including Wei Li, Jingru Luo, Yanyan Zhao, Mengdi Liu, Chaochao Lang, Bingju Zhong, Xiaolin Tao, Elizabeth Pastrana Alta, Prof. Pengcheng Dai, Dr. Chun Du, Prof. Ji-Wook Jang, Prof. Peiyan Ma, Prof. Song Li, Prof. Hongye Bai, Shasha Zhu and Xin Ba, for their help and insightful discussions during the years.

Additionally, I appreciate all the help from my colleagues in Boston College. I wish to extend my gratitude to my friends I met here in Boston and all my old friends for their continous support and encouragement.

In the end, I would like to thank my beloved family for their unconditional support and love over the years. Your constant encouragement and trust motivates me most in my life.

Chapter 1 Introduction

1.1 Rechargeable Batteries

Rechargeable batteries are indispensible in many fields for a large variety of applications such as mobile electronics, electrical vehicles, grid-scale levelling, and large-scale electricity storage for renewable energy sources (**Figure 1.1**).[1] As an electrochemical energy storage device, rechargeable batteries are able to store electrical energy as chemical energy during charging which could be reversibly converted back to electricity during discharging.[2]

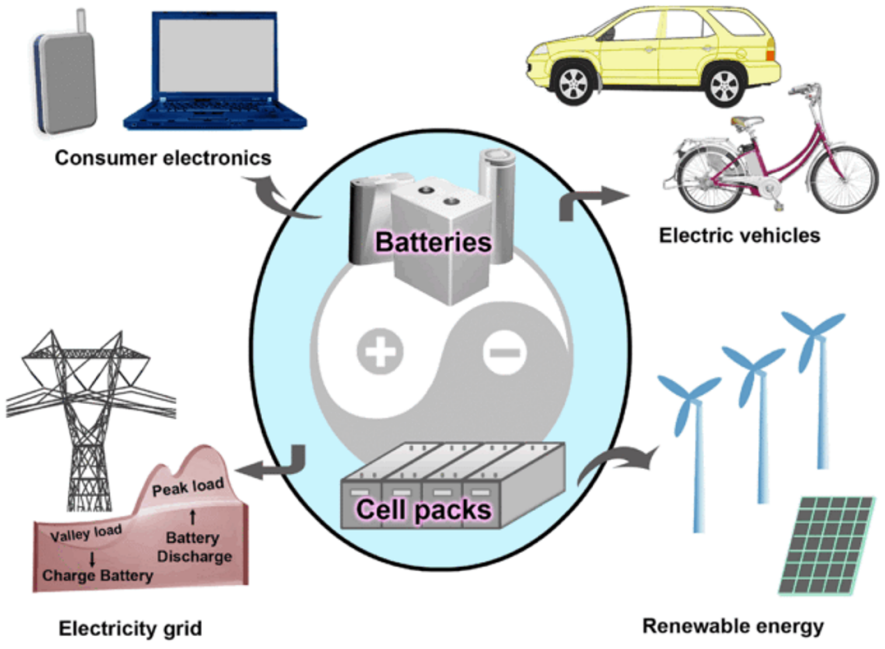

Figure 1.1 Representative applications of rechargeable batteries. Reproduced with permission from Ref. [1]. Copyright 2011 Wiley-VCH.

A battery typically has three major components: the anode, the cathode and the electrolyte. During discharging, the anode active material is oxidized and the cathode active material is reduced. When connected to an external load, electrons flow from the anode through the external load to the cathode, while the movement of ions in the electrolyte completes the electric circuit to generate electricity. During charging, the process is reversed by connecting to an external power supply.

The performance of rechargeable batteries can be evaluated by several key parameters:[3]

- Gravimetric energy density (E_m, Wh/kg): discharge energy output per unit mass

$$E_m = \int_0^t IV\, dt/m$$

- Power density (P_m, W/kg): discharge power output per unit mass

$$P_m = IV/m$$

- Capacity (C, Ah): discharge energy in ampere-hours at a certain rate

$$\mathrm{C} = \int_0^t I\, dt$$

- Round-trip efficiency: ratio of discharge energy output and charge energy input

$$\eta = \frac{E_{discharge}(Wh)}{E_{charge}\,(Wh)} \times 100\%$$

- Cycle lifetime: numbers of cycles before a battery fails to deliver certain percentage of its initial capacity

Up to now, the wide application of rechargeable batteries such as Li-ion batteries has already greatly transformed the way people power mobile electronics. However, state-of-

the-art Li-ion batteries may not be the best option for other applications such as electric vehicles and grid-scale energy storage. For example, the theoretical energy density of Li-ion batteries is too low to meet the future electric vehicles' range demand per charge (e.g. 500 miles).[4] In addition, the relatively high cost, short lifetime as well as safety concerns of Li-ion batteries is hindering their application for grid-scale energy storage.[5] Thus alternative rechargeable batteries such as lithium oxygen batteries[6] and redox flow batteries[7] should be developed to meet the future demands for battery applications. A brief overview of current understandings of lithium oxygen batteries and redox flow batteries is provided next.

1.1.1 Lithium Oxygen Batteries

Societal demand for high-energy-density battery technologies for applications such as long-range electric vehicles are growing rapidly in order to retard fossil fuel depletion, eradicate exhaust pollution and reduce CO_2 emissions. Lithium oxygen battery is one of the most promising candidates since it has the highest theoretical energy density (3505 Wh/kg) compared with other available battery chemistries.[4] Practical energy densities in the range of 500 Wh/kg-1000 Wh/kg are proposed, which are still about 2-3 times higher than today's Li-ion batteries (**Figure 1.2**).[8]

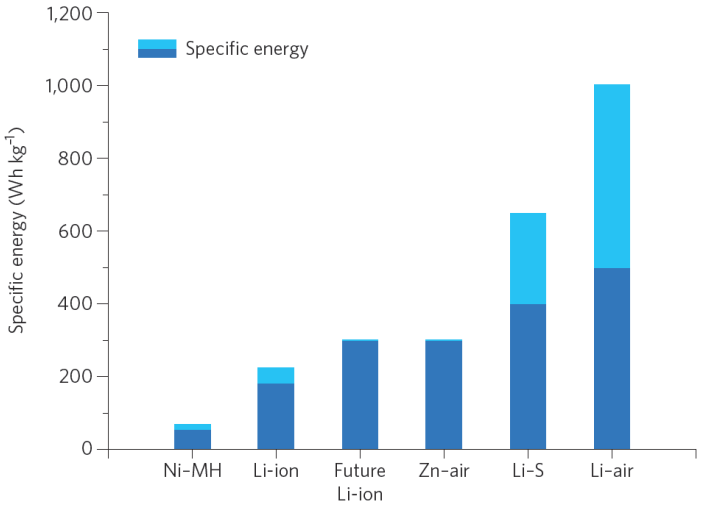

Figure 1.2 Practical specific energy density for several representative rechargeable batteries. Reproduced with permission from Ref. [8]. Copyright 2016 NPG.

The schematic operation of a non-aqueous Li-O_2 battery is shown in **Figure 1.3**.[9] It is composed of Li metal anode, aprotic Li^+ conducting electrolyte and O_2 cathode. The fundamental chemistry involves Li metal dissolution and deposition on the anode side and O_2 reduction reaction (ORR) and O_2 oxidation reaction (OER) on the cathode side. The electrochemical reactions on both electrodes are shown as following, generating a theoretical cell voltage of 2.96 V.

Anode: $$Li - e^- \underset{charge}{\overset{discharge}{\rightleftharpoons}} Li^+ \qquad (E^0 = -3.04\,V\ vs.SHE)$$

Cathode: $$2Li^+ + 2e^- + O_2 \underset{charge}{\overset{discharge}{\rightleftharpoons}} Li_2O_2 \qquad (E^0 = -0.08\,V\ vs.SHE)$$

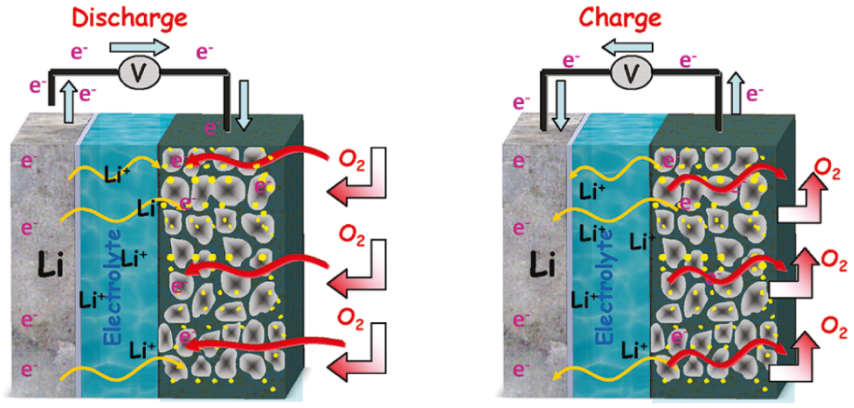

Figure 1.3 Schematic operation of Li-O_2 batteries. Reproduced with permission from Ref. [9]. Copyright 2010 ACS.

While progress has been made in recent years, there are still many challenges associated with the major components of Li-O_2 batteries (**Figure 1.4**).[10] Li metal anode has attracted much attention in recent years, owing to the much higher gravimetric capacity of Li (3861 mAh/g_{Li}; $Li^+ + e^- \rightarrow Li$) compared to conventional intercalation anode materials such as carbon (372 mAh/g_c; $Li^+ + C_6 + e^- \rightarrow LiC_6$) in Li-ion batteries.[11] However, Li dendrite formation during repeated Li dissolution and deposition and the resulting safety issues are greatly hindering the application of Li metal anode.[12] As the key component of Li-O_2 batteries, O_2 cathode suffers from high recharge overpotential, poor rate capability and short cycle lifetime. One important reason is the poor kinetics of Li_2O_2 formation and decomposition resulted from the insulating nature of Li_2O_2.[13] What's worse, the high recharge overpotential would further induce the decomposition of both electrolyte and cathode materials, which results in significant formation of byproducts and overall cell

failure eventually.[14] In addition to the above issues, another critical issue is the instability of electrolyte and cathode towards the reduced oxygen species which are produced unavoidably during the operation of Li-O_2 batteries. As a result, Li-O_2 batteries which could be cycled for more than a few hundred cycles are rare.

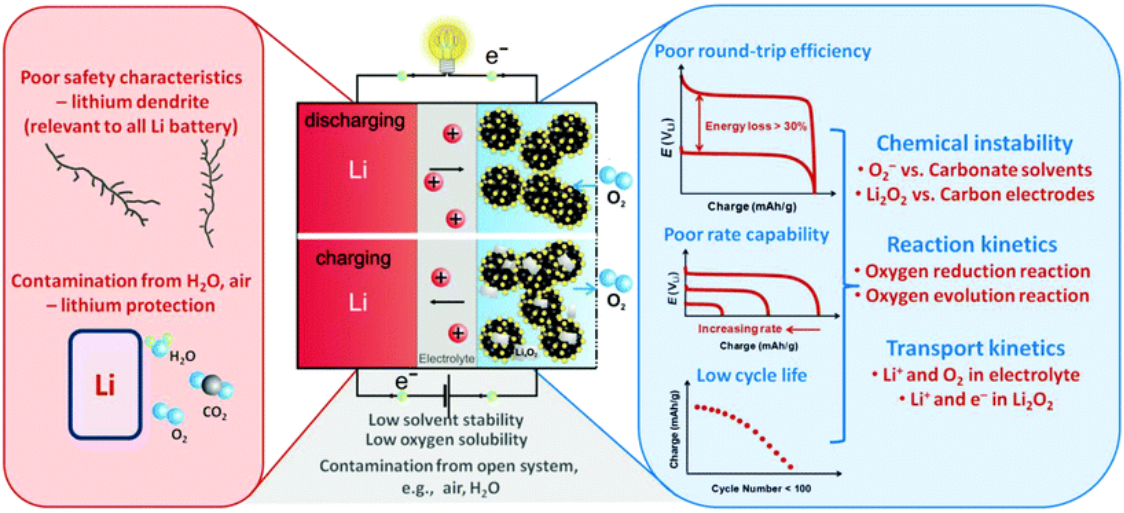

Figure 1.4 Challenges of Li-O_2 Batteries. Reproduced with permission from Ref. [10]. Copyright 2013 RSC.

1.1.2 Redox Flow Batteries

The rapid increase of grid penetration of intermittent renewable energy sources, such as solar and wind, necessitates the development of large-scale energy storage devices to match renewable energy supply and demand. Rechargeable batteries are attractive in these applications without obvious geographical limitations.[5] Among them, redox flow batteries (RFB) is most promising for these grid-level application since it offers much larger storage capacities than other conventional batteries.[7] A RFB represents a class of rechargeable

batteries where chemical energy is provided by two soluble redox pairs. A representative RFB setup (**Figure 1.5**),[15] similar to fuel cells, consists of two electrodes, two redox-active electrolytes separated by an ion exchange membrane and a flow circulation system. Additional electrolytes are stored in two external tanks and can be fed into electrode surfaces as needed by pumps.

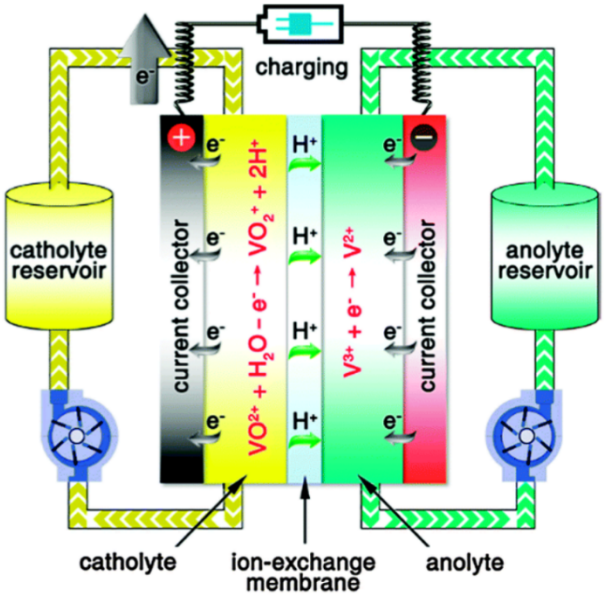

Figure 1.5 Schematic of a typical redox flow battery. Reproduced with permission from Ref. [15]. Copyright 2015 RSC.

The working principle of a RFB is largely different from conventional batteries since the electrodes in a RFB serve only as charge transfer medium instead of participating in redox reactions. RFB utilizes two soluble redox couples with different electrochemical potentials to store electricity during charge, then reversibly converting the stored charge to electricity during discharge.[16] A proton-exchange membrane is put between the two redox electrolytes to prevent their crossover while still allow diffusion of ions to complete the circuit. Taking

the all-vanadium RFB as an example, the electrochemical process during charge and discharge are as following:[17]

Cathode/Catholyte: $VO^{2+} + H_2O - e^- \underset{discharge}{\overset{charge}{\rightleftharpoons}} VO_2^+ + 2H^+ \ (E^0 = 1.00\ V\ vs.SHE)$

Anode/Anolyte: $V^{3+} + e^- \underset{discharge}{\overset{charge}{\rightleftharpoons}} V^{2+} \qquad (E^0 = -0.26\ V\ vs.SHE)$

The redox pairs are the most critical part of a RFB since their properties dominate the overall performance.[18] The open circuit voltage is determined by the difference of the equilibrium potentials of the redox couples used in RFB's half cells. The capacity of a RFB is determined by the effective concentrations of the two redox pairs, which depend on their solubilities and the number of electrons involved in the redox reactions. The energy density is mainly dependent on the effective concentrations of the redox pairs and the cell voltage. The reversibility and mass transfer of the redox active materials are two important factors related with the kinetic of the redox reactions, which significantly influences RFB performance in terms of current, power density as well as cycle lifetime. In addition, the cost of the redox active materials accounts for the majority of the overall RFB system cost for large-scale energy storage applications.

One key distinction of a RFB from other solid-electrode based batteries is that the power and capacity are decoupled and can be scaled-up independently.[19] The power (in Watts) of a RFB could be enhanced by increasing electrode areas, and the capacity (in Watt-hours) of the system could be increased by increasing redox electrolyte amounts. This feature

brings significant benefits such as long discharge duration, design flexibility and excellent scalability. Compared to other conventional batteries, RFBs have other key advantages such as longer cycle lifetime, lower cost and better inherent safety features. As a result, RFBs are well suited for large-scale stationary energy storage applications such as grid-scale electricity leveling.

However, RFBs typically have lower energy densities compared to conventional batteries such as Li-ion batteries.[20] This is due to low solubilities of redox materials as well as low operating voltages in terms of aqueous electrolytes. In addition, current commercialized flow battery technologies such as all-vanadium RFB are still too costly for grid-scale application. The development of cost-effective and high performance RFBs are thus highly needed for large-scale energy storage of renewable energy.[21]

1.2 Photoelectrochemical Solar-to-Chemical Conversion

As the most abundant and clean renewable energy source, solar energy has great potential to solve many energy-related and environmental issues such as energy shortage and global warming. Solar energy can be harvested and converted to different energy forms such as electricity, thermal energy and chemical energy.[22] Considering the intermittent nature of solar energy, solar-to-chemical energy conversion route is the most desirable one since it could convert and store solar energy as chemical energies such as H_2 fuel for off-hour usages.[23] Furthermore, solar-to-chemical route is promising in reducing cost for solar

energy utilization as it replaces relatively sophisticated solid-state junction processing by a much simpler semiconductor-liquid interface formation.[24]

Solar-to-chemical conversion are mainly realized by photochemical and photoelectrochemical (PEC) routes. An efficient solar-to-chemical conversion device requires wide light absorption, efficient charge separation/transfer and fast surface redox reactions.[25] Compared to photochemical process, PEC process not only enables separation of oxidation and reduction half reactions, but also improves solar-to-chemical conversion efficiency by decreasing electron-hole recombination with externally applied bias.[26,27]

Both photocatalytic and photoelectrocatalysis feature a highly unique semiconductor/liquid junction, which is the most crucial part to realize solar to chemical conversion. The easiest situation to consider is the interface between an n-type semiconductor and a liquid containing the redox pair A/A^- (**Figure 1.6**).[28] For a typical case where the electrochemical potential of semiconductor (Fermi level, denoted as E_F) is more negative than of the solution redox potential prior to their contact, electrons flow from n-type semiconductor phase to liquid phase after contact in order to reach equilibrium. This charge transfer leads to the formation of space charge region and upward band bending near semiconductor surface. After equilibrium, the semiconductor Fermi level is at the same level with the electrolyte electrochemical potential.

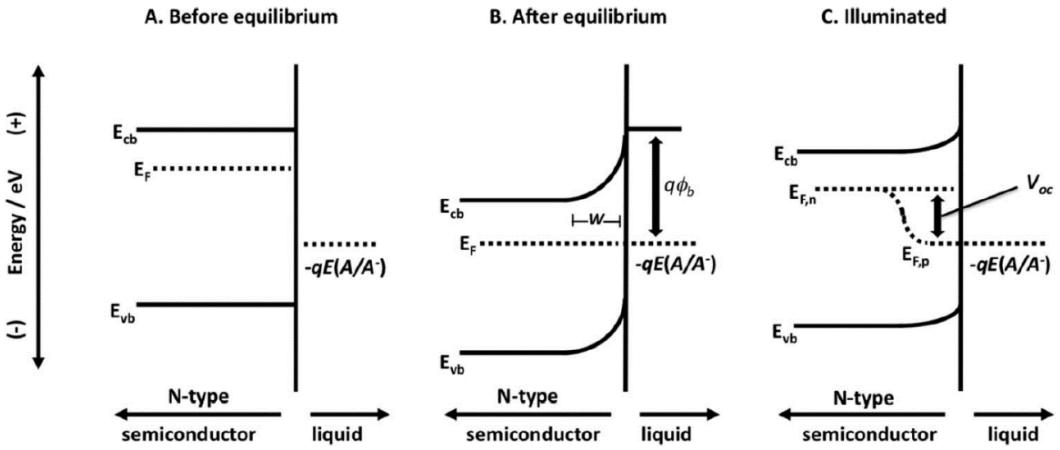

Figure 1.6 The band energetics of a semiconductor/liquid contact before equilibrium, after equilibrium and under illumination. Reproduced with permission from Ref. [28]. Copyright 2010 ACS.

When semiconductor absorbs light (hv > Eg), electrons in the valence band are excited to the conduction band, generating electron-hole pairs. The photogenerated electrons and holes in the space charge region are separated due to the presence of potential gradient. For n-type semiconductor discussed here, photogenerated holes move towards the interface to oxidize the redox species, while photoelectrons move towards the semiconductor bulk. This charge separation decreases the band bending and raises the Fermi level of the n-type semiconductor. Electron quasi-Fermi level (denoted as $E_{F,n}$) and hole quasi-Fermi level (denoted as $E_{F,p}$) are used to describe the energy levels of electrons and holes in semiconductor as the system is no longer in equilibrium. Since the concentration of majority carriers (electrons for n-type semiconductor) almost remains unchanged under

illumination, $E_{f,n}$ still aligns with semiconductor bulk Fermi level. In contrast, $E_{f,p}$ moves below the bulk Fermi level due to the dramatic concentration change of minority carriers (holes for p-type semiconductor) under illumination. The photovoltage (V_{oc}) introduced by illumination in this case is determined by the difference between $E_{f,n}$ and the electrochemical potential of the redox solution.

The photocurrent (denoted as j_{ph}) could be given by calculating the flux of photogenerated minority carriers to the surface. A simplified expression was derived by Gartner in 1959 (Equation 1.1) by assuming negligible electron-hole recombination within the space charge region.[29]

$$j_{ph} = I_0 \left[1 - \frac{\exp(-\alpha W)}{1 + \alpha L_p}\right] \qquad (1.1)$$

In this equation, I_0 is the incident light flux, α is the light light absorption coefficient, W is the space charge layer width, and L_p is minority carrer diffusion length. As shown in Equation 1.2, L_p is determined by the minority carrier (holes for n-type semiconductor) diffusion coefficient (D_p) and hole lifetime (τ_p):

$$L_p = \sqrt{D_p \, \tau_p} \qquad (1.2)$$

The space charge layer width (Equation 1.3) is determiend by the premittvity of free space (ε_0), the static dielectric constant of the semiconductor (ε_{sc}), the doping density (N_d), and the difference between applied potential (V) and flat band potential (V_{fb}).

$$W = \sqrt{\frac{2\varepsilon_0 \varepsilon_{sc}(V - V_{fb})}{qN_d}} \qquad (1.3)$$

The flat band potential of a semiconductor could be determined by plotting Mott-Shottky equation of the depletiong layer capacitance (C_{SC}) as below.

$$\frac{1}{C_{SC}^2} = \frac{2}{qN_d\varepsilon_0\varepsilon_{sc}}\left[\left(V - V_{fb}\right) - \frac{k_B T}{q}\right] \qquad (1.4)$$

In order to achieve efficient PEC solar-to-chemical converion, the general requirements for semiconductor photoelectrodes are summarized as following:

(1) The semiconductor should have an appropriate band gap. On one hand, the band gap should be narrow enough to maximize light absorption and hence theoretical maximum solar energy conversion efficiency. On the other hand, the band gap should be wide enough to provide sufficient photovoltages for redox reactions.

(2) The valence band edge and conduction band edge of the semiconductor should be suitable for redox reactions. Take PEC overall water splitting as an example, the conduction band edge should be more negative than water reduction potential and the valence band edge position should be more positive than water oxidation potential (**Figure 1.7**).[30]

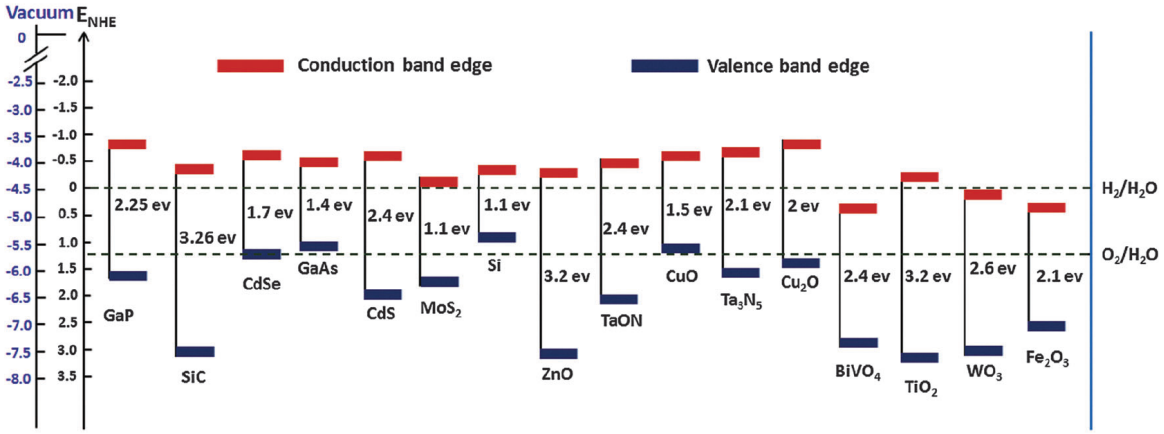

Figure 1.7 Bandgaps and band edge positions of various semiconductors relative to NHE (Normal Hydrogen Electrode) and the vacuum level. Reproduced with permission from Ref. [30]. Copyright 2016 RSC.

(3) The semiconductor should be stable against corrosion during long-term PEC operation.

(4) The semiconductor should be efficient in terms of charge separation and charge transfer. In other words, charge recombination should be minimized in order to achieve high conversion efficiency.

(5) The semiconductor should be catalytically active towards electrolyte redox reactions in order to achieve low overpotentials.

1.3 Solar Rechargeable Redox Flow Battery

PEC energy conversion is one of the most cost-effective and efficient route for intermittent solar energy utilization by directly converting solar energy into chemical

energy. The most common approach is to harvest and store solar energy in the chemical bonds of molecular fuels such as H_2 or organic fuels by PEC water splitting or CO_2 reduction. Typical utilization of solar fuel requires subsequent solar fuel storage and fuel cell for electric power generation in order to complete solar energy utilization (**Figure 1.8a**).[31] As a result, solar energy utilization efficiency is restricted by the efficiencies of the above individual devices as well as the efficiency loss between the device transfers.

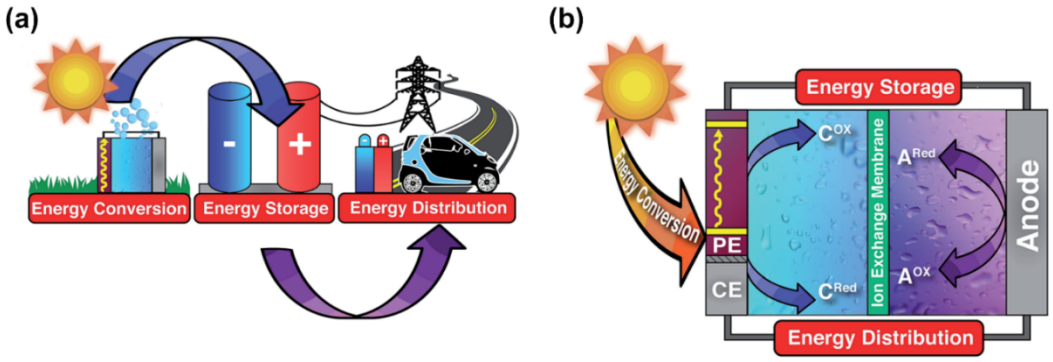

Figure 1.8 Solar energy utilization routes for the conventional solar fuel approach and solar rechargeable redox flow battery approach. Reproduced with permission from Ref. [31]. Copyright 2015 RSC.

Alternatively, solar energy could be in-situ stored as electrochemical energy in an electrochemical energy storage device such as a battery or a capacitor.[32] The products could then be directly utilized for electricity generation via reversible electrochemical processes. This could be achieved in a solar rechargeable electrochemical energy storage device by integrating a PEC cell and an electrochemcial cell into a single device (**Figure 1.8b**). RFBs are considered an outstanding solar energy storage solution since it is inexpensive and amended to scaling. In addition, the integration of RFBs into PEC cells to build

rechargeable redox flow batteries (SRFBs) could be seamless due to the common applied liquid electrolytes in both RFBs and PEC cells.

SRFBs are fabricated through the integration of RFBs with single photoelectrode or dual photoelectrodes via the linkage of redox electrolytes. Under illumination of the photoelectrodes, the photogenerated free charge carriers conduct redox reactions of the redox electrolytes to photocharge the RFBs. The charged RFBs could then be discharged via reversible redox reactions to generate electricity when needed. The reactions during photocharge and discharge can be expressed as following:

Photoanode/Catholyte: $$C^{red} - ne^- \underset{discharge}{\overset{photocharge}{\rightleftharpoons}} C^{ox}$$

Photocathode/Anolyte: $$A^{ox} + ne^- \underset{discharge}{\overset{photocharge}{\rightleftharpoons}} A^{red}$$

SRFBs has several advantages for solar energy utilization compared to solar fuel approach such as solar hydrogen through water splitting. By integrating solar energy conversion, storage and distribution functions in a single unit (**Figure 1.8b**), SRFBs greatly minimize device-to-device energy transfer loss and reduces fabrication costs compared to solar hydrogen approaches. In addition, redox pairs in RFBs typically have much faster kinetics than water splitting reactions, thus a higher solar conversion efficiency is expected compared to solar hydrogen. As for the electric power generation step, the round trip efficiency of a typical RFB (60%-85%) is also higher than a hydrogen fuel cell (20-50%).[33,34] Furthermore, more choices of suitable photoelectrodes are expected for SRFBs

due to the wider selections of redox couples in RFBs. As a result, the overall efficiency of SRFBs is very likely to be much higher than solar fuel approach.[25,35]

In order to unassistedly photocharge state-of-the-art aqueous RFBs where open-circuit-potential is typically about 1.2 V, dual-photoelectrode configuration is generally required to meet the photovoltage demand.[35,36] Similar to overall water splitting system (**Figure 1.9**), the current-voltage data of the photoanode and the photocathode must overlay with each other to achieve unbiased solar charging.[28]

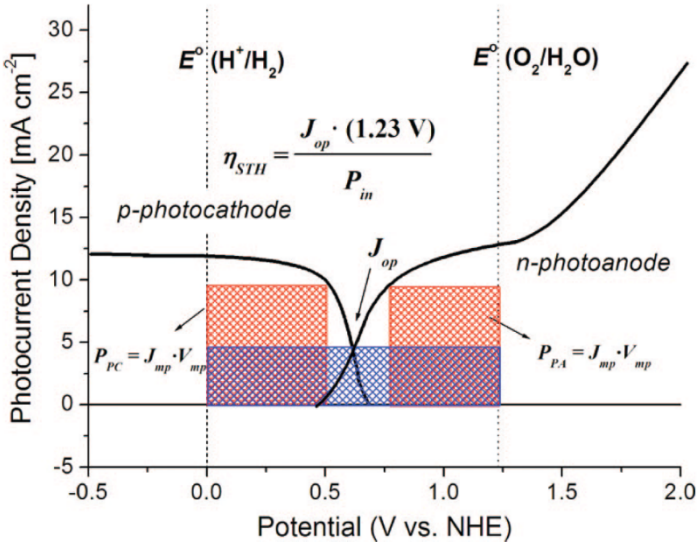

Figure 1.9 Overlaid current-potential curves for a p-type photocathode and an n-type photoanode for overall water splitting. Reproduced with permission from Ref. [28]. Copyright 2010 ACS.

Solar-to-Chemical conversion efficiency (η_{STC}) during photocharging can be calculated using Equation 1.5:[35]

$$\eta_{STC} = \frac{J_{op} \times (E^0_{C^{ox}/C^{red}} - E^0_{A^{ox}/A^{red}}) \times \eta_F}{P_{in}} \times 100\% \qquad (1.5)$$

with P_{in} as the illumination power density, J_{op} as the operating current density, $E^0_{C^{ox}/C^{red}}$ and $E^0_{A^{ox}/A^{red}}$ as the formal potential of catholyte and anolyte redox pairs, and η_F as the lowest Faradic efficiency of the two target redox reactions during photocharging.

Another important parameter is the overall solar-to-electricity ($\eta_{overall}$) efficiency, which is the ratio of output electricity compared to input solar energy. $\eta_{overall}$ could be further estimated according to Equation 1.6:[36]

$$\eta_{overall} = \eta_{STC} \times \eta_{dis} = \frac{E_{out}}{E_{in}} = \frac{\int I_{out} V_{out}\, dt}{P_{in} \times S_{total} \times t'} \times 100\% \qquad (1.6)$$

where I_{out} stands for output discharging current, V_{out} as the output discharging voltage, S_{total} is the total illumination areas of photoanode and photocathode, t' as the illumination time, and t as the discharing time.

1.4 References

[1] Cheng, F.; Liang, J.; Tao, Z.; Chen, J., Functional Materials for Rechargeable Batteries. *Adv. Mater.* **2011,** *23*, 1695.
[2] Winter, M.; Brodd, R. J., What Are Batteries, Fuel Cells, and Supercapacitors? *Chem. Rev.* **2004,** *104*, 4245.
[3] Goodenough, J. B.; Kim, Y., Challenges for Rechargeable Li Batteries. *Chem. Mater.* **2010,** *22*, 587.
[4] Bruce, P. G.; Freunberger, S. A.; Hardwick, L. J.; Tarascon, J.-M., $Li–O_2$ and Li–S batteries with high energy storage. *Nat. Mater.* **2012,** *11*, 19.
[5] Dunn, B.; Kamath, H.; Tarascon, J.-M., Electrical Energy Storage for the Grid: A Battery of Choices. *Science* **2011,** *334*, 928.
[6] Lu, J.; Li, L.; Park, J.-B.; Sun, Y.-K.; Wu, F.; Amine, K., Aprotic and Aqueous $Li–O_2$ Batteries. *Chem. Rev.* **2014,** *114*, 5611.
[7] Soloveichik, G. L., Flow Batteries: Current Status and Trends. *Chem. Rev.* **2015,** *115*, 11533.
[8] Aurbach, D.; McCloskey, B. D.; Nazar, L. F.; Bruce, P. G., Advances in understanding mechanisms underpinning lithium-air batteries. *Nat. Energy* **2016,** *1*, 16128.
[9] Girishkumar, G.; McCloskey, B.; Luntz, A. C.; Swanson, S.; Wilcke, W., Lithium-Air Battery: Promise and Challenges. *J. Phys. Chem. Lett.* **2010,** *1*, 2193.
[10] Lu, Y.-C.; Gallant, B. M.; Kwabi, D. G.; Harding, J. R.; Mitchell, R. R.; Whittingham, M. S.; Shao-Horn, Y., Lithium-oxygen batteries: bridging mechanistic understanding and battery performance. *Energy Environ. Sci.* **2013,** *6*, 750.
[11] Kwabi, D. G.; Ortiz-Vitoriano, N.; Freunberger, S. A.; Chen, Y.; Imanishi, N.; Bruce, P. G.; Shao-Horn, Y., Materials challenges in rechargeable lithium-air batteries. *MRS Bull* **2014,** *39*, 443.
[12] Cheng, X.-B.; Zhang, R.; Zhao, C.-Z.; Zhang, Q., Toward Safe Lithium Metal Anode in Rechargeable Batteries: A Review. *Chem. Rev.* **2017,** *117*, 10403.
[13] McCloskey, B. D.; Speidel, A.; Scheffler, R.; Miller, D. C.; Viswanathan, V.; Hummelshøj, J. S.; Nørskov, J. K.; Luntz, A. C., Twin Problems of Interfacial Carbonate Formation in Nonaqueous $Li-O_2$ Batteries. *J. Phys. Chem. Lett.* **2012,** *3*, 997.
[14] Ottakam Thotiyl, M. M.; Freunberger, S. A.; Peng, Z.; Bruce, P. G., The Carbon Electrode in Nonaqueous $Li-O_2$ Cells. *J. Am. Chem. Soc.* **2013,** *135*, 494.
[15] Zhao, Y.; Ding, Y.; Li, Y.; Peng, L.; Byon, H. R.; Goodenough, J. B.; Yu, G., A chemistry and material perspective on lithium redox flow batteries towards high-density electrical energy storage. *Chem. Soc. Rev.* **2015,** *44*, 7968.
[16] Jens, N.; Nataliya, R.; Tatjana, H.; Peter, F., The Chemistry of Redox-Flow Batteries. *Angew. Chem. Int. Ed.* **2015,** *54*, 9776.
[17] Álvaro, C.; Jorge, M.; Nuno, R.; P., B. F., Vanadium redox flow batteries: a technology review. *International Journal of Energy Research* **2015,** *39*, 889.
[18] Pan, F.; Wang, Q., Redox Species of Redox Flow Batteries: A Review. *Molecules* **2015,** *20*.

[19] Chalamala, B. R.; Soundappan, T.; Fisher, G. R.; Anstey, M. R.; Viswanathan, V. V.; Perry, M. L., Redox Flow Batteries: An Engineering Perspective. *Proceedings of the IEEE* **2014,** *102*, 976.
[20] Ponce de León, C.; Frías-Ferrer, A.; González-García, J.; Szánto, D. A.; Walsh, F. C., Redox flow cells for energy conversion. *J. Power Sources* **2006,** *160*, 716.
[21] Li, B.; Liu, J., Progress and directions in low-cost redox-flow batteries for large-scale energy storage. *National Science Review* **2017,** *4*, 91.
[22] Lewis, N. S., Research opportunities to advance solar energy utilization. *Science* **2016,** *351*, 353.
[23] Tachibana, Y.; Vayssieres, L.; Durrant, J. R., Artificial photosynthesis for solar water-splitting. *Nat. Photon.* **2012,** *6*, 511.
[24] Sivula, K.; van de Krol, R., Semiconducting materials for photoelectrochemical energy conversion. *Nat. Rev. Mater.* **2016,** *1*, 15010.
[25] Sheng, C.; Wei, L.; Yanfa, Y.; Thomas, H.; Ishiang, S.; Dunwei, W.; Zetian, M., Roadmap on solar water splitting: current status and future prospects. *Nano Futures* **2017,** *1*, 022001.
[26] Grätzel, M., Photoelectrochemical cells. *Nature* **2001,** *414*, 338.
[27] Hisatomi, T.; Kubota, J.; Domen, K., Recent advances in semiconductors for photocatalytic and photoelectrochemical water splitting. *Chem. Soc. Rev.* **2014,** *43*, 7520.
[28] Walter, M. G.; Warren, E. L.; McKone, J. R.; Boettcher, S. W.; Mi, Q.; Santori, E. A.; Lewis, N. S., Solar Water Splitting Cells. *Chem. Rev.* **2010,** *110*, 6446.
[29] Gärtner, W. W., Depletion-Layer Photoeffects in Semiconductors. *Phys. Rev.* **1959,** *116*, 84.
[30] Tamirat, A. G.; Rick, J.; Dubale, A. A.; Su, W.-N.; Hwang, B.-J., Using hematite for photoelectrochemical water splitting: a review of current progress and challenges. *Nanoscale Horizons* **2016,** *1*, 243.
[31] Yu, M.; McCulloch, W. D.; Huang, Z.; Trang, B. B.; Lu, J.; Amine, K.; Wu, Y., Solar-powered electrochemical energy storage: an alternative to solar fuels. *J. Mater. Chem. A* **2016,** *4*, 2766.
[32] Schmidt, D.; Hager, M. D.; Schubert, U. S., Photo-Rechargeable Electric Energy Storage Systems. *Adv. Energy Mater.* **2016,** *6*, 1500369.
[33] Leung, P.; Li, X.; Ponce de Leon, C.; Berlouis, L.; Low, C. T. J.; Walsh, F. C., Progress in redox flow batteries, remaining challenges and their applications in energy storage. *RSC Adv.* **2012,** *2*, 10125.
[34] Pellow, M. A.; Emmott, C. J. M.; Barnhart, C. J.; Benson, S. M., Hydrogen or batteries for grid storage? A net energy analysis. *Energy Environ. Sci.* **2015,** *8*, 1938.
[35] Liao, S.; Zong, X.; Seger, B.; Pedersen, T.; Yao, T.; Ding, C.; Shi, J.; Chen, J.; Li, C., Integrating a dual-silicon photoelectrochemical cell into a redox flow battery for unassisted photocharging. *Nat. Commun.* **2016,** *7*, 11474.
[36] Li, W.; Fu, H. C.; Li, L.; Cabán‐Acevedo, M.; He, J. H.; Jin, S., Integrated Photoelectrochemical Solar Energy Conversion and Organic Redox Flow Battery Devices. *Angew. Chem. Int. Ed.* **2016,** *55*, 13104.

Chapter 2 Protected Three Dimentionally Ordered Mesoporous Carbon as a Li-O_2 Battery Cathode

2.1 Introduction

Enabled by the reversible conversion between Li_2O_2 and O_2, Li-O_2 batteries promise theoretical gravimetric capacities significantly greater than Li-ion ones. The poor cycling performance, however, has greatly hindered the development of this technology. At the heart of the problem is the reactivity exhibited by carbon cathode support under cell operation conditions. One strategy is to conceal the carbon surface from reactive intermediates. Here we show that long cyclability can indeed be achieved on three-dimensionally ordered mesoporous (3DOm) carbon by growing a thin layer of FeO_x using atomic layer deposition (ALD). 3DOm carbon distinguishes itself from other carbon materials with well-defined pore structures, providing a unique material platform for fundamental understandings of processes important to Li-O_2 battery operations. When decorated with Pd nanoparticle catalysts, also prepared by ALD, the new cathode exhibits a capacity >6000 mAh/g_{carbon} and cyclability >68 cycles.

2.2 Experimental Details

2.2.1 Materials synthesis

3DOm carbons were made by following the method reported in literatures.[1,2] A precursor solution made of furfuryl alcohol and oxalic acid with a weight ratio of 200:1 was impregnated within silica colloidal crystal templates composed of highly monodisperse 12 or 35 nm silica nanoparticles (SNPs). The resulting samples were heated to 70 ^{o}C for 2 days to polymerize furfuryl alcohol, followed by heating at 200 ^{o}C in flowing N_2 for 3 h to cure the polymer, and then heated at 900 ^{o}C for an additional 2 h to carbonize the samples. The SNPs were dissolved in 6 M KOH solution at 150 ^{o}C for 2 days to yield 3DOm carbon replica. The resulting carbon material was then thoroughly washed with 70 °C deionized water until the resulting solution was near neutral. Finally, the 3DOm carbon was dried at 70 ^{o}C for 24 h.

Carbon and polytetrafluoroethylene (PTFE) were mixed in isopropyl alcohol (IPA) with a mass ratio of 8:2. The mixture was dispersed by sonication and coated on the Ni foam (1.6mm in thickness originally, MTI Corp.). The electrode was further dried in vacuum oven overnight to remove the residual solvent.

The growth of FeO_x has been reported by us previously.[3-5] The as-prepared carbon electrodes were placed in the ALD (Savannah S100, Ultratech/CambridgeNanoTech) chamber and heated to 180 °C. Iron *tert*-butoxide ($Fe_2(^{t}BuO)_6$) and water were employed as precursors at 120 °C and 25 °C, respectively. Each cycle of the growth followed the repeated sequence of 3 s Fe precursor pulse, 60 s Fe precursor diffusion/adsorption/reaction, 90 s N_2 purging; 0.05 s water pulse, 60 s water precursor diffusion/adsorption/reaction, and

another 90s N_2 purging. A typical growth lasts 50 cycles to yield desired coating of FeO_x of ca. 1.4 nm in thickness.

Pd nanoparticles were deposited using ALD as well. The growth temperature was 250 °C, with $Pd(hfac)_2$ (Palladium(II) hexafluoroacetylacetonate, 60 °C) and formalin (37 wt% in H_2O, 25 °C) as precursors. Each cycle consisted of 5 repeated pulse/purge sub-cycles of $Pd(hfac)_2$ and formalin for sufficient surface adsorption in the high aspect ratio 3DOm carbon.

The loading quantity was examined by microbalance (Sartorius, CPA2P). The resulting loading of carbon on Ni foam (15-30mg per piece) varied between 0.5mg/cm^2 to 1mg/cm^2. The weight ratio of FeO_x:C and Pd:C was measured as 1:5 and 1:10, respectively.

2.2.2 Electrochemical characterization

$LiClO_4$ in dimethoxyethane (0.1 M) was used as purchased from Novolyte (BASF) with water level <10 ppm. Tetraethylene glycol dimethyl ether (TEGDME, ≥ 99%, Sigma-Aldrich) was first stored over freshly activated 4 Å molecular sieves and then distilled. The distilled TEGDME was stored over molecular sieves before usage. $LiClO_4$ (99.99%, Battery grade, Sigma-Aldrich) was baked at 130 °C in a vacuum oven within the glove box and mixed with TEGDME to generate the 1 M electrolyte solution. Customized Swagelok^{TM} type cells (**Figure 2.1**) were assembled in the glove box (H_2O and O_2 levels < 0.1 ppm, MBraun) with Li metal(380μm in thickness, Sigma-Aldrich) as the anode,

Celgard 2400 films as the separator, 100 to 200μL 0.1 M $LiClO_4$ in DME or 1.0 M $LiClO_4$ in TEGDME as the electrolyte. Batteries were studied using potentiostats (VMP3, Bio-Logic).

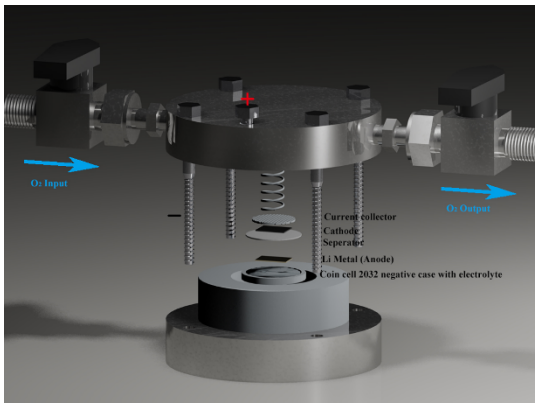

Figure 2.1 A Swagelok™ cell design. The design of our cell was modified from literature reports.[6]

For DEMS characterization, the cell was first discharged in TEGDME under pure O_2 to a given capacity. The discharged cell was then evacuated for 5 h to remove remaining O_2. For *in situ* analysis, the cell was connected to the mass spectrometer with a dry rotary pump (nXDS 10i, Edwards) as the differential pump. The cell was wired to a potentiostat (609D, CH Instruments) for galvanostatic recharging, while gas content was analyzed using a customized mass spectrometer with quadrupole mass analyzer (Microvision 2, MKS). Each scan was collected from 28 to 44 amu within 3 s to give desired time resolution and accuracy.

2.2.3 Material characterization

Scanning electron microscopy (SEM) images were taken on a JEOL 6340F microscope and TEM were performed on a JEOL 2010F microscope operated at 200 kV. X-ray diffraction (XRD) measurements were performed on PANalytical X'Pert Pro diffractometer with Cu Kα radiation. The cell was first transferred to an O_2-toleranted Ar-filled glove box (H_2O level < 0.1 ppm, MBraun) and disassembled inside to extract the cathode, which was then rinsed with pure anhydrous DME (Sigma-Aldrich) for 3 times to remove remaining salts. An airtight sample holder with an X-ray transparent Kapton film window was used to transfer the sample and carry out XRD characterizations without exposing the sample to the ambient air. Raman spectra and mapping were acquired using a micro-Raman system (XploRA, Horiba) with a 532nm laser excitation. The N_2 adsorption/desorption experiments were carried out on an automatic gas sorption analyzer (Autosorb iQ, Quantachrome) at 77 K. The pore size distribution and cumulative pore volume were obtained by applying a built-in quenched state density functional theory (QSDFT) adsorption model with cylindrical/spherical configuration for carbon (ASiQwin v3.0, Quantachrome). Surface analysis was carried out using a K-Alpha XPS (Thermo Scientific). The sample was also washed by DME with the same procedure as described above and mounted on the sample stage with a short exposure to the ambient air (typically <5 min) before entering the load lock. XPS data was calibrated by adventitious carbon at 284.8eV and fitted using XPS Peak 4.1 software. For example, for oxygen species, linear background was subtracted and mixed Lorentzian-Gaussian shape peaks were adopted, peak positions for different oxygen species were adopted from previous literature reports.

2.3 Results and Discussions

2.3.1 Structure and performance of pristine 3DOm carbon

Metal-air battery has been studied for decades, with the interest in Li-O_2 battery intensified recently for its potentially high gravimetric capacities.[7-10] The key to successful operation of a Li-O_2 battery is the control over Li_2O_2 formation and its decomposition. Many of the observed failing mechanisms are connected to these two processes.[11,12] For instance, discharge products other than Li_2O_2 are often found difficult to decompose upon recharge, leading to fast capacity fading. Side reactions other than Li_2O_2 formation and decomposition degrade the electrode or the electrolyte or both.[13,14] Synergistic effects between carbon support and the electrolyte have been recently recognized to contribute to these side reactions.[15] Existing reports on details of Li_2O_2 formation concerning, for example, their sizes, morphologies, and crystallinity vary, making it difficult to draw a unified understanding of the key processes involved in Li-O_2 battery operations.[16-19] The issue is compounded in part by the poorly defined pore structures and surfaces of carbon support reported to date. It becomes clear that detailed studies of Li_2O_2 formation and decomposition on a cathode support of well-defined structures and surfaces should be of great value.[20-23] In this context, 3DOm carbon, an inverse replica of face-centered-cubic (FCC) close-packed structures (**Figure 2.2**), presents a unique opportunity to understand Li-O_2 battery operations.[2,24] The size of pores and windows connecting the pores in the 3DOm carbon can be independently tailored as has been reported previously.[2] This feature makes 3DOm carbon distinctly different from other carbon support (e.g., super P or Vulcan carbon) where well-defined pores in the range of tens of nanomaterials are not

available.[25,26] In this regard, 3DOm carbon also distinguishes itself from carbon nanotubes whose sidewalls are essentially open spaces.[27] Similarly, spaces between randomly arranged graphene (and other graphene derivatives including reduced graphene oxides) are also less than uniform.[28]

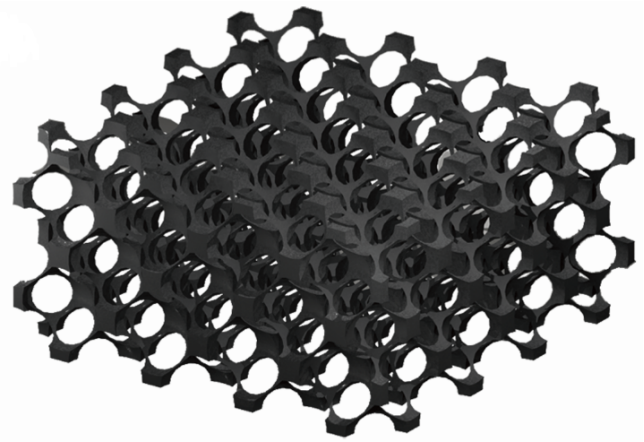

Figure 2.2 Structure of 3DOm carbon with well-defined pore sizes.

To demonstrate what the well-defined pores enable, we compared the 1st cycle performance of 3DOm carbon with other commercially avaiable carbon including super P carbon and Vulcan carbon 72. As shown in **Figure 2.3**, 3DOm carbon has larger capacities and lower recharge overpotentials. The larger capacities are mainly related with the higher total pore volumes of 3DOm carbons (**Table 2.2**).[29] The lower recharge overpotentials could be explained by the smaller particle sizes of Li_2O_2 confined by the pore sizes of 3DOm carbons. The reduced Li_2O_2 particle size decreases the polarization required to decompose Li_2O_2 particles.

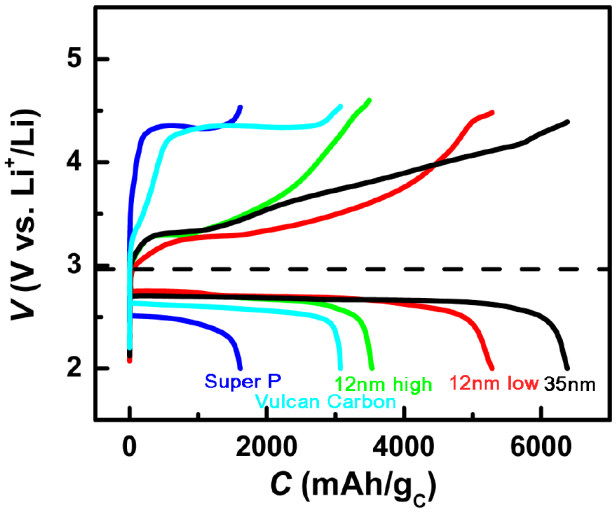

Figure 2.3 First cycle performance of Super P carbon, Vulcan carbon and 3DOm carbon at 200mA/g_c.

To prove the pore confinement effect of Li_2O_2 in 3DOm carbons, we employed SEM to characterize 3DOm carbon at different stages of discharge/recharge. As is seen in **Figure 2.4**, the porous nature of the surfaces remained intact up to 4000 mAh/g, >67% of the full state of discharge (SOD, ca. 6000 mAh/g). The evidence strongly supports that majority of the Li_2O_2 products deposit within the large pores of 3DOm carbon. As the Li_2O_2 particle sizes are not expected to exceed the dimensions of the hosting pores, for the first time we obtained complete control over the site and size of Li_2O_2 growth in Li-O_2 operations. The relatively small pore sizes are considered advantageous because they minimize impact of electronic and ionic polarizations within Li_2O_2 on the discharge/recharge overpotentials.[30,31] Toward the end of discharge, starting at 5000 mAh/g, we started to observe particulate Li_2O_2 appearance on the exterior of 3DOm carbon (**Figure 2.4g**). The

porous surface of 3DOm was fully exposed with no visible residues upon recharge (**Figure 2.4i**).

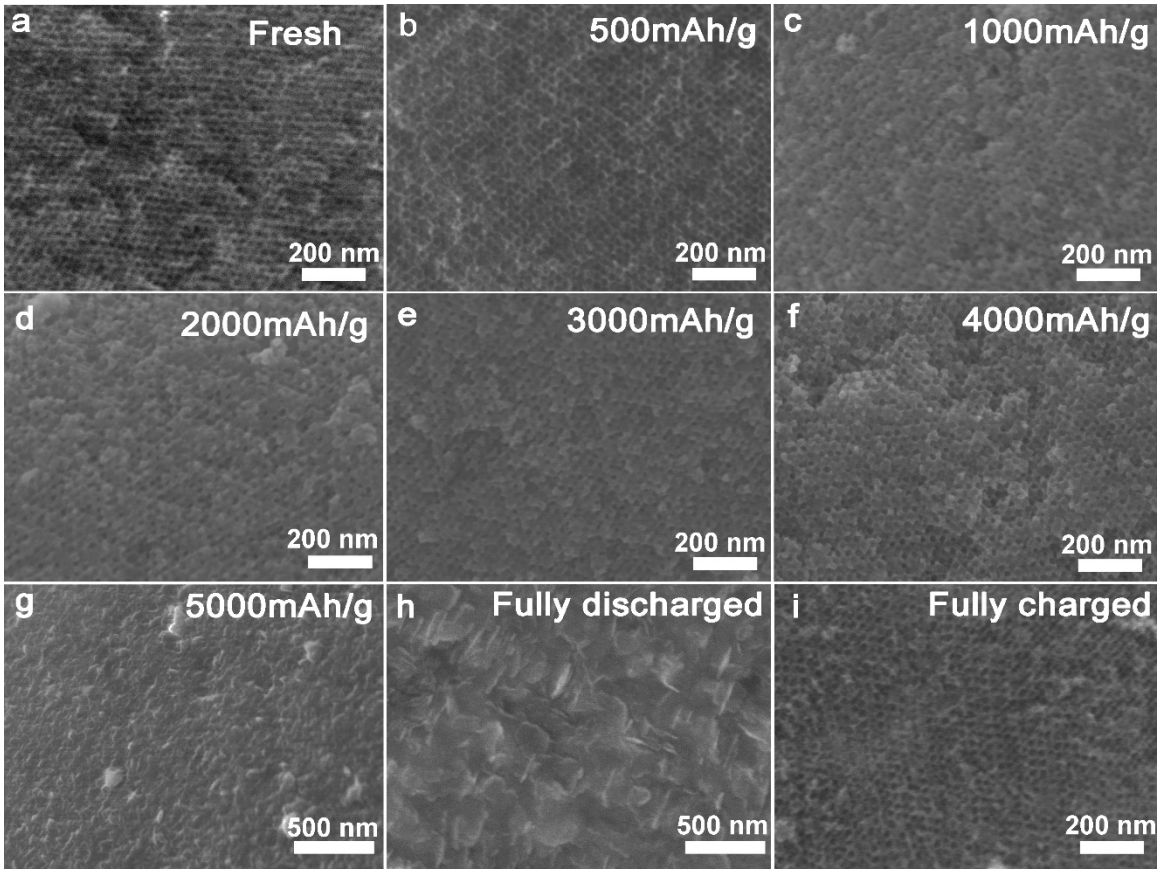

Figure 2.4 Scanning electron micrographs of 3DOm carbon surfaces at different stage of discharge and recharge.

The growth of Li_2O_2 within the pores of 3DOm carbon was also confirmed by TEM characterizations (**Figure 2.5**). After discharge, the mesopores within each micrometers size carbon particles were filled with Li_2O_2. Most products formed inside the pores as shown in the inset of **Figure 2.5b**. Few large particles were observed outside the pores.

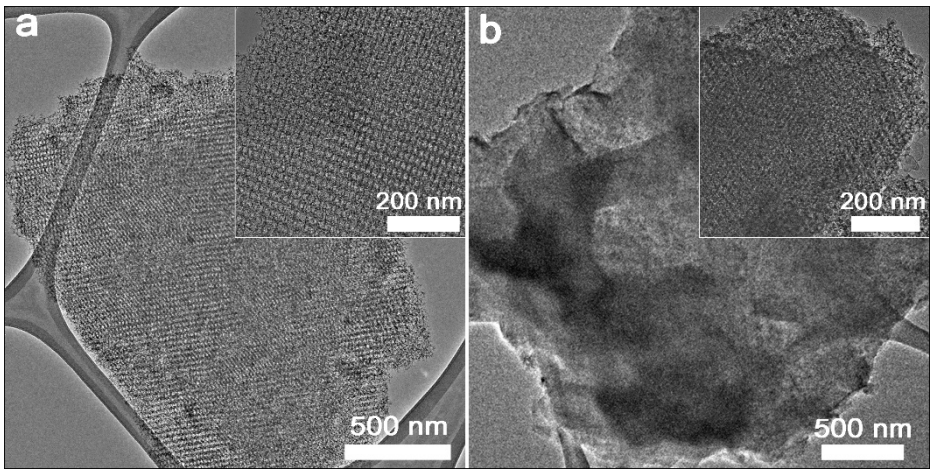

Figure 2.5 TEM characterizations of (a) pristine Pd/FeO_x modified 35nm 3DOm carbon and (b) fully discharged Pd/FeO_x modified 35nm 3DOm carbon samples.

The pore filling details could be furture evidenced by the pore size distribution analysis of fresh and discharged 35 nm 3DOm carbon electrode. As shown in **Figure 2.6**, the total pore volume around 30 nm pore diameter significantly decreased after discharge, proving the pore filling by discharged product Li_2O_2. The cumulative pore volume result (**Figure 2.6c**) further shows that only about 50% of the total pores are occupied for a fully discharged electrode. Specifically, the pores on the surface would be filled up at a faster rate than pores deep underneath the electrode/electrolyte interface. This is because oxygen concentration on the top is the highest and will produce Li_2O_2 at a faster rate. We indeed see from **Figure 2.6** that the pore size distribution is broadened upon discharge.

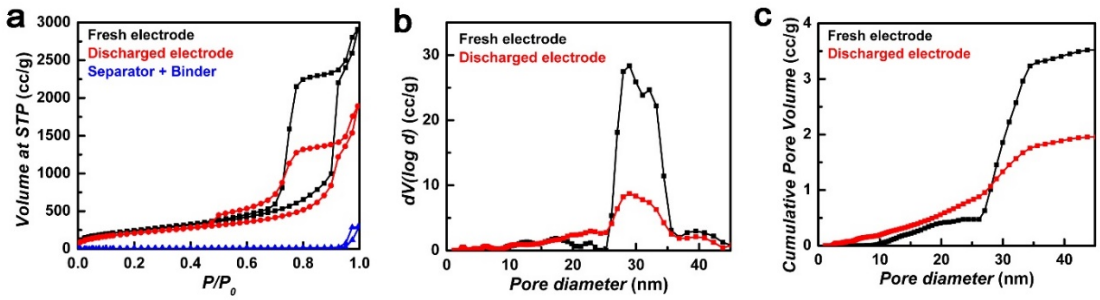

Figure 2.6 Pore size distribution of fresh and discharged 35nm 3DOm carbon electrode.

Calculations of pore filling by Li_2O_2 within a 35nm 3DOm electrode based on an oxygen diffusion model was performed to support our hypothesis. The calculations were based on the following assumptions. First, the deposition rate of Li_2O_2 is first order to O_2 concentration. Second, the diffusion of O_2 follows the Fick's law. Third, O_2 is saturated in the electrolyte at the beginning of the discharge reactions. Fourth, the only source of O_2 supply comes from the electrolyte/gas surface.

$$\frac{\partial(\varepsilon \cdot c)}{\partial t} = \frac{\partial}{\partial x}(D \cdot \varepsilon^{\beta-1} \frac{\partial c}{\partial x}) - \frac{R}{2F}$$

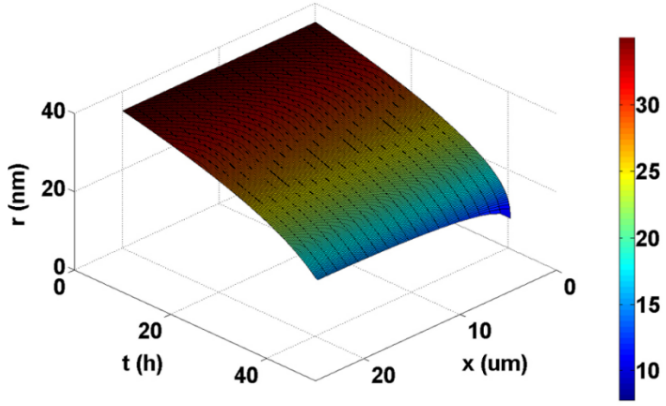

Figure 2.7 Pore size distribution at different depths and discharge times.

We see from **Figure 2.7** that the Li_2O_2 distribution becomes less uniform (more Li_2O_2 close to the electrode/electrolyte interface) at a deeper level of DOD. The reason is that O_2 concentration is higher at locations closer to the electrolyte/gas interfaces. At the end of the discharge, the surface pores are completely filled by Li_2O_2. At the stage, no additional O_2 will be supplied, and discharge overpotential will increase sharply. Pores far away from the electrode/electrolyte interface are not yet filled, leading to broadening of pore size distribution by BET measurements.

Our calculations further reveal that the pore filling percentage (which directly corresponds to achievable capacities) also depends on: (1) the type of electrolyte (through influencing O_2 diffusion coefficient and solubility); (2) loading density of carbon materials (through changing the overall normalized specific capacities); (3) discharge current densities (by dictating reaction kinetics).

Pore filling by discharge product during discharging was simulated based on a simplified oxygen diffusion model using MATLAB. Briefly, we assume

(1) The diffusion of O_2 follows Fick's law with porosity consideration.[32]

$$\frac{\partial(\varepsilon \cdot c)}{\partial t} = \frac{\partial}{\partial x}(D \cdot \varepsilon^{\beta-1} \frac{\partial c}{\partial x}) - \frac{R}{2F} \qquad (2.1)$$

(2) The reaction rate is first order proportional to (a) oxygen concentration and (b) electrode/electrolyte interface area.

$$R(x,t) \propto c(x,t) \cdot s(x,t) \qquad (2.2)$$

$$\int_0^L R(x,t)dx = j \qquad (2.3)$$

$$s(x,t) \propto (\frac{\varepsilon}{\varepsilon_0})^{2/3} \qquad (2.4)$$

(3) The reaction product (Li_2O_2) form a thin film to coat the inner pores and cause the local porosity to decrease.

$$\frac{\partial \varepsilon(x,t)}{\partial t} = -\frac{R(x,t)}{2F} \cdot \frac{M}{\rho} \qquad (2.5)$$

$$\varepsilon(x,0) = \varepsilon_0 \qquad (2.6)$$

(4) At the oxygen/electrolyte interface, the oxygen concentration in the electrolyte always equals to saturation concentration due to fast dissolution. At the electrode/separator interface, oxygen does not pass the boundary.

$$c(x,0) = c_0 \qquad (2.7)$$

$$c(0,t) = c_0 \qquad (2.8)$$

$$\frac{dc(L,t)}{dx} = 0 \qquad (2.9)$$

Table 2.1: Definition of all symbols.

Symbols	Meaning	Value	Unit
ε	Local porosity of carbon		

c	Local oxygen concentration		mol/cm^3
t	Elapsed time since discharging started		s
x	Distance from oxygen/electrode interface		cm
D	Diffusion coefficient of oxygen in the electrolyte[33]	1.22×10^{-5}	cm^2/s
β	Bruggeman coefficients	3	
R	Oxygen consumption rate per unit distance		A
F	Faraday constant	96485	As/mol
s	Surface area		cm^2
L	The overall thickness of carbon electrode		cm
j	Cell discharge current		A
ε_0	Initial porosity	0.74	
M	Molar mass of Li_2O_2	46	g/mol
ρ	Density of Li_2O_2	2.3	g/cm^3
c_0	Maximum oxygen solubility in the electrolyte[34]	9.57×10^{-6}	mol/cm^3

We next study how the cyclability depends on the pore sizes of the 3DOm carbons. Our understanding as depicted in **Figure 2.8** is based on the following assumptions. First, side-reactions other than Li_2O_2 formation and decomposition on the surfaces of carbon are inevitable during Li-O_2 battery operations.[35] Second, these reactions result in accumulation of by-products that will eventually clog the pores of 3DOm carbon.[11,13,36] Third, once the pores are clogged, the volume accessible for Li_2O_2 deposition drops dramatically to result

in cell failure. Since smaller pores correspond to greater surface-to-volume ratios, they will be clogged more easily than bigger pores. We therefore expect poorer cyclability on 3DOm carbon of smaller pores.

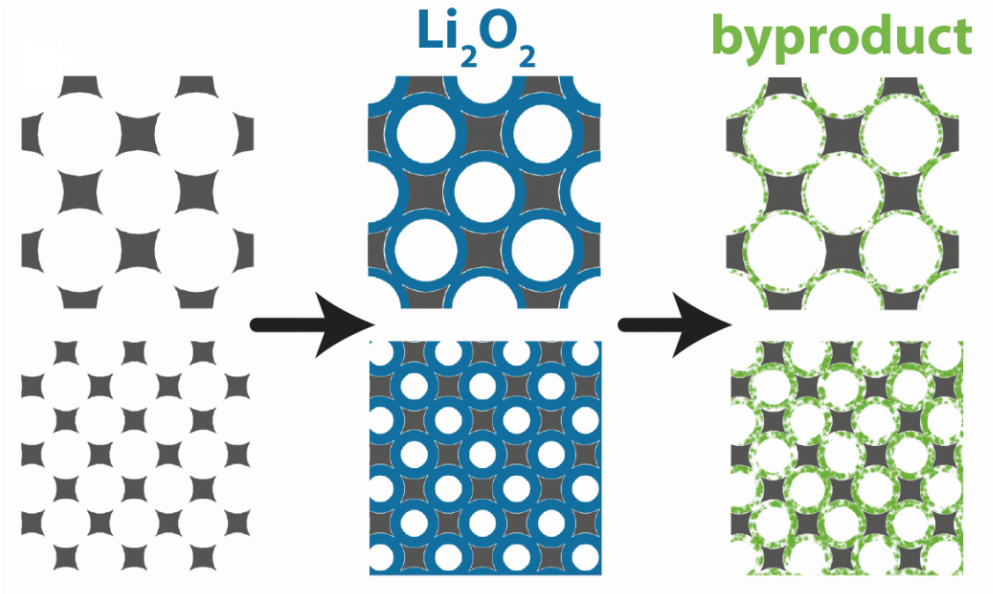

Figure 2.8 The formation and accumulation of by-products shown in a simplified two-dimensional representation. Undesired byproducts accumulate faster on 3DOm carbon with small pores (bottom panels) than large ones (top panels). Left: pristine carbon; middle: with discharge product (Li_2O_2); right: after recharge, where green deposits represent byproducts that cannot be easily decomposed.

In order to study the influence of mesopores (2-50 nm) and micropores (< 2 nm) on battery performance, we choose 12 nm 3DOm with varied micropore volumes and 35 nm 3DOm carbons as our study platform. Their different pore sizes are indicated by N_2

adsorption/desorption results **(Figure 2.9** and **Table 2.2)** and small angle X-ray diffraction **(Figure 2.10)**.

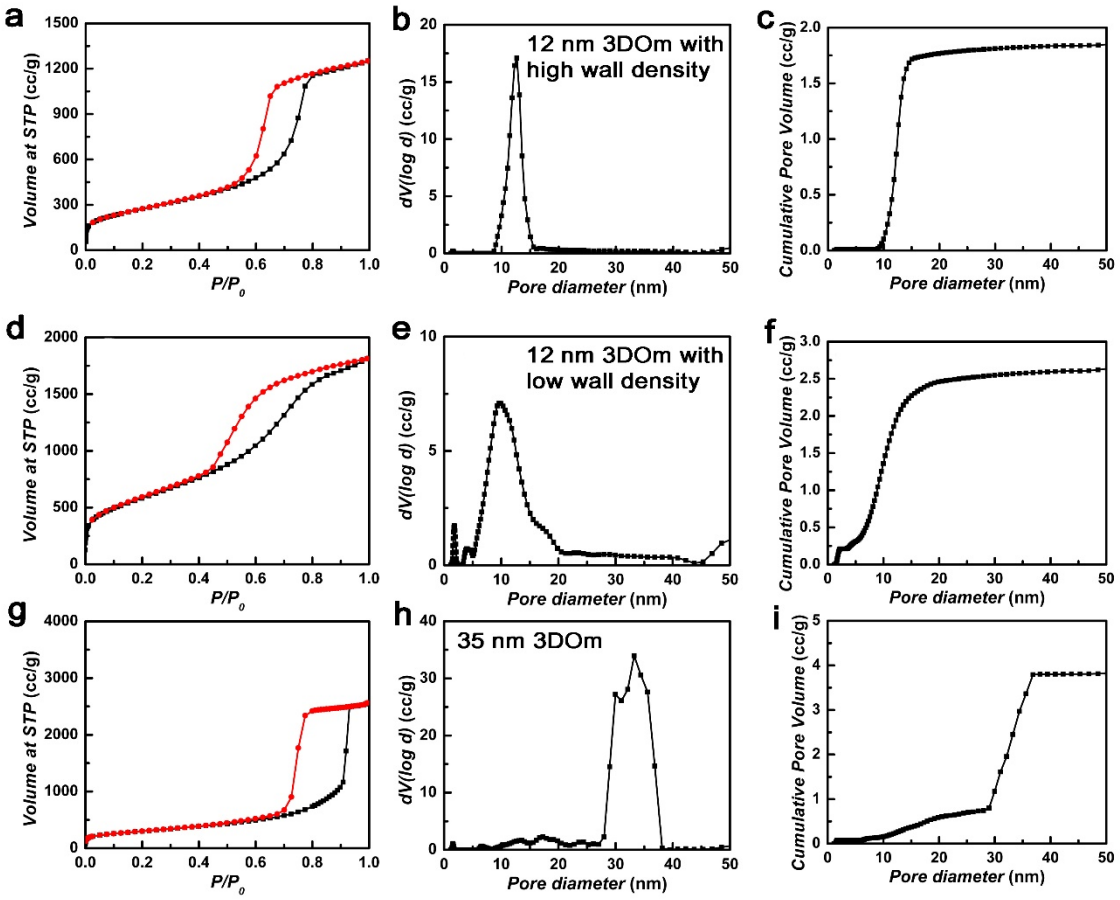

Figure 2.9: N_2 sorption isotherm, pore size distribution, and cumulative pore volume of as-prepared 12nm 3DOm carbon with high wall density (a, b, c), 12nm 3Dom carbon with low wall density (d, e, f) and 35nm 3DOm carbon (g, h, i).

Table 2.2: Textural data from N_2 sorption measurement for the carbons and electrodes.

	Total pore volume [a] (cc/g)	surface area [a] (m^2/g)	Micropore volume [b] (cc/g)

12 nm 3DOm carbon with high wall density	1.85	901	0.012
12 nm 3DOm carbon with low wall density	2.64	1902	0.19
35 nm 3DOm carbon	3.82	1028	0.078
Fresh electrode	3.76	809	~0
Discharged electrode	2.17	657	~0
35 nm 3DOm carbon with 50 cycle ALD FeO_x	3.94	1045	0.071

[a] From QSDFT model

[b] From the cumulative pore volume calculated from the QSDFT analysis when the pore size is smaller than 2 nm.

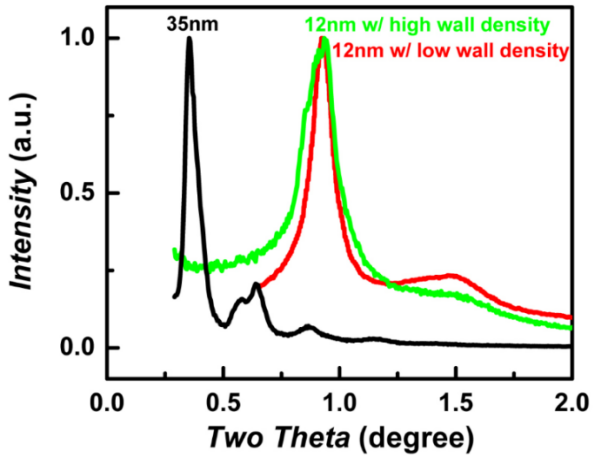

Figure 2.10 Small angle X-ray diffraction of the 3DOm carbon samples used in the study.

The expectation was indeed verified in **Figure 2.11**. Even by limiting the discharge capacity to a modest 500 mAh/g_{carbon}, less than 10% of the total achievable capacities, we observed severe capacity fading by the 15th cycle of recharge for 3DOm carbon of 35 nm

pores. Poorer cycling performance was witnessed on 3DOm carbon of smaller pores (6^{th} to 7^{th} cycle for 12 nm pores).

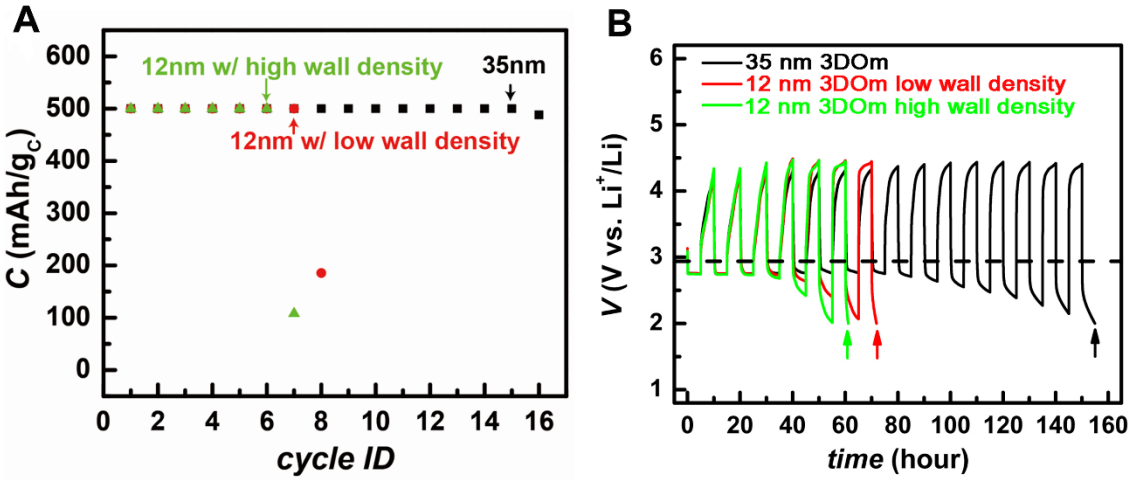

Figure 2.11 Cycling performance of bare 3DOm carbon of different pore sizes. The capacity is limited to 500 mAh/gcarbon; rate: 100 mA/gcarbon.

As far as capacity is concerned, we expect it only depends on the accessible mesopores (i.e., pores defined by the silica beads) but not the micropores in the carbon walls (d≤2 nm). This is because the micropores are too small to support Li_2O_2 deposition. Indeed, upon deep discharge, the capacities normalized to the volumes specific to the large pores as shown in **Figure 2.12** are comparable (1700 mAh/mL_{pore} for 35 nm and 2000 mAh/mL_{pore} for 12 nm 3DOm carbon). Most strikingly, we see negligible difference between the capacities measured on 3DOm carbon of similar pore sizes (ca. 12 nm) but different micropore volumes (green and red traces in **Figure 2.12**), strongly supporting that micropores do not contribute to the capacities.

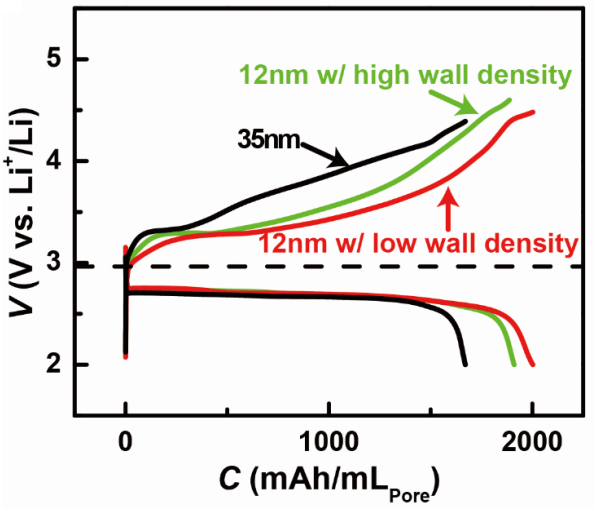

Figure 2.12 Discharge/charge behaviors normalized to pore volumes.

2.3.3 Protection of 3DOm carbon

Next, we seek to address an important concern in using carbon support for Li-O_2 battery operations, specially the reactivity of carbon.[37] Increasing evidence suggests that carbon is unstable against O_2^- during discharge.[35] Carbon is also reactive under high recharge potentials.[15,36] Our strategy to address the issue is to physically separate carbon surface from Li_2O_2, any reaction intermediates, as well as the electrolyte. The goal is achieved by growing a thin, uniform layer of iron oxides on 3DOm carbon (**Figure 2.13a**). Thanks to the synthesis procedures of 3DOm carbon, its surface is inherently hydrophilic, ideal for growing oxides by atomic layer deposition (ALD). ALD growth has the benefit of affording complete coverage with minimum defects.

The uniformity of the FeO_x growth is first confirmed by the Brunauer-Emmett-Teller (BET) pore size measurements. As shown in **Figure 2.13b**, the average pore sizes of 35 nm 3DOm carbons have been reduced from 33.0 nm to 30.2 nm, corresponding to a wall thickness of 1.4 nm for FeO_x, consistent with what is expected from a 50-cycle ALD growth.

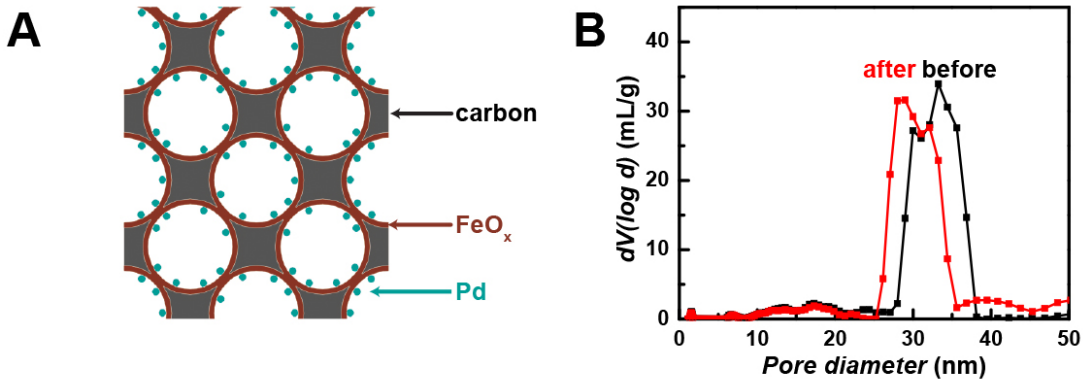

Figure 2.13 a) Illustration of FeOx and Pd deposition on 3DOm carbon b) pore size distribution of the 35 nm 3DOm carbon before and after FeO_x deposition

Second, the bright field transmission electron micrographs (TEM) before and after the ALD treatment (**Figure 2.14**) unambiguously confirm the deposition of FeO_x. With the deposition of 50 cycles of FeO_x, a relatively uniform and dense film can be observed on walls of 3DOm carbon indicated by increased contrast compared to the pristine carbon.

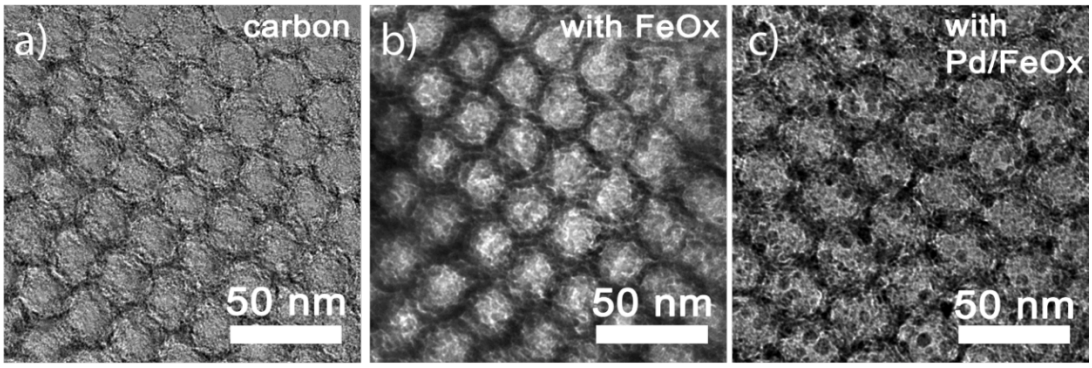

Figure 2.14 TEM images of a) pristine carbon, b) after ALD of FeOx and c) after the ALD of both FeOx and Pd

Lastly, Raman characterization was carried out to confirm the coating uniformity of FeO_x. According to control experiment on glass (red trace in **Figure 2.15**), FeO_x gave a series of characteristic peaks at low Raman shift region. The existence and distribution of FeO_x can also be visualized by Raman mapping, in which one can use one or multiple signature Raman shift peaks to observe how FeOx is distributed (**Figure 2.16**). The characteristic peaks existed at different depths of FeO_x coated electrodes indicates that the ALD growth of FeO_x was able to penetrate into the pores to produce coatings. The fact that the Raman maps of FeOx at different focal depths track those of carbon proves the uniform coating of FeOx on carbon surface.

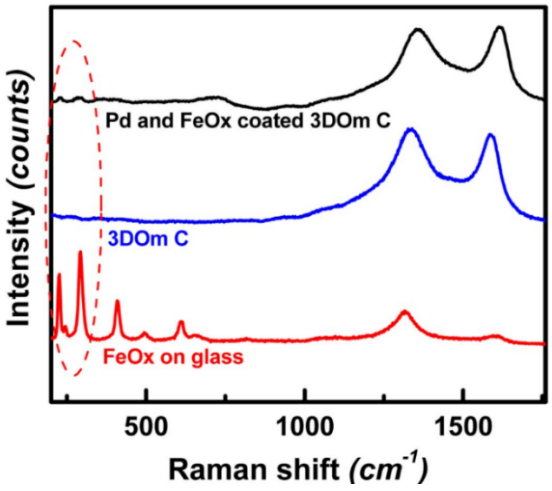

Figure 2.15 Raman characterization of Pd and FeO_x modified 3DOm carbon electrode.

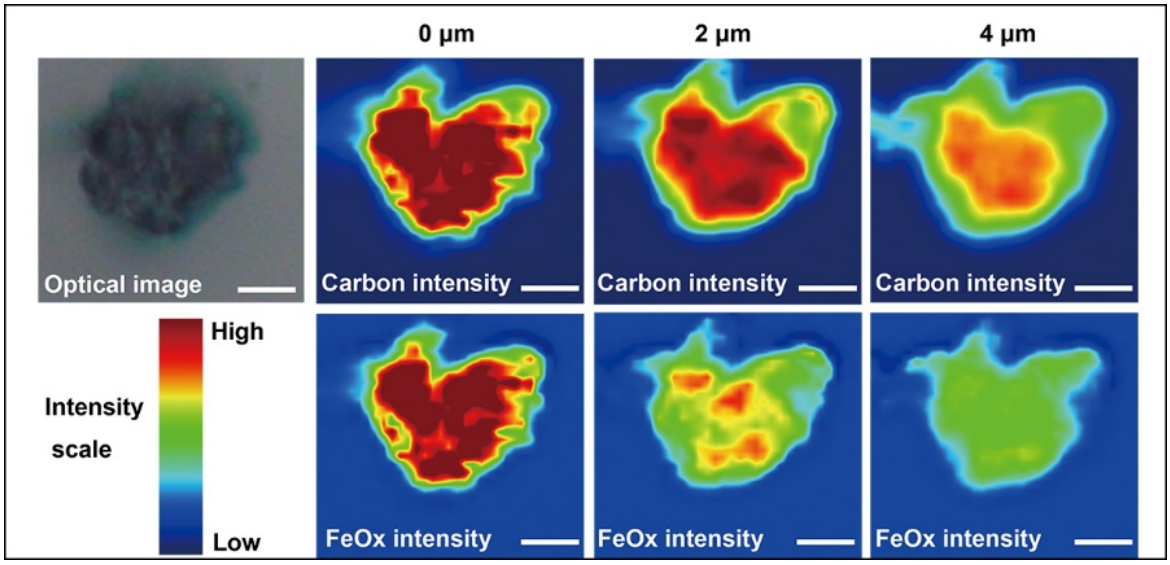

Figure 2.16 Raman mapping of FeO_x coated 3DOm carbon. Top left: optical image of the carbon particle studied. Top right panels: carbon signal mapping at 0, 2.0 μm, and 4.0 μm focal depth, respectively; bottom right panels: FeO_x signal mapping at the same depths. Scale bars: 5 μm.

Taken as a whole, the BET measurements, TEM micrographs, and Raman mapping confirm that the coverage of FeO_x on carbon is uniform. The uniform FeO_x coating is expected to provide a desired protection to minimize side reactions inherent to bare carbon surfaces.

The separation of carbon surface from reaction intermediates serves another important purpose. It hinders the well-recognized oxygen reduction reactions (ORR) activities of carbon. At the first glance, this may seem counterintuitive. After all, the first step of Li-O_2 battery discharge is to reduce oxygen. As such, the ORR activity of carbon would be a beneficial property. However, as shown in **Figure 2.17a** (upper panel), the ORR activity of carbon promotes Li_2O_2 formation randomly on the surface of carbon, at or away from oxygen evolution reactions (OER) sites. Note that OER catalysts are necessary to decompose Li_2O_2 at relatively low recharge overpotentials.[38] Li_2O_2 reside far away from OER sites are difficult to decompose, increasing the need for overpotentials and driving up the recharge potentials. Even worse, they may remain during the following cycles, accumulate, and eventually lead to capacity fading. The FeO_x coating is a known OER catalyst in aqueous systems.[3] We are therefore interested to examine whether they serve to decompose Li_2O_2 in nonaqueous electrolytes. As will be discussed next (also see **Figure 2.17b**), the OER activity of FeO_x in DME is indeed obvious. As such, their uniform presence on the carbon surface ensures complete decomposition of Li_2O_2 at relatively low overpotentials (**Figure 2.17a**, lower panel). To compensate for the loss of ORR activity, Pd nanoparticles, one of the best-known ORR catalysts in both aqueous and nonaqueous

electrolytes (**Figure 2.17a**),[20,39] were grown on the 3DOm carbon by ALD after the deposition of FeO_x. The success in growing uniform Pd nanoparticles within 3DOm carbon pores is confirmed by TEM in **Figure 2.14c**.

2.3.4 Pd/FeOx/3DOm performance

The efficacy of the above-outlined material design and preparation strategy is obvious. We see in **Figure 2.17b** that the average discharge potential measured on bare 3DOm carbon was 2.76 V (vs Li^+/Li), representing an overpotential of 0.20 V. The overpotential increased to 0.26 V when carbon was covered by FeO_x, but dropped back to 0.23 V with Pd decorations. Similarly, bare 3DOm carbon exhibited high recharge overpotentials (0.82 V). Adding Pd led to a reduction to 0.68 V because Pd is a moderately effective OER catalyst as well. The presence of FeO_x enabled the greatest overpotential reduction, with or without Pd (0.48 V and 0.51 V, respectively). The result strongly supports that OER were primarily catalyzed by FeO_x but not Pd, a desired feature of the material design principle as shown in **Figure 2.17a**.

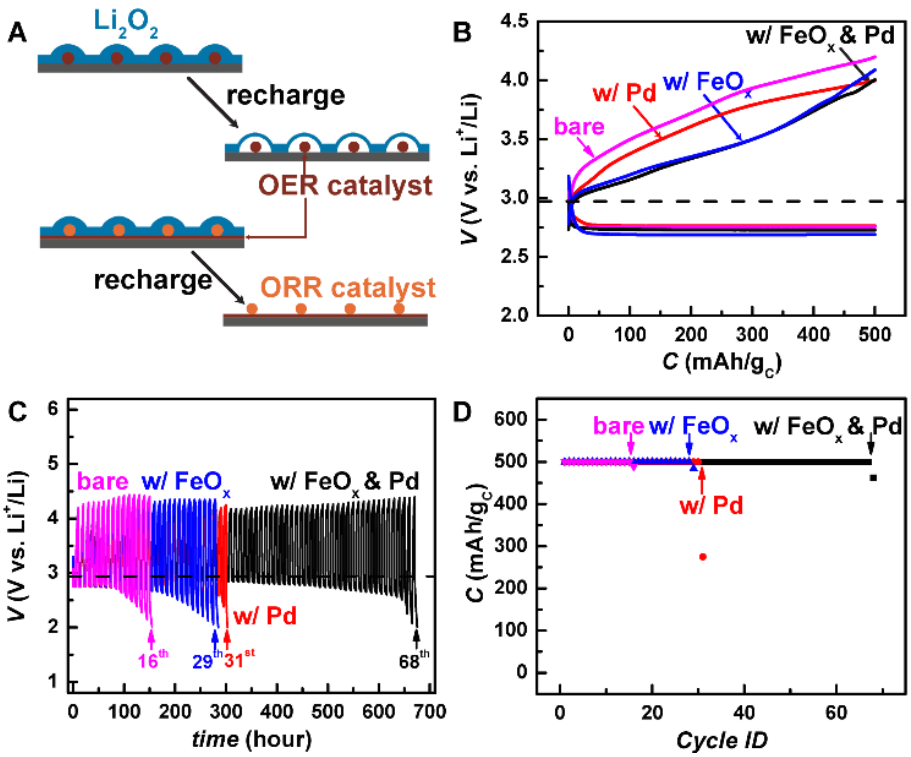

Figure 2.17 Effect of FeO_x and Pd decoration on 3DOm carbon. A. Without FeO_x, carbon inherently promotes ORR, producing Li_2O_2 far away from OER sites that are difficult to decompose. FeO_x coating serves as OER catalyst. When combined with ORR catalysts such as Pd, the decomposition of Li_2O_2 can be more complete. B. The understanding as shown in (A) is supported by the 1st cycle discharge/recharge characteristics. (Current density: 100mA/g_C) C & D. More complete decomposition of Li_2O_2 corresponds to better cyclability in the deep discharge/recharge cycles.)

The most important goal we hope to meet by adding FeO_x and Pd is to increase cyclabilities of Li-O_2 battery operations, because better controls over Li_2O_2 formation and decomposition are expected to correspond to better cyclability. To evaluate the cathode

performance and in accordance with practices most commonly reported in the literature, we limited the capacity at 500 mAh/g and recorded the voltage-capacity behaviors as shown in **Figure 2.17c**. When the discharge potential dropped below 2.0 V, we considered the cell to have failed. It is seen in **Figure 2.17c & 2.17d** that bare 35nm 3DOm carbon cathode failed after the 16^{th} cycle; addition of Pd improved the cyclability to the 31^{st} cycle, presumably through the OER properties of Pd; the presence of FeO_x significantly stabilized the cathode, and the cell did not fail until the 68^{th} cycle, which is the highest cycling numbers obtained on carbon-based cathode support in DME-based electrolyte, to the best of our knowledge. Because the decomposition of all known and tested electrolyte systems is a recognized issue, the eventual degradation of the cell performance is expected. Within this context, we are excited to see that the lifetime of a carbon cathode is extended by more than 4-fold by a simple FeO_x coating and Pd decoration.

We next set out to confirm that the measured performance is indeed as a result of the formation and decomposition of Li_2O_2. First, X-ray diffraction (XRD, **Figure 2.18a**) unambiguously confirmed the formation of Li_2O_2 upon discharge. The peaks at 32.9°, 35.0° and 40.7° agreed well with documented diffraction peaks of Li_2O_2 (JCPDS 74-0115). Notably, no peaks corresponding to Li_2CO_3, an important undesired by-product of Li-O_2 operation, were found in the XRD pattern. Upon recharge, the Li_2O_2 diffraction peaks disappeared. Significantly, at the 61^{st} cycles, the diffraction peaks of Li_2O_2 were still prominent while no Li_2CO_3 peaks were observed. Next, X-ray photoelectron spectroscopy (XPS) was used to confirm the existence of Li_2O_2 from O 1s spectra

(**Figure 2.18b**). Before discharge, only species corresponding to iron oxide were identified: the peak located at 529.9 eV is attributed to O^{2-} in the lattice of Fe_2O_3 and the peak at 531.7eV to surface hydroxide terminal groups on Fe_2O_3. A third, much less prominent broad peak at 534.2 eV was assigned to Pd $3p_{3/2}$ of oxides on Pd nanoparticle surfaces. After discharge, three distinct peaks were obtained. Among them, the peak at 529.9 eV (from iron oxide) remained unchanged. At 531.9 eV was a new, most significant peak corresponding to Li_2O_2. The peak at 533.4 eV increased in intensity. It can be assigned to O in Li_2CO_3 due to the short exposure of sample to the ambient air before loading into the XPS instrument. Upon recharge, the spectrum was nearly identical to before discharge.

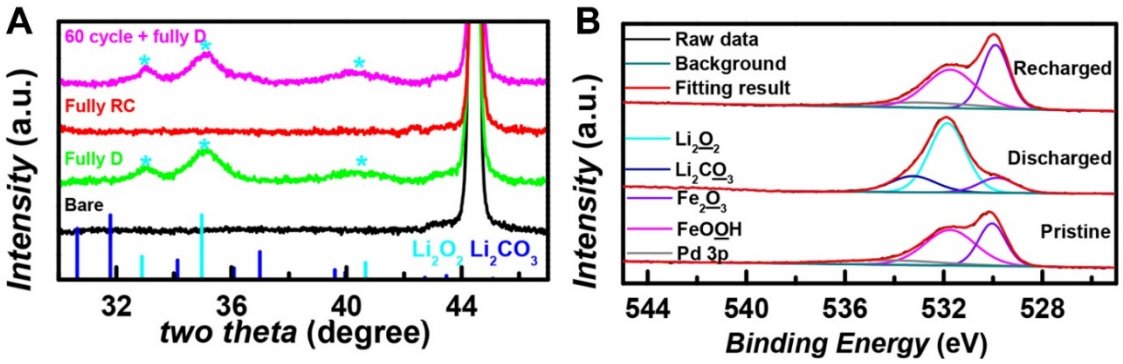

Figure 2.18 Product detection. A. X-ray diffraction peaks before discharge (black), after the 1st cycle discharge (green), the 1st cycle recharge (red), and fully discharged after 60 cycles of operations (purple). B. X-ray photoelectron spectra before discharge (bottom), after discharge (middle), and after recharge (top). The assignment of deconvoluted peaks are color-coded and labelled in the viewgraph, with the element of interest underlined (e.g., O peaks in Li_2O_2 labelled as $Li_2\underline{O_2}$).

Third, differential electrochemical mass spectrometry (DEMS) was used to quantify the gaseous recharge product **(Figure 2.19)**. For this set of experiments, tetraethylene glycol dimethyl ether (TEGDME) was chosen as the electrolyte solvent for its relatively low vapor pressures. During the 1st cycle recharge, O_2 accounted for 96.6% of the total gas evolved. Despite the protection, CO_2 was detected (3.4% of the total amount) (**Figure 2.19a**). It is noted that O_2 diffusion coefficient in TEGDME (2.17×10^{-6} cm^2/s) is lower than in dimethoxyethane (DME; 1.22×10^{-5} cm^2/s),[33] which was the primary solvent used for all characterizations other than DEMS. Consequently, the average recharge potentials in TEGDME (3.69 V) was greater than in DME (3.44 V). We therefore expect more severe side reactions when TEGDME is used. Nontheless, CO_2 generation from the protected carbon is clearly less than the unprotected one (**Figure 2.19b**), proving the effectiveness of carbon protection for inhibiting the side reactions.

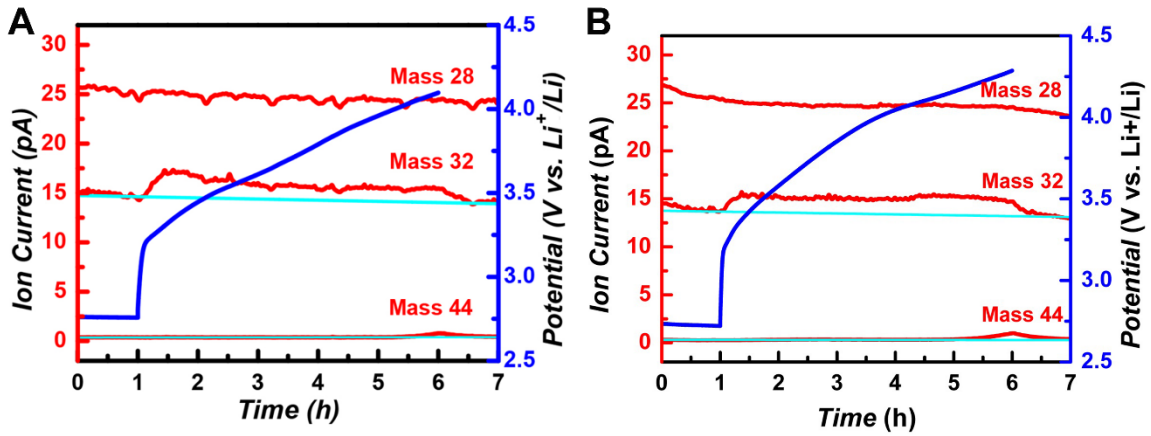

Figure 2.19 Mass-spectrometry detection of N_2 as a control (mass 28), O_2 (mass 32), and CO_2 (mass 44). The corresponding voltages were plotted against the right axis. (A) Pd/FeOx/3DOm carbon (B) Prinstine 3DOm carbon

2.4 Conclusions

Before the full potentials of Li-O_2 can be materialized, significant advances in many areas, including the discovery of stable electrolytes and anodes, are necessary. Among them, controls over the product (Li_2O_2 in the case of Li-O_2 battery) formation and decomposition are critical. Availability of material platforms that can enable detailed studies of the processes will contribute significantly to this field. Within this context, 3DOm carbon offers unprecedented opportunities. The demonstrated high capacity and preferred deposition within the large pores of 3DOm carbon build a foundation for high performance Li-O_2 battery operations. A facile FeO_x ALD growth, in conjunction with ORR catalyst decorations of ligand-free Pd nanoparticles, readily addresses the inherent reactivity of carbon and extends the cyclability from 16 to 68. Importantly, the 3DOm carbon platform allows for control over the size and location of Li_2O_2 deposition. We anticipate 3DOm carbon to play an increasingly more important role in the field energy storage.

2.5 References

[1] Yokoi, T.; Sakamoto, Y.; Terasaki, O.; Kubota, Y.; Okubo, T.; Tatsumi, T., Periodic Arrangement of Silica Nanospheres Assisted by Amino Acids. *J. Am. Chem. Soc.* **2006**, *128*, 13664.

[2] Fan, W.; Snyder, M. A.; Kumar, S.; Lee, P.-S.; Yoo, W. C.; McCormick, A. V.; Lee Penn, R.; Stein, A.; Tsapatsis, M., Hierarchical nanofabrication of microporous crystals with ordered mesoporosity. *Nat. Mater.* **2008**, *7*, 984.

[3] Lin, Y.; Zhou, S.; Sheehan, S. W.; Wang, D., Nanonet-Based Hematite Heteronanostructures for Efficient Solar Water Splitting. *J. Am. Chem. Soc.* **2011**, *133*, 2398.

[4] Lin, Y.; Xu, Y.; Mayer, M. T.; Simpson, Z. I.; McMahon, G.; Zhou, S.; Wang, D., Growth of p-Type Hematite by Atomic Layer Deposition and Its Utilization for Improved Solar Water Splitting. *J. Am. Chem. Soc.* **2012**, *134*, 5508.

[5] Du, C.; Yang, X.; Mayer, M. T.; Hoyt, H.; Xie, J.; McMahon, G.; Bischoping, G.; Wang, D., Hematite-Based Water Splitting with Low Turn-On Voltages. *Angew. Chem. Int. Ed.* **2013**, *52*, 12692.

[6] Lu, Y.-C.; Gasteiger, H. A.; Parent, M. C.; Chiloyan, V.; Shao-Horn, Y., The Influence of Catalysts on Discharge and Charge Voltages of Rechargeable Li-Oxygen Batteries. *Electrochem. Solid State Lett.* **2010**, *13*, A69.

[7] Abraham, K. M.; Jiang, Z., A Polymer Electrolyte-Based Rechargeable Lithium/Oxygen Battery. *J. Electrochem. Soc.* **1996**, *143*, 1.

[8] Hartmann, P.; Bender, C. L.; Vračar, M.; Dürr, A. K.; Garsuch, A.; Janek, J.; Adelhelm, P., A rechargeable room-temperature sodium superoxide (NaO_2) battery. *Nat. Mater.* **2013**, *12*, 228.

[9] Ren, X.; Wu, Y., A Low-Overpotential Potassium-Oxygen Battery Based on Potassium Superoxide. *J. Am. Chem. Soc.* **2013**, *135*, 2923.

[10] Li, Y.; Dai, H., Recent advances in zinc-air batteries. Chem. Soc. Rev. 2014, 43, 5257.

[11] McCloskey, B. D.; Bethune, D. S.; Shelby, R. M.; Girishkumar, G.; Luntz, A. C., Solvents' Critical Role in Nonaqueous Lithium-Oxygen Battery Electrochemistry. *J. Phys. Chem. Lett.* **2011**, *2*, 1161.

[12] Lu, Y.-C.; Gallant, B. M.; Kwabi, D. G.; Harding, J. R.; Mitchell, R. R.; Whittingham, M. S.; Shao-Horn, Y., Lithium-oxygen batteries: bridging mechanistic understanding and battery performance. *Energy Environ. Sci.* **2013**, *6*, 750.

[13] McCloskey, B. D.; Speidel, A.; Scheffler, R.; Miller, D. C.; Viswanathan, V.; Hummelshøj, J. S.; Nørskov, J. K.; Luntz, A. C., Twin Problems of Interfacial Carbonate Formation in Nonaqueous Li–O2 Batteries. *J. Phys. Chem. Lett.* **2012**, *3*, 997.

[14] McCloskey, B. D.; Bethune, D. S.; Shelby, R. M.; Mori, T.; Scheffler, R.; Speidel, A.; Sherwood, M.; Luntz, A. C., Limitations in Rechargeability of Li-O_2 Batteries and Possible Origins. *J. Phys. Chem. Lett.* **2012**, *3*, 3043.

[15] Ottakam Thotiyl, M. M.; Freunberger, S. A.; Peng, Z.; Bruce, P. G., The Carbon Electrode in Nonaqueous Li-O_2 Cells. *J. Am. Chem. Soc.* **2013**, *135*, 494.

[16] Xu, J.-J.; Wang, Z.-L.; Xu, D.; Zhang, L.-L.; Zhang, X.-B., Tailoring deposition and morphology of discharge products towards high-rate and long-life lithium-oxygen batteries. *Nat. Commun.* **2013**, *4*, 2438.
[17] Gallant, B. M.; Kwabi, D. G.; Mitchell, R. R.; Zhou, J.; Thompson, C. V.; Shao-Horn, Y., Influence of Li_2O_2 morphology on oxygen reduction and evolution kinetics in Li-O_2 batteries. *Energy Environ. Sci.* **2013**, *6*, 2518.
[18] Yilmaz, E.; Yogi, C.; Yamanaka, K.; Ohta, T.; Byon, H. R., Promoting Formation of Noncrystalline Li_2O_2 in the Li-O_2 Battery with RuO_2 Nanoparticles. *Nano Lett.* **2013**, *13*, 4679.
[19] Adams, B. D.; Radtke, C.; Black, R.; Trudeau, M. L.; Zaghib, K.; Nazar, L. F., Current density dependence of peroxide formation in the Li-O_2 battery and its effect on charge. *Energy Environ. Sci.* **2013**, *6*, 1772.
[20] Lu, J.; Lei, Y.; Lau, K. C.; Luo, X.; Du, P.; Wen, J.; Assary, R. S.; Das, U.; Miller, D. J.; Elam, J. W.; Albishri, H. M.; El-Hady, D. A.; Sun, Y.-K.; Curtiss, L. A.; Amine, K., A nanostructured cathode architecture for low charge overpotential in lithium-oxygen batteries. *Nat. Commun.* **2013**, *4*, 2383.
[21] Xie, J.; Yao, X.; Madden, I. P.; Jiang, D.-E.; Chou, L.-Y.; Tsung, C.-K.; Wang, D., Selective Deposition of Ru Nanoparticles on $TiSi_2$ Nanonet and Its Utilization for Li_2O_2 Formation and Decomposition. *J. Am. Chem. Soc.* **2014**, *136*, 8903.
[22] Kang, S. J.; Mori, T.; Narizuka, S.; Wilcke, W.; Kim, H.-C., Deactivation of carbon electrode for elimination of carbon dioxide evolution from rechargeable lithium–oxygen cells. Nat. Commun. 2014, 5, 3937.
[23] Peng, Z.; Freunberger, S. A.; Chen, Y.; Bruce, P. G., A Reversible and Higher-Rate Li-O_2 Battery. *Science* **2012**, *337*, 563.
[24] Cychosz, K. A.; Guo, X.; Fan, W.; Cimino, R.; Gor, G. Y.; Tsapatsis, M.; Neimark, A. V.; Thommes, M., Characterization of the Pore Structure of Three-Dimensionally Ordered Mesoporous Carbons Using High Resolution Gas Sorption. *Langmuir* **2012**, *28*, 12647.
[25] Guo, Z.; Zhou, D.; Dong, X.; Qiu, Z.; Wang, Y.; Xia, Y., Ordered Hierarchical Mesoporous/Macroporous Carbon: A High-Performance Catalyst for Rechargeable Li–O_2 Batteries. *Adv. Mater.* **2013**, *25*, 5668.
[26] Ding, N.; Chien, S. W.; Hor, T. S. A.; Lum, R.; Zong, Y.; Liu, Z., Influence of carbon pore size on the discharge capacity of Li-O_2 batteries. *J. Mater. Chem. A* **2014**, *2*, 12433.
[27] Jian, Z.; Liu, P.; Li, F.; He, P.; Guo, X.; Chen, M.; Zhou, H., Core-Shell-Structured CNT@RuO_2 Composite as a High-Performance Cathode Catalyst for Rechargeable Li-O_2 Batteries. *Angew. Chem. Int. Ed.* **2014**, *53*, 442.
[28] Sun, B.; Huang, X.; Chen, S.; Munroe, P.; Wang, G., Porous Graphene Nanoarchitectures: An Efficient Catalyst for Low Charge-Overpotential, Long Life, and High Capacity Lithium-Oxygen Batteries. *Nano Lett.* **2014**, *14*, 3145.
[29] Franco, A. A.; Xue, K.-H., Carbon-Based Electrodes for Lithium Air Batteries: Scientific and Technological Challenges from a Modeling Perspective. *ECS J. Solid State Sci. Technol.* **2013**, *2*, M3084.
[30] Gerbig, O.; Merkle, R.; Maier, J., Electron and Ion Transport In Li_2O_2. *Adv. Mater.* **2013**, *25*, 3129.

[31] Geng, W. T.; He, B. L.; Ohno, T., Grain Boundary Induced Conductivity in Li_2O_2. *J. Phys. Chem. C* **2013**, *117*, 25222.
[32] Andrei, P.; Zheng, J. P.; Hendrickson, M.; Plichta, E. J., Some Possible Approaches for Improving the Energy Density of Li-Air Batteries. *J. Electrochem. Soc.* **2010**, *157*, A1287.
[33] Laoire, C. O.; Mukerjee, S.; Abraham, K. M.; Plichta, E. J.; Hendrickson, M. A., Influence of Nonaqueous Solvents on the Electrochemistry of Oxygen in the Rechargeable Lithium-Air Battery. *J. Phys. Chem. C* **2010**, *114*, 9178.
[34] Read, J.; Mutolo, K.; Ervin, M.; Behl, W.; Wolfenstine, J.; Driedger, A.; Foster, D., Oxygen Transport Properties of Organic Electrolytes and Performance of Lithium/Oxygen Battery. *J. Electrochem. Soc.* **2003**, *150*, A1351.
[35] Itkis, D. M.; Semenenko, D. A.; Kataev, E. Y.; Belova, A. I.; Neudachina, V. S.; Sirotina, A. P.; Hävecker, M.; Teschner, D.; Knop-Gericke, A.; Dudin, P.; Barinov, A.; Goodilin, E. A.; Shao-Horn, Y.; Yashina, L. V., Reactivity of Carbon in Lithium-Oxygen Battery Positive Electrodes. *Nano Lett.* **2013**, *13*, 4697.
[36] McCloskey, B. D.; Valery, A.; Luntz, A. C.; Gowda, S. R.; Wallraff, G. M.; Garcia, J. M.; Mori, T.; Krupp, L. E., Combining Accurate O_2 and Li_2O_2 Assays to Separate Discharge and Charge Stability Limitations in Nonaqueous Li-O_2 Batteries. *J. Phys. Chem. Lett.* **2013**, *4*, 2989.
[37] Ottakam Thotiyl, M. M.; Freunberger, S. A.; Peng, Z.; Chen, Y.; Liu, Z.; Bruce, P. G., A stable cathode for the aprotic Li-O_2 battery. *Nat. Mater.* **2013**, *12*, 1050.
[38] Black, R.; Lee, J. H.; Adams, B.; Mims, C. A.; Nazar, L. F., The Role of Catalysts and Peroxide Oxidation in Lithium-Oxygen Batteries. *Angew. Chem. Int. Ed.* **2013**, *52*, 392.
[39] Lu, Y.-C.; Gasteiger, H. A.; Shao-Horn, Y., Catalytic Activity Trends of Oxygen Reduction Reaction for Nonaqueous Li-Air Batteries. *J. Am. Chem. Soc.* **2011**, *133*, 19048.

Chapter 3 The Parasitic Chemistries and Their Synergistic Effect in Li-O_2 Batteries

3.1 Introduction

Based on the reversible formation and decomposition of Li_2O_2, aprotic Li-O_2 batteries hold great promise to meet the societal needs for high-capacity energy storage in areas such as electric vehicles.[1] The theoretical specific energy can reach 3505 Wh/kg, much higher than other energy storage systems such as lithium ion (Li-Ion, 387 Wh/kg) and lithium sulfur (Li-S, 2567 Wh/kg).[2] Originally reported in 1996,[3] this technology gained significant attention since 2006.[4] Continued research, nevertheless, has revealed a number of important issues that limit further development of Li-O_2 batteries into a practical technology.[5,6] These issues include poor stabilities of all components of the test cells – the anode, the electrolyte and the cathode.[7-9] Additionally, much higher recharge potentials than discharge ones are often necessary, limiting the achievable energy efficiencies.[10] These issues and their chemical origins have been the topic of numerous recent review articles.[11-13] Briefly, it is generally recognized that carbon is an unstable cathode material that can be readily corroded during cell operations (for both discharge and recharge, but more so for the recharge process).[14-16] No stable electrolytes have been identified, although DME (dimethoxyethane), TEGDME (tetraethylene glyco dimethyl ether) and DMSO (dimethtylsulfoxide) have been popularly used.[17-19] Without a stable solid-electrolyte-interface (SEI) layer, Li as an anode material faces critical problems.[20] But replacing it with other Li-containing materials will greatly reduce the achievable capacities, undermining

the potentials held by Li-O_2 batteries.[21] The high overpotentials are responsible for the low round-trip efficiencies. While many catalytic materials have been studied and have shown promises for reducing the overptoentials, their role in the processes remains the subject of debates.[6,22-24] These challenges notwithstanding, intense research has significantly advanced our understanding on the chemical nature of Li-O_2 battery operations. While the parasitic chemistries at the anode, the cathode and within the electrolyte have received reasonable attention, the possible synergistic effects between them are rarely discussed and remain poorly understood. By focusing on the various parasitic chemistries, we find a clear sign of synergistic effect between them. The lack of attention to the possible synergistic effect may help explain why the progress on Li-O_2 battery research has been frustratingly sluggish. It points to the importance of system approaches in studying Li-O_2 batteries for future breakthroughs.

Key to the synergistic effect is the ubiquitous presence of O_2 and its reactive derivatives. For an ideal Li-O_2 battery, the electrolyte (liquid), the cathode support as well as the Li_2O_2 product (solid) and O_2 (gas) form a three-phase interface.[1] At this interface, oxygen reduction reactions (ORR) and oxygen evolution reactions (OER) take place. O_2 and its reactive derivatives are confined to this three-phase interface.[25] In reality, however, the cathode is typically flooded by the electrolyte, through which O_2 has to diffuse to reach the reactive sites during ORR and diffuse away during OER. Consequently, various reactive intermediates including superoxides and possible byproducts such as H^+ abound in the electrolyte.[13,26] The mixture of the electrolyte, O_2 and various reactive oxygen species

provides ample opportunities for chemical feedbacks by chemistries that should be separated, creating synergistic effects that are poorly understood to date. For a systematic understanding of the complex processes, we first summarize literature reports on electrolyte decomposition based on their reaction pathways and then examine the possible synergistic effects between electrolyte decomposition and parasitic chemistries involving the anode and the cathode, respectively. Such a treatment of existing knowledge offers us new insights into the parasitic chemistries that limit the development of Li-O_2 batteries, which will be presented later.

3.2 Decomposition Pathways of the Electrolytes

Due to the ORR and OER on the cathode and possible reactions between Li and dissolved O_2 (see section 3.4), reactive oxygen species (e.g., $O_2^{\cdot -}$, Li_2O_2 and $Li_{2-x}O_2$) are expected to co-exist with molecular O_2 in the electrolyte.[11,27] Their reactivity toward the electrolyte is a critical reason for the electrolyte decomposition.[28] In accordance with the literature conventions, here we focus on the reactivity of the solvents. The possible roles of salts in the electrolyte decomposition are not considered. For clarity, we categorize known electrolyte decomposition pathways into five groups, (1) nucleophilic attacks, (2) auto-oxidation, (3) acid-base reactions, (4) proton-mediated reactions, and (5) reduction by Li. The categorization is summarized in **Figure 3.1** and will be discussed in details next.

3.2.1 The role of oxygen species in nucleophilic attack

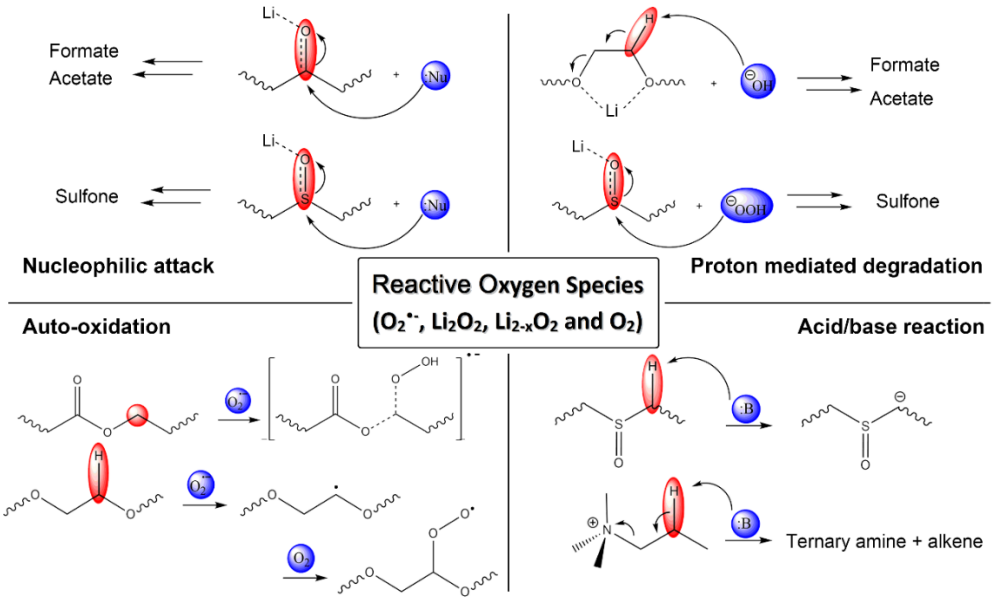

Figure 3.1 Pathways of electrolyte decomposition by reactive oxygen species.

The desired product of O_2 reduction in an aprotic Li-O_2 battery is Li_2O_2.[3] As a nucleophile, its reactivity toward functional groups such as sulfoxides (S=O) and carbonyls (C=O) is known.[29,30] A more problematic species toward electrolyte decomposition is $O_2^{\cdot-}$, which is an important intermediate during both ORR and OER.[31,32] As an intermediate, $O_2^{\cdot-}$ has been found not only at the cathode support where ORR and OER take place,[26] but also in the electrolyte as solvated species.[32,33] These reactive species serve as a promoter to the electrolyte decomposition. Indeed, carbonates used in early Li-O_2 battery studies were found to decompose severely due to the nucleophilic attacks by $O_2^{\cdot-}$ to the C=O groups, producing Li alkyl carbonates and Li_2CO_3.[34] Computational studies have shown that other esters face similar issues.[35] DMSO has been explored by the Bruce group as an electrolyte for better stability against nucleophilic attacks than carbonates.[18] Its high donor numbers were also found to enable low discharge overpotentials and high discharge

capacities.[33] However, research by Shao-Horn and Aurbach et al. and others revealed that sulfoxide is susceptible to nucleophilic attacks by reduced oxygen species, as well.[29,31] Compared to ester and sulfoxide, amide is a weaker electron withdrawing group and has been studied for their potential as a stable electrolyte toward nucleophilic attacks.[35-37] The expectation is supported by computational calculations showing higher free energy barrier than DMSO and esters.[35,36] Experimental results on the stability of amides against nucleophilic attacks, however, are not conclusive.[38,39]

3.2.2 The role of oxygen species in auto-oxidation

One class of electrolyte, the ethereal-based ones such as DME and TEGDME, is notable for their stability against nucleophiles owing to the lack of electron-withdrawing functional groups in their molecular structures. As a result, they have become the most widely used electrolytes in recent Li-O_2 literatures.[40] Their reactivity toward auto-oxidation,[19] nevertheless, presents significant problems (**Figure 3.2**). For example, the α-H in ethers has been shown reactive toward superoxide radicals.[41] In fact, Shao-Horn et al. have shown that simple mixture of ethers with molecular O_2 leads to auto-oxidation through α-H abstraction.[42] These reactions further promote the release of protons, esterification and polymerization, leading to severe decomposition of the electrolyte. The detection of byproducts such as formate and acetate supports the auto-oxidation mechanism.[43] As far as auto-oxidation is concerned, superoxide radicals are not the only reactive species. Molecular oxygen has been shown to promote similar reactions as well. For instance,

polyether-based electrolytes suffer auto-oxidation initiated by dissolved molecular oxygen.[42] The auto-oxidation of the α or β positions also contributes to the decomposition of carbonates.[34] It has been predicted by computational studies that auto-oxidation may be a general decomposition pathway, presenting a significant challenge in the development of stable electrolyte systems for Li-O_2 batteries. The issue is especially severe for ether-based electrolytes.

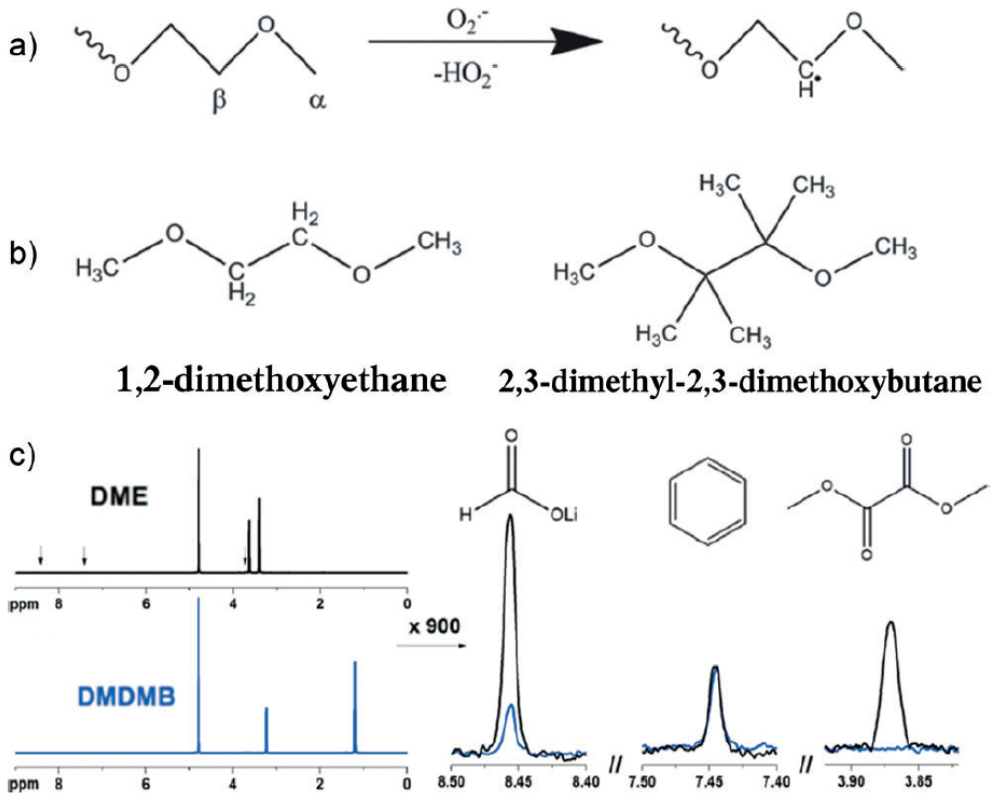

Figure 3.2 Electrolyte decomposition by auto-oxidation. a) Reaction mechanism of auto-oxidation of ethers. b) Methylation of the susceptible position. c) NMR result of DME decomposition and protection effect by methylation. Reproduced with permission from Ref. [19]. Copyright 2014 Wiley-VCH.

3.2.3 The role of oxygen species in acid/base reactions

The reduced oxygen species are strong Lewis bases in aprotic environments. They tend to attack the α- or β-H following an acid-base chemistry mechanism. The reactivity is enhanced by the presence of polarizing functional groups such as sulfoxide or charged atoms.[44] Considering DMSO as an example, its α position can be readily deprotonated by superoxides and peroxides, including those in their solid forms (Li_2O_2, $Li_{2-x}O_2$; see **Figure 3.3**).[29,45] The resulting anions lead to further degradation of the electrolyte, consuming the intermediates or the final products or both and lowering the Coulombic efficiencies. Such an acid-base pathway is a main mechanism for the decomposition of ionic liquids, which were originally adopted for their low vapour pressure, low flammability, low H_2O content and possible better stability against oxidation. However, as early as in 2012, McCloskey et al. evaluated the performance of several ionic liquids and raised questions about the stabilities of the cations.[10] In those experiments, H_2 was detected as a major gas phase byproduct during discharge, pointing to a β-H elimination mechanism by acid-base chemistry. Two recent studies by the Gasteiger group provided strong evidence to support the decomposition pathways of $PYR_{14}TFSI$ (1-butyl-1-methylpyrrolidinium bis(trifluoromethanesulfonyl)imide) following the Hofmann elimination mechanism.[46,47] As a soft acid, PYR cation interacts favourably with superoxide, which is a soft base, according to the half-soft-acid-base (HSAB) theory.[48] This interaction helps stabilize superoxide in the electrolyte, promoting OER reactions following a one-electron process. Consequently, low recharge overpotentials are measured.[32] The relatively high

concentration of superoxide in PYRTFSI, nonetheless, also promotes β-H elimination of PYR cation by the superoxide, leading to the decomposition of the electrolyte.[32,47]

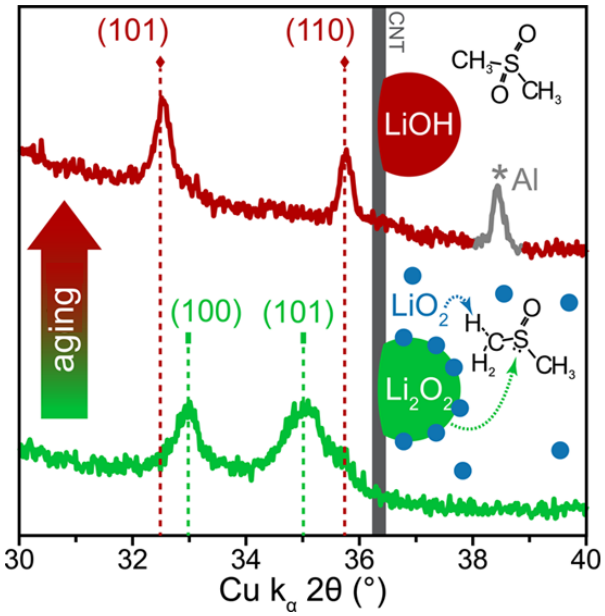

Figure 3.3 XRD results showing that reduced oxygen species (Li_2O_2 and LiO_2) attack DMSO resulting in LiOH formation. Reproduced with permission from Ref. [29]. Copyright 2014 ACS.

3.2.4 The role of oxygen species in proton mediated degradation

Despite the best efforts to remove H_2O from the electrolyte, H_2O has been an inevitable impurity in all electrolytes reported in the literature. It is an important source of protons, which interact strongly with oxygen species such as superoxides and peroxides. These interactions produce protonated superoxides, peroxides and hydroxides that are nucleophiles and strong bases. They participate in the various decomposition reactions of the electrolyte as discussed above. Moreover, the strong interactions between protons and

reduced oxygen species help dissolve the latter, further enhancing electrolyte decomposition by reactive oxygen species.[49] Indeed, it has been shown that the existence of proton accelerates the degradation of the electrolytes, leading to the formation of formate and acetate byproducts.[50] Worse, the decomposition reactions liberate more protons to exacerbate the degradation of the electrolyte in a self-accelerating fashion.

3.2.5 The reduction susceptibility by Lithium

As will be discussed more later, Li is a necessary component in order to actualize the potentials of Li-O_2 batteries as a high-capacity energy storage technology. Its reactivity with the electrolyte and dissolve oxygen species is therefore an important consideration that must be taken into account. The reactivity of Li with oxygen species will be further discussed in Section 3.4. Here we focus our discussions on the direct reactions between Li and the electrolyte. The reactivity originated from the highly reducing nature of Li leads to the decomposition of most known electrolytes.[20] For instance, ethers and carbonates have been shown to be decomposed by Li upon contact, forming insoluble byproducts such as lithium oxides, carbonates, alkyl carbonates and hydroxides.[20,51] These byproducts deposit onto Li to form a compact film that prevents further direct contact between Li and the electrolyte, effectively limiting the reactions. Furthermore, this film is electronically insulating but allows for diffusion of Li^+, serving as a solid-electrolyte-interface (SEI) layer.[52] Such a feature permits the utilization of Li anode for Li-O_2 test cells. However, no known stable SEI formation has been reported for certain electrolyte systems such as

amides or DMSO.[36] These electrolytes have attracted attention for their potential resistivity against oxygen species. The reactivity of these electrolytes toward Li is therefore a challenge that must be addressed. Promising results have already been obtained by additives such as $LiNO_3$.[37,53]

3.2.6 Summary of electrolyte decomposition and outlook of future efforts

Previous reviews have mostly treated the electrolyte systems based on their chemical structures.[6,8] The categorization based on the various decomposition pathways as summarized above is new. The knowledge presented here is not limited to the reactive oxygen species, but also applicable to other radicals or anions that might exist in the system, such as redox mediators, dissolution of metal catalysts or electrolyte decomposition intermediates. To facilitate the understanding of the systems, we further list different discussions in **Table 3.1**, where the mechanisms and chemical structures are correlated for easy reading. These efforts provide us with new insight into the role of oxygen species on the decomposition of the electrolytes. It is conceivable that ethers can be stabilized by the substitution of the H on the carbon backbone with inert groups such $–CH_3$. This hypothesis has been recently verified by experimental efforts by Nazar et al.[19] Similarly, the methylation of β positions on PYR cation may improve the stability of the related ionic liquid cation. Nevertheless, the synthesis and purification of modified electrolytes may incur high cost, which can be an issue for practical applications. In addition, the

introduction of bulky substitution groups may decrease the oxygen diffusivity, leading to high overpotentials.

Table 3.1 Electrolytes decomposition pathways

	Li_2O_2	$O_2^{\bullet-}$	Li	O_2
Carbonate	--	B, N, O[30,34]	--	--
Ether/polyether	--	O, P[19,41,43,44]	--	O
DMSO	B,[31] N[29]	B,[31] N,[29] P[45]	R	--
Ionic liquid	--	B[46,47]	R	--
Amide	--	N[38,39]	R	--

Notes: N: Nucleophilic attack; B: Acid/base reaction; O: Auto-oxidation; P: Proton mediated process; R: Reduction by Li

3.3 Synergistic Effects at the Cathode

As the primary site for Li_2O_2 formation and decomposition, the cathode is the most studied component in Li-O_2 batteries. It has also been the subject of numerous reviews.[5,11,54-56] Instead of repeating these disucssions, here we focus on the synergistic effect between the cathode and the electrolyte, an aspect that has received underwhelming attention previously. It is shown here that the parasitic chemistries at the cathode and those

in the electrolyte have important influences on each other.[57] For instance, the reaction mechanisms at the cathode are found to be sensitive to the electrolyte choices. The decomposition chemistries on the cathode surface in turn contribute significantly to the electrolyte decomposition.

3.3.1 The cathode reaction pathways influenced by the electrolyte

The reactions taking place at the cathode (both ORR during discharge and OER during recharge) generate reactive oxygen species that promote parasitic chemistries. The detailed mechanisms by which these reactions proceed are highly sensitive to the nature of the electrolyte, as well. Below we discuss how the choice of electrolyte influences the reaction pathways at the cathode. The most representative pathway of the ORR involves the electrochemical reduction of an oxygen molecule to a superoxide anion ($O_2^{\cdot -}$). As a soft base, $O_2^{\cdot -}$ interacts strongly with Li^+, which is a hard acid, to disproportionate into Li_2O_2 and O_2. The one-electron electrochemical reaction features low overpotentials. Alternatively, LiO_2 may receive a second electron to be reduced to Li_2O_2, which corresponds to a 2-electron electrochemical reaction that features relatively high overpotentials.[33] Recent studies suggest that ORR favors the one-electron pathway when electrolytes with either high donor number (DN) or acceptor number (AN) are employed. For example, Aetukuri et al. found that the inclusion of trace amount of H_2O promotes the solution-based mechanism due to the strong Lewis acidity of H_2O (AN=54.8; see **Figure**

3.4a).[49] Johnson et al. demonstrated that electrolytes of high DNs favour ORR via the 1-electron pathway and enable high capacities and low overpotentials.[33] Nevertheless, the enhanced solubility of LiO_2 may increase the presence of superoxide species, which negatively impacts the stability of the electrolyte and the cathode following mechanisms as discussed in Section 3.2.[58-60] This effect has not been experimentally studied in the literature.

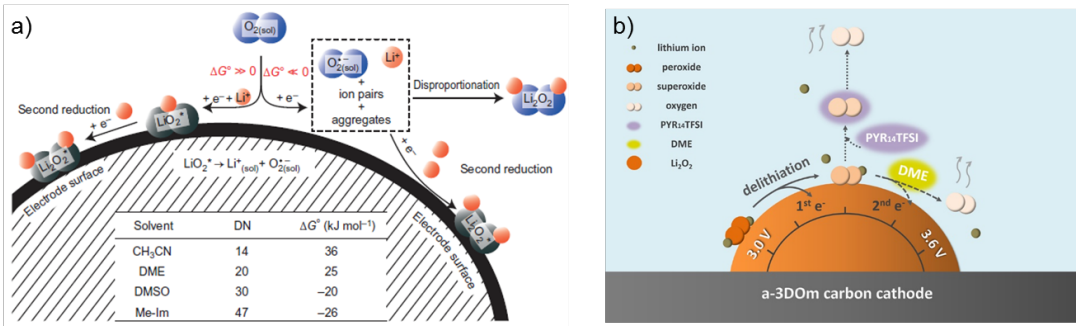

Figure 3.4 Schemes of the influence of electrolytes on the reaction pathways for the a) oxygen reduction reaction (ORR) and b) oxygen evolution reaction (OER; 3DOm carbon electrode=three-dimensionally ordered mesoporous carbon electrode). Reproduced with permission from Refs. [33] and [32]. Copyright 2014 NPG and 2015 ACS, respectively.

Similar influence by the electrolyte on the OER pathways during recharge has been recently observed, as well. For instance, ionic liquid ($PYR_{14}TFSI$) is found to help solvate superoxide species to favor the 1-electron recharge pathway (**Figure 3.4b**).[32] Correspondingly, low recharge overpotentials are measured. As far as overpotentials are concerned, it has been shown that H_2O in the electrolyte may serve as a mediator to facilitate charge transfer for low overpotentials.[61,62] More recently, it is reported that with

the help of H_2O, LiOH instead of Li_2O_2 may act as the discharge product for reversible recharge, which is a fundamentally different chemistry from that involving Li_2O_2 as discussed here.[63]

3.3.2 Synergistic effect between carbon cathode and electrolyte degradation

For the purpose of reducing overpotentials, researchers have examined a number of ORR and OER catalysts.[64,65] However, studies by McCloskey et al. showed that carbon loaded with catalysts, including Pt, MnO_2 and Au, would exhibit more CO_2 evolution than bare carbon, indicating that these catalysts may promote ether-based electrolyte decomposition (**Figure 3.5a**).[24] The issue of catalyst-promoted electrolyte decomposition should therefore be considered carefully for future studies.[22,66]

As a popularly used cathode material, porous carbon often features functional groups and defect sites that interact strongly with superoxide species following mechanisms as discussed in Section 3.2. The reactivity of carbon may also induce electrolyte decomposition (**Figure 3.5b**). For example, Bruce et al. observed that the extent of cathode and electrolyte decomposition is more severe for hydrophilic carbon than hydrophobic one due to the more abundant surface defects on the former.[16] When the carbon is deactivated by $LiNO_3$ additives, Kang et al. observed significantly supressed decomposition of not only the cathode, but also the electrolyte.[67] Indeed, greater stability has been consistently measured when carbon-free cathode is employed, either by coating carbon surface with

passivation (e.g., Al_2O_3, FeO_x) or by using non-carbon materials such as Au, $TiSi_2$ and TiC (**Figure 3.5b**).[18,68-72] Lu et al. examined the effect of Al_2O_3 coating using DFT calculations and proposed that the protective Al_2O_3 coating inhibited electrolyte decomposition on the defect sites.[68]

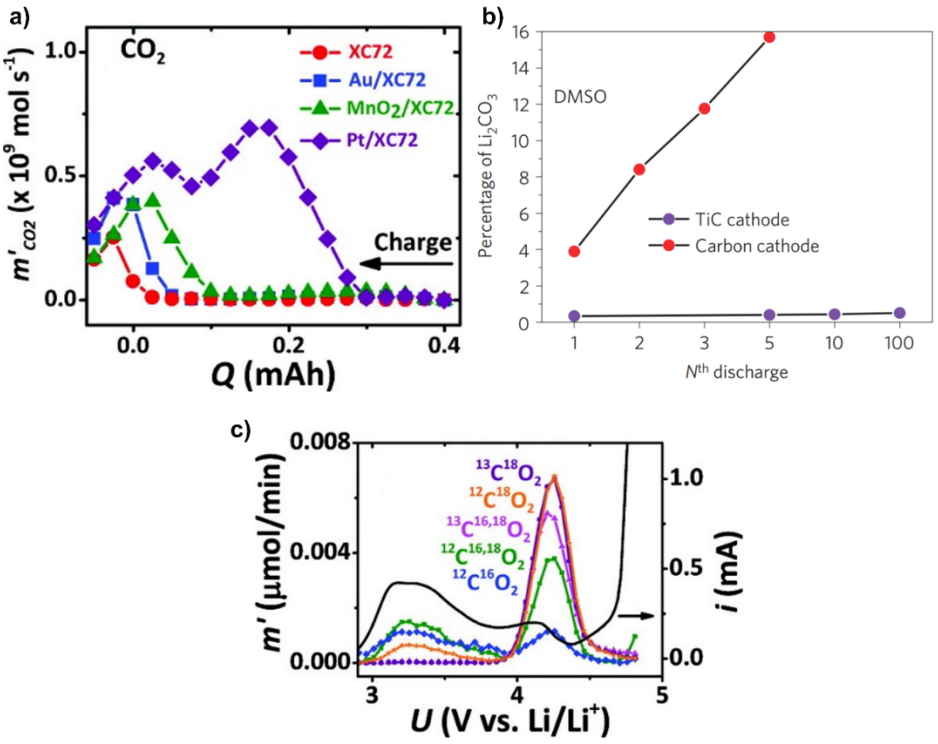

Figure 3.5 Synergistic effects between parasitic chemical reactions of the cathode and the electrolyte. a) The electrolyte decomposition is promoted by catalysts on the carbon cathode. b) Electrolyte decomposition is supressed when non-carbon cathode is used. c) Carbon decomposition is also promoted by the electrolytes. Reproduced with permission from Refs. [24], [72] and [15], respectively. Copyright 2011 ACS, 2013 NPG and 2012 ACS respectively.

The decomposition of electrolyte has been found to induce carbon decomposition under Li-O_2 operational conditions, as well.[57] By isotope labelling, McCloskey et al. found significant reactions between the electrolyte and the carbon cathode (**Figure 3.5c**).[15] Their results suggest that the highly reactive species formed as a result of the electrolyte decomposition can diffuse to the cathode surface and react with carbon. This result further highlights the importance of studying the cathode and electrolyte decomposition in a systematic fashion.

3.4 Parasitic Chemistries at the Li Anode

The desired reactions at the anode are the stripping (during discharge) and plating (during recharge) of Li.[3] Li metal is an obvious choice as an anode material. But the high reactivity and low redox potential of Li dictate that complex chemistries often take place when Li is in contact with other chemicals.[20] In principle, the negative impact of these chemistries can be circumvented by replacing Li with other Li-containing compounds, such as the approach employed in commercial LIBs.[73] For Li-O_2 batteries, however, replacing Li with other materials significantly undermines the achievable capacities.[21,74-76] As such, Li is the common anode material in nearly all published studies on Li-O_2 batteries. To date, little attention has been paid to the parasitic chemistries between Li and other components of the cell, including O_2, the electrolytes and the products of the O_2 reduction and electrolyte decomposition.[51,77,78] We will next address this issue by examining three common reactions at the Li anode, namely the reaction between Li and the electrolyte, the

reactivity of reduced oxygen species on Li surfaces and the reactions between oxygen species and the SEI layer.

3.4.1 Corrosion of Li by the electrolytes

As has been discussed in section 3.2, when the reactions between Li and electrolytes (e.g., DME, TEGDME and organic carbonates) are self-limiting, the insoluble products may serve as a pseudo-SEI layer to protect the Li anode.[52] These reactions will enable the utilization of Li as an anode material. Nevertheless, it is important to note that these SEI layers are only quasi-stable. Dendritic Li growth during recharge still poses significant challenges.[79] Indeed, corrosion of Li has been observed previously in TEGDME as a result of cycling (**Figure 3.6**), although it is unclear to what extent the anode corrosion contributes to the overall cell degradation.[77] When the reactions between Li and the electrolyte are not self-limiting, as is the case when DMA and DMSO are used as the electrolyte, the corrosion of Li is much more severe.[8] Unless stable artificial SEI layers can be achieved (see Section 3.5), these electrolytes are incompatible with Li.[18,53] Although the problem may be addressed by replacing Li with other Li-containing compounds,[74,75] such an approach would lead to significant reduction of cell voltages as well as increase of mass loading and therefore is not practical for Li-O_2 batteries.

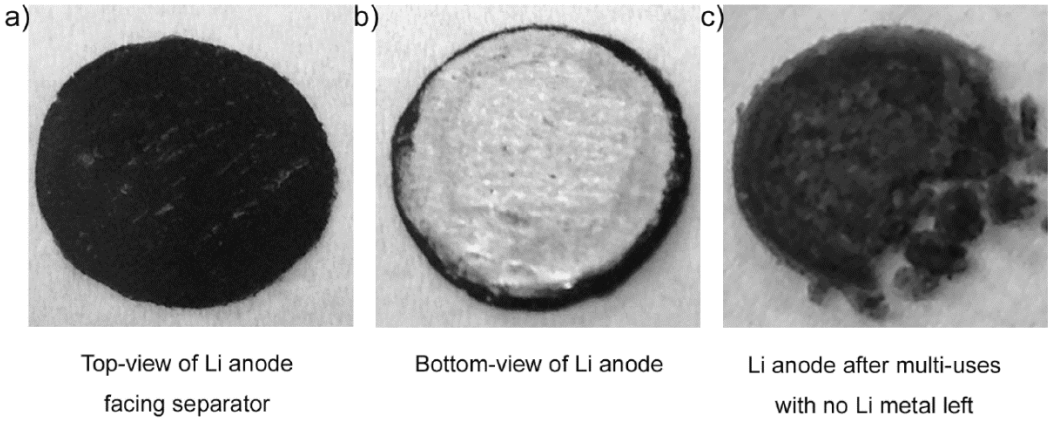

Figure 3.6 Degradation of Li anode in TEGDME electrolyte. a) The side of the Li anode facing the cathode. b) The opposite side. c) Significant decomposition after multiple cycle tests. Reproduced with permission from Ref. [77]. Copyright 2013 NPG.

3.4.2 Reactivity of reduced oxygen species on the Li surfaces

As discussed in the Section 3.2, for most Li-O_2 test cells, the electrolytes are saturated with O_2. The direct contact between Li and O_2 leads to redox reactions that produce reduced oxygen species such as superoxides (e.g., $O_2^{\cdot-}$, **Figure 3.7**).[51,80] Under ideal conditions, the final product of these reactions would be Li_2O. It can serve as an SEI layer to prevent further reactions between Li and O_2, and the amount of reduced oxygen species due to these reactions is negligible. But due to the poor quality of the SEI layer and also due to the dendritic growth of Li, the reactions between Li and O_2 have been found to be continuous during repeated cycling of Li-O_2 test cells.[51,77,80,81] It is therefore important to examine how the parasitic chemistries at the Li anode influence the overall stability of Li-O_2 batteries.

The reactivity of superoxide species toward the electrolytes has been discussed in the previous section. They are oxidative to attack the Li anode and the carbon cathode, basic to extract H from the organic electrolyte molecules and nucleophilic to attack carbonyl groups.[27] It is noted that as the necessary intermediates of ORR at the cathode (see Section 3.3), superoxide species already abound in the system. The additional ones produced at the Li anode are comparably low in quantities. Nevertheless, their influence of promoting the parasitic chemistries at the Li anode is profound. (**Figure 3.7**)

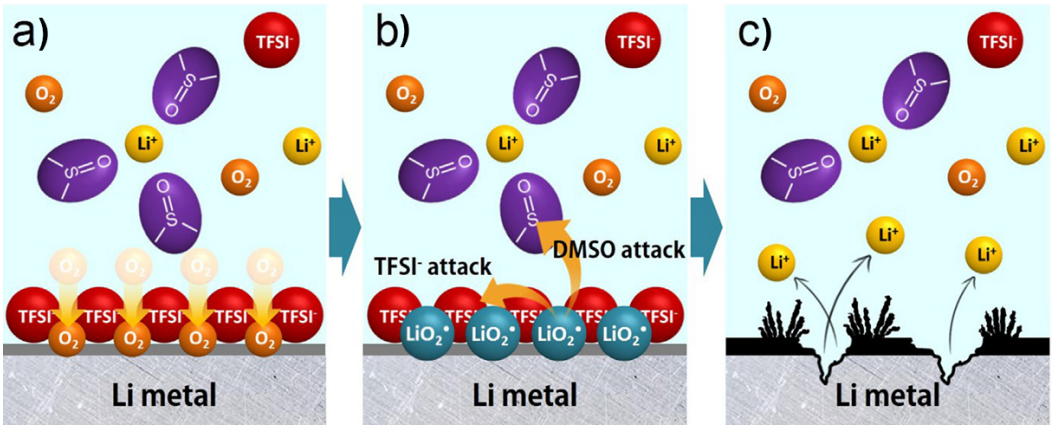

Figure 3.7 The existence of reduced oxygen species on the anode surfaces and their reactivity toward Li anode corrosion. a) Generation of superoxide species on Li surface. b) Superoxide species attack the electrolyte. c) The reaction leads to etching of the Li anode. Reproduced with permission from Ref. [80]. Copyright 2014 Elsevier.

Furthermore, even for thermodynamically more stable products such as Li_2O_2 and Li_2O, their reactivity with the electrolytes should be examined with great care.[14,29] For instance, Li_2O as a stable final product is strongly basic. It can abstract protons even for solvents normally considered aprotic. It has been shown that soaking Li_2O and Li_2O_2 in pure DMSO

solution results in the formation of LiOH and severe degradation of DMSO (**Figure 3.3**).[29,44,82] As a consequence, in the full cell tests, large amount of LiOH was observed on the surface of Li, much more than what can be accounted for by the water impurities in the electrolyte.[82]

3.4.3 Synergy between oxygen and the SEI formation

The spontanous SEI formed in the Ar atomosphere usually contains Li_2CO_3, Li_2O, LiF, RCOOLi, ROLi and some polymeric compounds (**Figure 3.8**). When O_2 is introduced to the system, compositional and morphological changes are often observed. Both positive and negative impacts to the cell stability due to these changes have been reported.[80,83] In the case of DMSO, the increase of Li_2O enhances the formation of LiOH, which lowers the Coulombic efficiency of the Li anode.[80,82] In the case of $N_{1114}TF_2N$ ionic liquid, however, >10% improvement of the anode Coulombic efficiecies was observed in dry oxygen as compared to Ar atomsphere. It was found that O_2 helps reduce the thickness of the SEI layer by up to 67% (**Figure 3.9**).[84] In another example, O_2 was discovered to help regenerate $LiNO_3$ ($LiNO_2+O_2 \rightarrow LiNO_3$), which has been shown to react with Li to form Li_2O as a reasonably stable SEI in DMA.[85] Without O_2, the protection effect fades quickly due to the consumption of $LiNO_3$.[53]

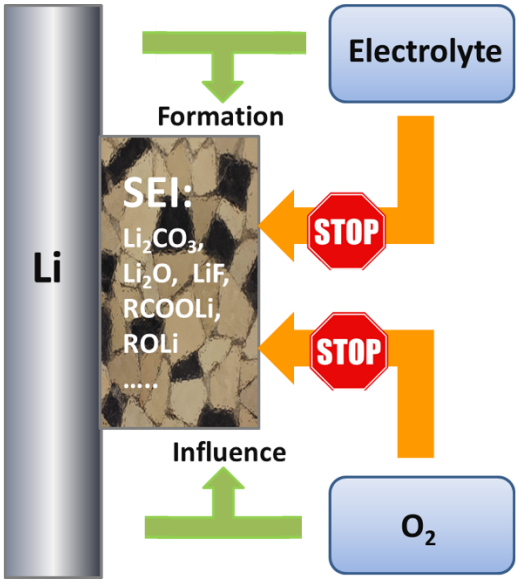

Figure 3.8 Spontaneous formation of SEI layer and its protection effect of Li against electrolyte and oxygen.

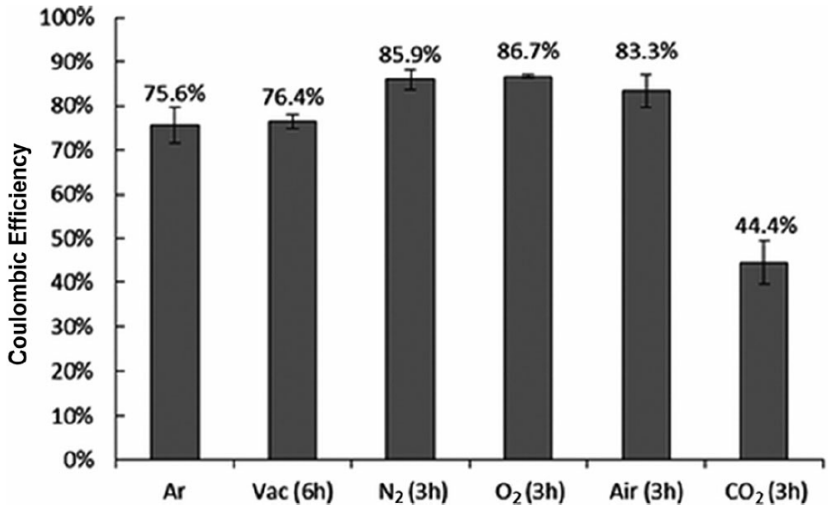

Figure 3.9 Effects of oxygen invasion to the anode. The Coulombic efficiencies are sensitive to the atmosphere in which the SEI is formed. Reproduced with permission from Ref. [84]. Copyright 2013 ACS.

3.4.4 Summary of parasitic chemistries at the Li anode

The utilization of Li as the anode is of great importance to actualizing the full potentials of Li-O_2 battereis as a high energy density energy storage technology. The reactivity of Li with the electrolyte and O_2 is therefore a critical issue that has received underwhelming attention previously.[51,77,80,82,86] We see from the above discussions that the presence of O_2 has a profound impact on the SEI layer, both its formation and the compositional changes. The direct reactions between Li and O_2 genreate reactive oxygen species that may contribute to the degradation of the electrolyte. Additionally, the reductive nature of Li further limits the electrolyte choices. These issues call for a solution that may be met by a stable artificial SEI layer (see Section 3.5).

3.5 Summary and Outlook

Compared to LIBs, Li-O_2 batteries feature one additional component, O_2, which is highly reactive. This addition complicates the possible chemistries considerably, making it difficult to study the parasitic chemistries at the anode, the cathode and within the electrolyte that are inherent to Li-O_2 batteries. But the understanding of these chemistries is critical to the actualization of the promise held by Li-O_2 batteries. While the parasitic cathode degradation and electrolyte decomposition have been reviewed separately previously, their possible synergistic effects are rarely discussed in a systematic fashion previously.

We see from the discussions that O_2 and reactive oxygen species play important roles in promoting various undesired side reactions in nearly all components of a test cell. For the anode, oxygen species react with Li to initiate a number of reactions that contribute to the degradation of the anode. In addition, Li often exhibits reactivity toward the electrolyte, particularly those with resistance against oxidation (e.g., DMA and DMSO). While the formation of spontaneous SEI layer helps protect Li to some extent, the effect is highly phenomological and lacks control. Moving forward, the strategy of forming a stable SEI is expected to address this issue. Solid-state electrolytes that can be grown as ultra-thin, uniform layers can serve as an artificial SEI layer and have received some research attention lately.[87,88] The issues connect to the reactivity of carbon surfaces may be mitigated by coating the cathode with passivation layers. But such an approach also makes it difficult to take advantage of the good ORR activity of carbon, which may increase the discharge overpotentials. To solve the problem, researchers have started looking into the possibility of promoting one-electron reaction pathways by choosing appropriate electrolytes. Additionally, researchers have studied the possibilities of controlling the reaction pathways by altering the carbon surfaces and morphologies.[63,89] Before these approaches can be widely implemented, nevertheless, careful studies must be performed to evaluate how the new reaction pathways impact the stability of various components of the test cells. With regard to the electrolyte, no known compounds are stable enough for the operation of Li-O_2 batteries. It is by far the most challenging problem that requires significant research attention. While the modification of known compounds for better stability without sacrificing their properties in terms of salt solubility and O_2 diffusivity

appears promising, the performance metrics by these derivatives remain subpar. In addition, the increased cost as a result of the modifications must be taken into account for practical applications. Most importantly, we see from the discussions presented here that future studies of Li-O_2 batteries should benefit tremendously by examining the parasitic chemistries systematically.

3.6 References

[1] Girishkumar, G.; McCloskey, B.; Luntz, A. C.; Swanson, S.; Wilcke, W., Lithium-Air Battery: Promise and Challenges. *J. Phys. Chem. Lett.* **2010,** *1*, 2193.

[2] Bruce, P. G.; Freunberger, S. A.; Hardwick, L. J.; Tarascon, J.-M., Li-O_2 and Li-S batteries with high energy storage. *Nat. Mater.* **2012,** *11*, 19.

[3] Abraham, K. M.; Jiang, Z., A Polymer Electrolyte-Based Rechargeable Lithium/Oxygen Battery. *J. Electrochem. Soc.* **1996,** *143*, 1.

[4] Read, J., Ether-Based Electrolytes for the Lithium/Oxygen Organic Electrolyte Battery. *J. Electrochem. Soc.* **2006,** *153*, A96.

[5] Luntz, A. C.; McCloskey, B. D., Nonaqueous Li-Air Batteries: A Status Report. *Chem. Rev.* **2014,** *114*, 11721.

[6] Li, F.; Zhang, T.; Zhou, H., Challenges of non-aqueous Li-O_2 batteries: electrolytes, catalysts, and anodes. *Energy Environ. Sci.* **2013,** *6*, 1125.

[7] Bhatt, M. D.; Geaney, H.; Nolan, M.; O'Dwyer, C., Key scientific challenges in current rechargeable non-aqueous Li-O_2 batteries: experiment and theory. *Phys. Chem. Chem. Phys.* **2014,** *16*, 12093.

[8] Balaish, M.; Kraytsberg, A.; Ein-Eli, Y., A critical review on lithium-air battery electrolytes. *Phys. Chem. Chem. Phys.* **2014,** *16*, 2801.

[9] Chang, Z. w.; Xu, J. j.; Liu, Q. c.; Li, L.; Zhang, X. b., Recent Progress on Stability Enhancement for Cathode in Rechargeable Non‐Aqueous Lithium-Oxygen Battery. *Adv. Energy Mater.* **2015,** *5*, 1500633.

[10] McCloskey, B. D.; Bethune, D. S.; Shelby, R. M.; Mori, T.; Scheffler, R.; Speidel, A.; Sherwood, M.; Luntz, A. C., Limitations in Rechargeability of Li-O_2 Batteries and Possible Origins. *J. Phys. Chem. Lett.* **2012,** *3*, 3043.

[11] Lu, Y.-C.; Gallant, B. M.; Kwabi, D. G.; Harding, J. R.; Mitchell, R. R.; Whittingham, M. S.; Shao-Horn, Y., Lithium-oxygen batteries: bridging mechanistic understanding and battery performance. *Energy Environ. Sci.* **2013,** *6*, 750.

[12] Wang, Z.-L.; Xu, D.; Xu, J.-J.; Zhang, X.-B., Oxygen electrocatalysts in metal-air batteries: from aqueous to nonaqueous electrolytes. *Chem. Soc. Rev.* **2014,** *43*, 7746.

[13] McCloskey, B. D.; Scheffler, R.; Speidel, A.; Girishkumar, G.; Luntz, A. C., On the Mechanism of Nonaqueous Li-O_2 Electrochemistry on C and Its Kinetic Overpotentials: Some Implications for Li-Air Batteries. *J. Phys. Chem. C* **2012,** *116*, 23897.

[14] McCloskey, B. D.; Valery, A.; Luntz, A. C.; Gowda, S. R.; Wallraff, G. M.; Garcia, J. M.; Mori, T.; Krupp, L. E., Combining Accurate O_2 and Li_2O_2 Assays to Separate Discharge and Charge Stability Limitations in Nonaqueous Li-O_2 Batteries. *J. Phys. Chem. Lett.* **2013,** *4*, 2989.

[15] McCloskey, B. D.; Speidel, A.; Scheffler, R.; Miller, D. C.; Viswanathan, V.; Hummelshøj, J. S.; Nørskov, J. K.; Luntz, A. C., Twin Problems of Interfacial Carbonate Formation in Nonaqueous Li-O_2 Batteries. *J. Phys. Chem. Lett.* **2012,** *3*, 997.

[16] Ottakam Thotiyl, M. M.; Freunberger, S. A.; Peng, Z.; Bruce, P. G., The Carbon Electrode in Nonaqueous Li-O_2 Cells. *J. Am. Chem. Soc.* **2013,** *135*, 494.

[17] McCloskey, B. D.; Bethune, D. S.; Shelby, R. M.; Girishkumar, G.; Luntz, A. C., Solvents' Critical Role in Nonaqueous Lithium-Oxygen Battery Electrochemistry. *J. Phys. Chem. Lett.* **2011,** *2*, 1161.
[18] Peng, Z.; Freunberger, S. A.; Chen, Y.; Bruce, P. G., A Reversible and Higher-Rate Li-O_2 Battery. *Science* **2012,** *337*, 563.
[19] Adams, B. D.; Black, R.; Williams, Z.; Fernandes, R.; Cuisinier, M.; Berg, E. J.; Novak, P.; Murphy, G. K.; Nazar, L. F., Towards a Stable Organic Electrolyte for the Lithium Oxygen Battery. *Adv. Energy Mater.* **2015,** *5*, 1400867.
[20] Xu, W.; Wang, J.; Ding, F.; Chen, X.; Nasybulin, E.; Zhang, Y.; Zhang, J.-G., Lithium metal anodes for rechargeable batteries. *Energy Environ. Sci.* **2014,** *7*, 513.
[21] Obrovac, M. N.; Chevrier, V. L., Alloy Negative Electrodes for Li-Ion Batteries. *Chem. Rev.* **2014,** *114*, 11444.
[22] Gittleson, F. S.; Sekol, R. C.; Doubek, G.; Linardi, M.; Taylor, A. D., Catalyst and electrolyte synergy in Li-O_2 batteries. *Phys. Chem. Chem. Phys.* **2014,** *16*, 3230.
[23] Black, R.; Lee, J. H.; Adams, B.; Mims, C. A.; Nazar, L. F., The Role of Catalysts and Peroxide Oxidation in Lithium-Oxygen Batteries. *Angew. Chem. Int. Ed.* **2013,** *52*, 392.
[24] McCloskey, B. D.; Scheffler, R.; Speidel, A.; Bethune, D. S.; Shelby, R. M.; Luntz, A. C., On the Efficacy of Electrocatalysis in Nonaqueous Li-O_2 Batteries. *J. Am. Chem. Soc.* **2011,** *133*, 18038.
[25] Calvo, E. J.; Mozhzhukhina, N., A rotating ring disk electrode study of the oxygen reduction reaction in lithium containing non aqueous electrolyte. *Electrochem. Commun.* **2013,** *31*, 56.
[26] Yang, J.; Zhai, D.; Wang, H.-H.; Lau, K. C.; Schlueter, J. A.; Du, P.; Myers, D. J.; Sun, Y.-K.; Curtiss, L. A.; Amine, K., Evidence for lithium superoxide-like species in the discharge product of a Li-O_2 battery. *Phys. Chem. Chem. Phys.* **2013,** *15*, 3764.
[27] Black, R.; Oh, S. H.; Lee, J.-H.; Yim, T.; Adams, B.; Nazar, L. F., Screening for Superoxide Reactivity in Li-O_2 Batteries: Effect on Li_2O_2/LiOH Crystallization. *J. Am. Chem. Soc.* **2012,** *134*, 2902.
[28] Du, P.; Lu, J.; Lau, K. C.; Luo, X.; Bareno, J.; Zhang, X.; Ren, Y.; Zhang, Z.; Curtiss, L. A.; Sun, Y.-K.; Amine, K., Compatibility of lithium salts with solvent of the non-aqueous electrolyte in Li-O_2 batteries. *Phys. Chem. Chem. Phys.* **2013,** *15*, 5572.
[29] Kwabi, D. G.; Batcho, T. P.; Amanchukwu, C. V.; Ortiz-Vitoriano, N.; Hammond, P.; Thompson, C. V.; Shao-Horn, Y., Chemical Instability of Dimethyl Sulfoxide in Lithium-Air Batteries. *J. Phys. Chem. Lett.* **2014,** *5*, 2850.
[30] Xu, W.; Xu, K.; Viswanathan, V. V.; Towne, S. A.; Hardy, J. S.; Xiao, J.; Nie, Z.; Hu, D.; Wang, D.; Zhang, J.-G., Reaction mechanisms for the limited reversibility of Li-O_2 chemistry in organic carbonate electrolytes. *J. Power Sources* **2011,** *196*, 9631.
[31] Sharon, D.; Afri, M.; Noked, M.; Garsuch, A.; Frimer, A. A.; Aurbach, D., Oxidation of Dimethyl Sulfoxide Solutions by Electrochemical Reduction of Oxygen. *J. Phys. Chem. Lett.* **2013,** *4*, 3115.
[32] Xie, J.; Dong, Q.; Madden, I.; Yao, X.; Cheng, Q.; Dornath, P.; Fan, W.; Wang, D., Achieving Low Overpotential Li-O_2 Battery Operations by Li_2O_2 Decomposition through One-Electron Processes. *Nano Lett.* **2015,** *15*, 8371.

[33] Johnson, L.; Li, C.; Liu, Z.; Chen, Y.; Freunberger, S. A.; Ashok, P. C.; Praveen, B. B.; Dholakia, K.; Tarascon, J.-M.; Bruce, P. G., The role of LiO_2 solubility in O_2 reduction in aprotic solvents and its consequences for Li-O2 batteries. *Nat. Chem.* **2014,** *6*, 1091.
[34] Freunberger, S. A.; Chen, Y.; Peng, Z.; Griffin, J. M.; Hardwick, L. J.; Bardé, F.; Novák, P.; Bruce, P. G., Reactions in the Rechargeable Lithium-O_2 Battery with Alkyl Carbonate Electrolytes. *J. Am. Chem. Soc.* **2011,** *133*, 8040.
[35] Bryantsev, V. S.; Giordani, V.; Walker, W.; Blanco, M.; Zecevic, S.; Sasaki, K.; Uddin, J.; Addison, D.; Chase, G. V., Predicting Solvent Stability in Aprotic Electrolyte Li-Air Batteries: Nucleophilic Substitution by the Superoxide Anion Radical ($O_2^{\bullet-}$). *J. Phys. Chem. A* **2011,** *115*, 12399.
[36] Bryantsev, V. S.; Uddin, J.; Giordani, V.; Walker, W.; Addison, D.; Chase, G. V., The Identification of Stable Solvents for Nonaqueous Rechargeable Li-Air Batteries. *J. Electrochem. Soc.* **2013,** *160*, A160.
[37] Walker, W.; Giordani, V.; Uddin, J.; Bryantsev, V. S.; Chase, G. V.; Addison, D., A Rechargeable Li–O_2 Battery Using a Lithium Nitrate/N,N-Dimethylacetamide Electrolyte. *J. Am. Chem. Soc.* **2013,** *135*, 2076.
[38] Chen, Y.; Freunberger, S. A.; Peng, Z.; Bardé, F.; Bruce, P. G., Li-O_2 Battery with a Dimethylformamide Electrolyte. *J. Am. Chem. Soc.* **2012,** *134*, 7952.
[39] Sharon, D.; Hirsberg, D.; Afri, M.; Garsuch, A.; Frimer, A. A.; Aurbach, D., Reactivity of Amide Based Solutions in Lithium-Oxygen Cells. *J. Phys. Chem. C* **2014,** *118*, 15207.
[40] Jung, H.-G.; Hassoun, J.; Park, J.-B.; Sun, Y.-K.; Scrosati, B., An improved high-performance lithium-air battery. *Nat. Chem.* **2012,** *4*, 579.
[41] Bryantsev, V. S.; Faglioni, F., Predicting Autoxidation Stability of Ether- and Amide-Based Electrolyte Solvents for Li-Air Batteries. *J. Phys. Chem. A* **2012,** *116*, 7128.
[42] Harding, J. R.; Amanchukwu, C. V.; Hammond, P. T.; Shao-Horn, Y., Instability of Poly(ethylene oxide) upon Oxidation in Lithium-Air Batteries. *J. Phys. Chem. C* **2015,** *119*, 6947.
[43] Freunberger, S. A.; Chen, Y.; Drewett, N. E.; Hardwick, L. J.; Bardé, F.; Bruce, P. G., The Lithium–Oxygen Battery with Ether-Based Electrolytes. *Angew. Chem. Int. Ed.* **2011,** *50*, 8609.
[44] Khetan, A.; Pitsch, H.; Viswanathan, V., Solvent Degradation in Nonaqueous Li-O_2 Batteries: Oxidative Stability versus H-Abstraction. *J. Phys. Chem. Lett.* **2014,** *5*, 2419.
[45] Mozhzhukhina, N.; Méndez De Leo, L. P.; Calvo, E. J., Infrared Spectroscopy Studies on Stability of Dimethyl Sulfoxide for Application in a Li-Air Battery. *J. Phys. Chem. C* **2013,** *117*, 18375.
[46] Piana, M.; Wandt, J.; Meini, S.; Buchberger, I.; Tsiouvaras, N.; Gasteiger, H. A., Stability of a Pyrrolidinium-Based Ionic Liquid in Li-O_2 Cells. *J. Electrochem. Soc.* **2014,** *161*, A1992.
[47] Schwenke, K. U.; Herranz, J.; Gasteiger, H. A.; Piana, M., Reactivity of the Ionic Liquid $Pyr_{14}TFSI$ with Superoxide Radicals Generated from KO_2 or by Contact of O_2 with $Li_7Ti_5O_{12}$. *J. Electrochem. Soc.* **2015,** *162*, A905.

[48] Laoire, C. O.; Mukerjee, S.; Abraham, K. M.; Plichta, E. J.; Hendrickson, M. A., Influence of Nonaqueous Solvents on the Electrochemistry of Oxygen in the Rechargeable Lithium-Air Battery. *J. Phys. Chem. C* **2010,** *114*, 9178.
[49] Aetukuri, N. B.; McCloskey, B. D.; García, J. M.; Krupp, L. E.; Viswanathan, V.; Luntz, A. C., Solvating additives drive solution-mediated electrochemistry and enhance toroid growth in non-aqueous Li-O_2 batteries. *Nat. Chem.* **2015,** *7*, 50.
[50] García, J. M.; Horn, H. W.; Rice, J. E., Dominant Decomposition Pathways for Ethereal Solvents in Li-O_2 Batteries. *J. Phys. Chem. Lett.* **2015,** *6*, 1795.
[51] Assary, R. S.; Lu, J.; Du, P.; Luo, X.; Zhang, X.; Ren, Y.; Curtiss, L. A.; Amine, K., The Effect of Oxygen Crossover on the Anode of a Li-O_2 Battery using an Ether-Based Solvent: Insights from Experimental and Computational Studies. *ChemSusChem* **2013,** *6*, 51.
[52] Cheng, X. B.; Zhang, R.; Zhao, C. Z.; Wei, F.; Zhang, J. G.; Zhang, Q., A Review of Solid Electrolyte Interphases on Lithium Metal Anode. *Advanced Science* **2016,** *3*, 1500213.
[53] Uddin, J.; Bryantsev, V. S.; Giordani, V.; Walker, W.; Chase, G. V.; Addison, D., Lithium Nitrate As Regenerable SEI Stabilizing Agent for Rechargeable Li/O_2 Batteries. *J. Phys. Chem. Lett.* **2013,** *4*, 3760.
[54] Shao, Y.; Ding, F.; Xiao, J.; Zhang, J.; Xu, W.; Park, S.; Zhang, J. G.; Wang, Y.; Liu, J., Making Li-Air Batteries Rechargeable: Material Challenges. *Adv. Funct. Mater.* **2013,** *23*, 987.
[55] Lu, J.; Li, L.; Park, J.-B.; Sun, Y.-K.; Wu, F.; Amine, K., Aprotic and Aqueous Li-O_2 Batteries. *Chem. Rev.* **2014,** *114*, 5611.
[56] Wang, J.; Li, Y.; Sun, X., Challenges and opportunities of nanostructured materials for aprotic rechargeable lithium-air batteries. *Nano Energy* **2013,** *2*, 443.
[57] Schroeder, M. A.; Pearse, A. J.; Kozen, A. C.; Chen, X.; Gregorczyk, K.; Han, X.; Cao, A.; Hu, L.; Lee, S. B.; Rubloff, G. W.; Noked, M., Investigation of the Cathode-Catalyst-Electrolyte Interface in Aprotic Li-O_2 Batteries. *Chem. Mater.* **2015,** *27*, 5305.
[58] Khetan, A.; Luntz, A.; Viswanathan, V., Trade-Offs in Capacity and Rechargeability in Nonaqueous Li-O_2 Batteries: Solution-Driven Growth versus Nucleophilic Stability. *J. Phys. Chem. Lett.* **2015,** *6*, 1254.
[59] Burke, C. M.; Pande, V.; Khetan, A.; Viswanathan, V.; McCloskey, B. D., Enhancing electrochemical intermediate solvation through electrolyte anion selection to increase nonaqueous Li-O_2 battery capacity. *Proceedings of the National Academy of Sciences* **2015,** *112*, 9293.
[60] McCloskey, B. D.; Burke, C. M.; Nichols, J. E.; Renfrew, S. E., Mechanistic insights for the development of Li-O_2 battery materials: addressing Li_2O_2 conductivity limitations and electrolyte and cathode instabilities. *Chem. Commun.* **2015,** *51*, 12701.
[61] Meini, S.; Solchenbach, S.; Piana, M.; Gasteiger, H. A., The Role of Electrolyte Solvent Stability and Electrolyte Impurities in the Electrooxidation of Li_2O_2 in Li-O_2 Batteries. *J. Electrochem. Soc.* **2014,** *161*, A1306.
[62] Li, F.; Wu, S.; Li, D.; Zhang, T.; He, P.; Yamada, A.; Zhou, H., The water catalysis at oxygen cathodes of lithium-oxygen cells. *Nat. Commun.* **2015,** *6*, 7843.

[63] Liu, T.; Leskes, M.; Yu, W.; Moore, A. J.; Zhou, L.; Bayley, P. M.; Kim, G.; Grey, C. P., Cycling Li-O_2 batteries via LiOH formation and decomposition. *Science* **2015,** *350*, 530.
[64] Shao, Y.; Park, S.; Xiao, J.; Zhang, J.-G.; Wang, Y.; Liu, J., Electrocatalysts for Nonaqueous Lithium-Air Batteries: Status, Challenges, and Perspective. *ACS Catal.* **2012,** *2*, 844.
[65] Harding, J. R.; Lu, Y.-C.; Tsukada, Y.; Shao-Horn, Y., Evidence of catalyzed oxidation of Li_2O_2 for rechargeable Li-air battery applications. *Phys. Chem. Chem. Phys.* **2012,** *14*, 10540.
[66] Ma, S.; Wu, Y.; Wang, J.; Zhang, Y.; Zhang, Y.; Yan, X.; Wei, Y.; Liu, P.; Wang, J.; Jiang, K.; Fan, S.; Xu, Y.; Peng, Z., Reversibility of Noble Metal-Catalyzed Aprotic Li-O_2 Batteries. *Nano Lett.* **2015,** *15*, 8084.
[67] Kang, S. J.; Mori, T.; Narizuka, S.; Wilcke, W.; Kim, H.-C., Deactivation of carbon electrode for elimination of carbon dioxide evolution from rechargeable lithium-oxygen cells. *Nat. Commun.* **2014,** *5*, 3937.
[68] Lu, J.; Lei, Y.; Lau, K. C.; Luo, X.; Du, P.; Wen, J.; Assary, R. S.; Das, U.; Miller, D. J.; Elam, J. W.; Albishri, H. M.; El-Hady, D. A.; Sun, Y.-K.; Curtiss, L. A.; Amine, K., A Nanostructured Cathode Architecture for Low Charge Overpotential in Lithium-Oxygen Batteries. *Nat. Commun.* **2013,** *4*, 2383.
[69] Xie, J.; Yao, X.; Cheng, Q.; Madden, I. P.; Dornath, P.; Chang, C. C.; Fan, W.; Wang, D., Three Dimensionally Ordered Mesoporous Carbon as a Stable, High-Performance Li–O_2 Battery Cathode. *Angew. Chem. Int. Ed.* **2015,** *54*, 4299.
[70] Xie, J.; Yao, X.; Madden, I. P.; Jiang, D.-E.; Chou, L.-Y.; Tsung, C.-K.; Wang, D., Selective Deposition of Ru Nanoparticles on $TiSi_2$ Nanonet and Its Utilization for Li_2O_2 Formation and Decomposition. *J. Am. Chem. Soc.* **2014,** *136*, 8903.
[71] Yao, X.; Cheng, Q.; Xie, J.; Dong, Q.; Wang, D., Functionalizing Titanium Disilicide Nanonets with Cobalt Oxide and Palladium for Stable Li Oxygen Battery Operations. *ACS Appl. Mater. Interfaces* **2015,** *7*, 21948.
[72] Ottakam Thotiyl, M. M.; Freunberger, S. A.; Peng, Z.; Chen, Y.; Liu, Z.; Bruce, P. G., A stable cathode for the aprotic Li-O_2 battery. *Nat. Mater.* **2013,** *12*, 1050.
[73] Etacheri, V.; Marom, R.; Elazari, R.; Salitra, G.; Aurbach, D., Challenges in the development of advanced Li-ion batteries: a review. *Energy Environ. Sci.* **2011,** *4*, 3243.
[74] Hassoun, J.; Jung, H.-G.; Lee, D.-J.; Park, J.-B.; Amine, K.; Sun, Y.-K.; Scrosati, B., A Metal-Free, Lithium-Ion Oxygen Battery: A Step Forward to Safety in Lithium-Air Batteries. *Nano Lett.* **2012,** *12*, 5775.
[75] Guo, Z.; Dong, X.; Wang, Y.; Xia, Y., A lithium air battery with a lithiated Al-carbon anode. *Chem. Commun.* **2015,** *51*, 676.
[76] Elia, G. A.; Bresser, D.; Reiter, J.; Oberhumer, P.; Sun, Y.-K.; Scrosati, B.; Passerini, S.; Hassoun, J., Interphase Evolution of a Lithium-Ion/Oxygen Battery. *ACS Appl. Mater. Interfaces* **2015,** *7*, 22638.
[77] Shui, J.-L.; Okasinski, J. S.; Kenesei, P.; Dobbs, H. A.; Zhao, D.; Almer, J. D.; Liu, D.-J., Reversibility of anodic lithium in rechargeable lithium-oxygen batteries. *Nat. Commun.* **2013,** *4*, 2255.

[78] Younesi, R.; Hahlin, M.; Roberts, M.; Edström, K., The SEI layer formed on lithium metal in the presence of oxygen: A seldom considered component in the development of the Li-O_2 battery. *J. Power Sources* **2013,** *225*, 40.
[79] Park, M. S.; Ma, S. B.; Lee, D. J.; Im, D.; Doo, S.-G.; Yamamoto, O., A Highly Reversible Lithium Metal Anode. *Sci. Rep.* **2014,** *4*, 3815.
[80] Lee, H.; Lee, D. J.; Lee, J.-N.; Song, J.; Lee, Y.; Ryou, M.-H.; Park, J.-K.; Lee, Y. M., Chemical aspect of oxygen dissolved in a dimethyl sulfoxide-based electrolyte on lithium metal. *Electrochim. Acta* **2014,** *123*, 419.
[81] Assary, R. S.; Lu, J.; Luo, X.; Zhang, X.; Ren, Y.; Wu, H.; Albishri, H. M.; El‐Hady, D. A.; Al‐Bogami, A. S.; Curtiss, L. A.; Amine, K., Molecular-Level Insights into the Reactivity of Siloxane‐Based Electrolytes at a Lithium-Metal Anode. *ChemPhysChem* **2014,** *15*, 2077.
[82] Marinaro, M.; Balasubramanian, P.; Gucciardi, E.; Theil, S.; Jörissen, L.; Wohlfahrt‐Mehrens, M., Importance of Reaction Kinetics and Oxygen Crossover in aprotic Li–O_2 Batteries Based on a Dimethyl Sulfoxide Electrolyte. *ChemSusChem* **2015,** *8*, 3139.
[83] Togasaki, N.; Momma, T.; Osaka, T., Role of the solid electrolyte interphase on a Li metal anode in a dimethylsulfoxide-based electrolyte for a lithium-oxygen battery. *J. Power Sources* **2015,** *294*, 588.
[84] Stark, J. K.; Ding, Y.; Kohl, P. A., Role of Dissolved Gas in Ionic Liquid Electrolytes for Secondary Lithium Metal Batteries. *J. Phys. Chem. C* **2013,** *117*, 4980.
[85] Giordani, V.; Walker, W.; Bryantsev, V. S.; Uddin, J.; Chase, G. V.; Addison, D., Synergistic Effect of Oxygen and $LiNO_3$ on the Interfacial Stability of Lithium Metal in a Li/O_2 Battery. *J. Electrochem. Soc.* **2013,** *160*, A1544.
[86] Lee, D. J.; Lee, H.; Kim, Y. J.; Park, J. K.; Kim, H. T., Sustainable Redox Mediation for Lithium–Oxygen Batteries by a Composite Protective Layer on the Lithium-Metal Anode. *Adv. Mater.* **2016,** *28*, 857.
[87] Kozen, A. C.; Lin, C.-F.; Pearse, A. J.; Schroeder, M. A.; Han, X.; Hu, L.; Lee, S.-B.; Rubloff, G. W.; Noked, M., Next-Generation Lithium Metal Anode Engineering via Atomic Layer Deposition. *ACS Nano* **2015,** *9*, 5884.
[88] Visco, S. J.; Nimon, V. Y.; Petrov, A.; Pridatko, K.; Goncharenko, N.; Nimon, E.; De Jonghe, L.; Volfkovich, Y. M.; Bograchev, D. A., Aqueous and nonaqueous lithium-air batteries enabled by water-stable lithium metal electrodes. *J. Solid State Electrochem.* **2014,** *18*, 1443.
[89] Lu, J.; Jung Lee, Y.; Luo, X.; Chun Lau, K.; Asadi, M.; Wang, H.-H.; Brombosz, S.; Wen, J.; Zhai, D.; Chen, Z.; Miller, D. J.; Sub Jeong, Y.; Park, J.-B.; Zak Fang, Z.; Kumar, B.; Salehi-Khojin, A.; Sun, Y.-K.; Curtiss, L. A.; Amine, K., A lithium-oxygen battery based on lithium superoxide. *Nature* **2016,** *529*, 377.

Chapter 4 High Voltage Solar Rechargeable Redox Battery

4.1 Introduction

As the most abundant form of renewable energy on this lone planet, solar energy is diurnal and intermittent. Such a nature creates a critical challenge in its utilization.[1] It is generally agreed upon that converting and storing the energy in chemicals by means such as electrochemical (or photoelectrochemical) reactions hold the key to large-scale, practical implementations of solar energy.[2,3] Toward this direction, a variety of approaches have been proposed and actively pursued.[4] In terms of technology readiness levels, the most direct route would be to connect photovoltaic devices with batteries (e.g., state-of-the-art Li-ion batteries).[5,6] While already implemented in small-scale commercial settings, this method faces critical issues connected to the high cost of both the photovoltaic and the battery modules.[1,7] Alternatively, artificial photosynthesis represents the most cost-effective route if the efficiencies of the processes can be significantly improved.[8,9] Indeed, great efforts have been attracted toward the goal of efficient artificial photosynthesis.[10-12] However, when the release of the stored energy by artificial photosynthesis is taken into account (through methods such as fuel cells or thermal engines), the approach features inherently low round-trip efficiencies, due to the high overpotentials associated with the breaking and formation of chemical bonds.[13] Consider water splitting as an example to further illustrate this point. Even with the most effective catalysts, a minimum overpotential of 295 mV is required to reach a reasonable current density (e.g., at 10

mA/cm^2) for water splitting, corresponding to a storage potential of 1.53 V.[14,15] Conversely, even with the most effective catalysts for hydrogen fuel cells (HFCs), a minimum overpotential of ~450 mV is necessary for the release of the stored energy at a reasonable current density (e.g., at 1.0 A/cm^2).[16] As such, the maximum round-trip efficiency is limited to about 50%.[17] From this perspective, we see that it should be beneficial to combine the advantages offered by batteries in terms of high round-trip efficiencies and the benefits held by direct (photo)electrochemical systems in terms of high energy densities and low costs.[3,18]

It is within this context that researchers have turned attention to solar rechargeable redox batteries.[19] While the idea was originally proposed in 1976, it did not gain attractions until recently.[20-25] Wu and co-workers are among the recent pioneers toward this direction. For instance, they have demonstrated that direct combination of dye-sensitized solar cells (DSSC) with Li-O_2 batteries could effectively increase the round-trip efficiencies of the system.[26] Most recently, they achieved unassisted solar rechargeable flow batteries based on the AQDS (anthraquinone-2,7-disulphonic acid) anolyte and the iodide catholyte.[27] Nevertheless, the discharge cell voltages of their systems are limited (<0.8 V). Li and co-workers, and most recently Jin and co-workers, have separately demonstrated that Si photoelectrodes with buried p-n junctions can be readily utilized for the implementation of solar rechargeable redox flow batteries.[28,29] While high overall solar-to-electricity efficiencies (up to 3.2%) have been obtained, the cell voltages as determined by the redox

pair choices remain low. As far as cell voltages are concerned, Mendes and co-workers have shown that connecting DSSC with a photoelectrode (CdS) in series enables a cell voltage of 1.2 V based on the VO_2^+/VO^{2+} and V^{3+}/V^{2+} redox couples.[30] The poor stability of CdS in the aqueous system, nonetheless, prevented the measurement of meaningful discharge performance. Most recently, the same authors have applied a stable hematite photoanode to directly charge an aqueous alkaline AQDS-ferrocyanide redox flow battery with cell potential of 0.74 V.[31] Notwithstanding, the low current density (< 0.5 mA/cm^2) of hematite and the resulting low solar-to-chemical efficiency (< 0.1%) leave much to desire. To date, low cell voltage remains a critical issue for solar rechargeable redox flow batteries.[32]

By its very nature, the cell voltage of a solar rechargeable redox battery is limited by two factors, the achievable photovoltage of the photoelectrodes and the electrochemical potential differences between the redox pairs. Learning from parallel researches on photoelectrochemistry, we understand that it is exceedingly difficult to obtain a high photovoltage on a single light absorber.[33] This is because photoelectrodes that are likely to yield photovoltages >1.0 V would be wide bandgap semiconductors which only absorb in the short wavelength region of the solar spectrum, corresponding to low overall solar-to-electricity efficiencies.[34] As has been demonstrated in research on solar water splitting, possible solutions to this issue are to use multiple photoelectrodes.[35] Here we show that the idea worked well for solar rechargeable redox batteries. The photoanode in the system in

our system was based on Ta_3N_5 nanotubes, and the photocathode was based on GaN nanowires on Si with buried p-n junctions. Together, the two photoelectrodes enabled an overall photovoltage of 1.5 V, the highest for similar systems in the literature, to the best of our knowledge. For the redox systems, we took advantage of the latest breakthroughs reported by Gordon and co-workers, which features hydroxy-substituted anthraquinone and ferrocyanide with an equilibrium cell voltage of 1.2 V.[36] An overall 3.0% solar-to-chemical energy conversion efficiency was measured. Moreover, the inherent stability of the nitride systems in the presence of the redox pairs permitted us to measure stable performance up to 5 hr under photoelectrochemical operation conditions.[37,38] Importantly, a discharge cell voltage of up to 1 V was measured.

4.2 Experimental Details

4.2.1 Ta_3N_5 Photoanode Preparation

The Ta_3N_5 nanotubes (NTs) were synthesized through electrochemical anodization, using Ta foil (0.127 mm thick, Alfa Aesar) as the precursor.[39] The Ta foil was first cut into a piece (0.5 cm × 2 cm), of which one side was roughened with sandpaper for 10 min. Subsequently, the polished Ta foil was cleaned by ultrasonication in acetone, methanol, iso-propanol, and deionized (DI) water, respectively, then dried by flowing air. The anodization electrolyte was prepared by mixing sulfuric acid (38 mL, 95-98%, Sigma-Aldrich), hydrofluoric acid (0.4 mL, 48%, Sigma-Aldrich), and DI water (1.6 mL). By anodizing the Ta foil with Pt gauze as the counter electrode under 60 V direct current bias

for 10 min without stirring, the tantalum oxide NTs were obtained and the residual electrolyte on the sample surface were removed by ethanol and DI water. The conversion of as-prepared tantalum oxide NTs into Ta_3N_5 nanotubes was realized by calcining in a quartz-tube furnace (Lindberg/Blue M) at 1000 ^oC raised from room temperature at 10 ^oC/min rate for 2 hr under anhydrous NH_3 atmosphere at 300 torr with 75 sccm (standard cubic centimeter per minute) flowing rate.

4.2.2 TiO_2/GaN/Si photocathode preparation

The n^+-p Si was prepared according to the previously reported procedures.[40] The phosphorus and boron dopant precursors were spin coated on the front and back sides of p-doped Si (100) wafers (WRS Materials, thickness: 256─306 μm; resistivity: 1─10 Ω·cm), respectively. Then the Si wafers were put into a tube furnace and annealed at 900 ^oC for 4 hr under a N_2 atmosphere. The n^+ emitter layer and p^+ electron back reflection layer on the front side and back side of the Si wafer formed during the thermal diffusion process, respectively. The n^+-p Si, of which the surface oxide was first removed by buffered hydrofluoric acid, was further used as substrate for growing GaN nanowire arrays by radio frequency plasma-assisted molecular beam epitaxy (MBE). The following is the growth conditions of n-type GaN nanowire arrays: a substrate temperature of 750 ^oC, a nitrogen flow rate of 1.0 sccm, forward plasma power of 350 W, and Ga flux in the range of 4.5×10^{-8} to 8×10^{-8} Torr. The nanowire arrays were doped as n-type using Ge.

Thin passivation layer of TiO_2 on GaN/Si was constructed by ALD (Savannah 100, Cambridge Nanotech), and the whole process mainly followed the parameters of our previous reports.[41] $Ti(i\text{-}PrO)_4$ (operating temperature: 75 ^oC) and H_2O (operating temperature: room temperature) were applied as the Ti and O resources, respectively, and the temperature for growth was maintained at 275 ^oC with a constant flow of N_2 at 20 sccm (chamber base pressure ~500 mTorr). The pulse and purge time for $Ti(i\text{-}PrO)_4$ and H_2O was 0.1s & 5s, and 0.01s & 10s, respectively. The final thickness of TiO_2 passivation layer was controlled to ca. 25 nm after a growth of 750 cycles.

4.2.3 Photoelectrochemical measurements

The PEC performances were characterized by potentiostat (Modulab XM, coupled with Modulab XM ECS software) in a three-electrode system. An AM 1.5 solar simulator (Solarlight Model 16S-300-M Air Mass Solar Simulator) was used as the light source, and the illumination intensity during the PEC measurement was adjusted to 100 mW/cm^2 except the investigation of the influence of the illumination intensities on the photocurrent densities. The semiconductor photoelectrodes were used as the working electrode with Hg/HgO electrode soaked in 1 M NaOH solution as the reference and Pt wire as the counter electrode. The electrode potentials have been converted to NHE scale using $E_{NHE} = E_{Hg/HgO} + 0.13$ V. In a typical J-V experiment, the voltage was swept linearly (Ta_3N_5: from negative to positive; TiO_2/GaN/Si: from positive to negative) at a rate of 20 mV/s, and the whole

process was stirred with constant rate (1100 rpm) except the characterization of the influence of the stirring rates on the photocurrent densities.

The overall solar-to-chemical energy conversion efficiency (η_{stc}) can be calculated according to (assuming a Faradic efficiency of 100% for both reactions):[35]

$$\eta_{stc} = [J_{op}(mA/cm^{-2}) \times 1.2\ (V)] / [2 \times P_{in}(mW/cm^{-2})] \qquad (4.1)$$

In the above equation, J_{op} stands for the maximum operating current density determined by the intersection of the individually tested J-V data of the photoelectrodes. 1.2 V is the cell equilibrium potential determined by the reversible potential of the redox couples and P_{in} stands for the incident illumination power density (100 mW/cm^2). For the η_{stc} calculation, P_{in} was multiplied by two in this system since the photoelectrodes were illuminated in parallel by two solar simulators in the solar rechargeable redox battery measurement.

4.2.4 Electrochemical measurements

The electrolytes used in the electrochemical cell were consisted of 0.1 M 2,6-DHAQ (90% purity, purchased from AK Scientific Inc.) and 0.4 M $K_4Fe(CN)_6$ ($K_4Fe(CN)_6 \cdot 3H_2O$, 98.5-102.0%, purchased from Sigma Aldrich), both dissolved in KOH solution (pH 12 or 14) as required. A customized glass two-chamber cell (see **Figure 4.1** for detailed structure) was used as the redox battery study platform. A sheet of pretreated Nafion 212 film (purchased from Fuel Cell Store) was used as the ion-selective membrane to separate the electrolytes into two separate chambers. The pretreatment of the Nafion 212 film was

performed by soaking in 80 °C deionized water for 20 min followed by soaking in 5% H_2O_2 for 30 min, and then thoroughly washed with deionized water. A sheet of Sigracet ® SGL 39AA porous carbon paper (1 cm^2, purchased from Ion Power) was applied as both electrodes and the carbon paper was pretreated by calcining at 400 °C for 24 hr in air before use. Both the pretreatments of membrane and electrode are performed according to the previous report.[36] Electrochemical characterizations of 2,6-DHAQ/$K_4Fe(CN)_6$ battery performance were carried out on an electrochemical station (Biologic, VMP3) under uninterrupted vigorous stirring (~1100 rpm). The cell was carefully sealed and both electrolytes were purged with ultra-high purity N_2 during the whole process to avoid the oxidation of the reduction product of 2,6-DHAQ.

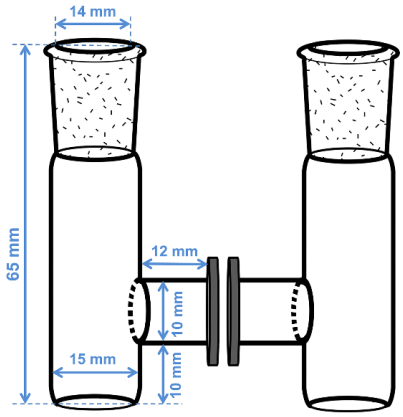

Figure 4.1 Two-chamber cell structure: the electrolyte volume applied in each chamber is 3 mL.

4.2.5 Solar rechargeable redox battery measurements

The cell system of solar rechargeable redox battery is similar with the above redox battery cell, and the only difference is that Ta_3N_5 photoanode and TiO_2/GaN/Si photocathode were added into the catholyte and anolyte chamber, respectively. During photocharge process, the Ta_3N_5 photoanode and the TiO_2/GaN/Si photocathode were connected to a potentiostat (Modulab XM) through external wires and illuminated with solar simulators (100 mW/cm^2, AM 1.5) in parallel. The simulated solar illumination was turned off when the photocurrent density decreased to around zero. Then, the two carbon paper electrodes were connected to the same potentiostat instead and discharged galvanostatically at 0.5 mA/cm^2 current density and the discharge process was terminated when the voltage decreased to 0.6 V.

4.2.6 Material characterizations

The scanning electron microscope (SEM) was used to characterize the morphologis of Ta_3N_5 (SEM, JSM6340F) and GaN/Si (SEM, FEI Inspect F-50). UV-vis absorption spectrums were recorded by a spectrophotometer (Ocean Optics Inc. ISS-UV/VIS). Proton nuclear magnetic resonance (^{1}H NMR) spectra was performed using a Variant (600 MHz) NMR spectrometer. Deuterated oxide (D_2O, 99.9%, purchased from Cambridge Isotope Labs.) was used as the solvent. All NMR chemical shifts were reported in ppm relative to residual solvents.

4.3 Results and Discussions

4.3.1 Design of the photorechargeable high voltage redox battery system

Our design is schematically illustrated in **Figure 4.2**. The electrolytes consist of $K_4[Fe(CN)_6]$ solution in the positive compartment and 2,6-dihydroxyanthraquinone (2,6-DHAQ) solution in the negative compartment. The electrodes consist of Ta_3N_5 photoanode, GaN/Si photocathode and two carbon paper electrodes. Upon illumination, the battery is directly charged by short-circuiting two photoelectrodes as $K_4[Fe(CN)_6]$ is oxidized on Ta_3N_5 photoanode and 2,6-DHAQ is reduced on GaN/Si photocathode. Afterwards, the discharge takes place on a separate set of carbon paper electrodes.

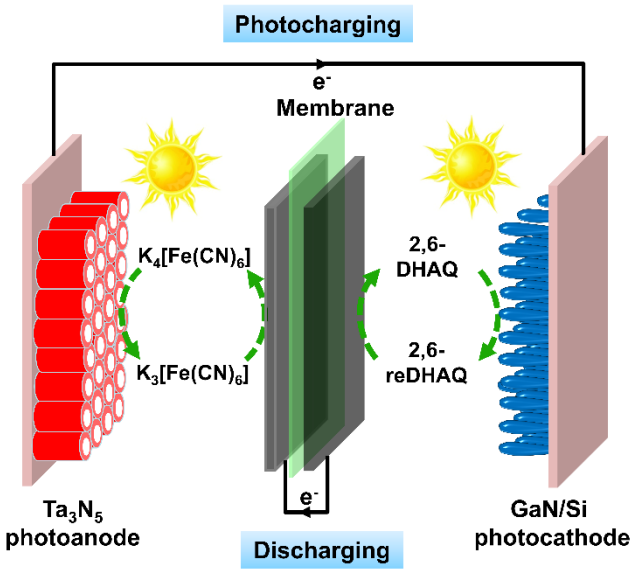

Figure 4.2 Schematic illustration of our design.

The choice of Ta_3N_5 nanotubes (see **Figure 4.3a** for the morphology) as the photoanode is inspired by recent successes in measuring high photocurrents on this material for solar water oxidation reactions.[42] We are also motivated to use Ta_3N_5 for the oxidation of

$Fe(CN)_6^{4-}$ by our recent observations that remarkable stability can be obtained on Ta_3N_5 in the presence of $Fe(CN)_6^{4-}$.[39] Our choice of photocathode consists of a planar n^+-p Si substrate and n-GaN nanowire arrays along the axial direction (GaN/n^+-p Si; morphology shown in **Figure 4.3b**). As has been demonstrated by Mi and co-workers, the light absorption and charge separation by the GaN/n^+-p Si system take place within the p-n junction in Si. In principle, the light absorption of the photoanode (Ta_3N_5) and the photocathode (Si) are complementary (λ <1100 nm for Si and λ <590 nm for Ta_3N_5), opening up opportunities to set up the photoelectrodes in a tandem configuration. Of the two photoelectrodes, Ta_3N_5 is expected to produce a photovoltage up to 0.9 V at pH 14. The value is obtained by comparing the light open circuit voltage of Ta_3N_5 (ca. -0.4 V vs. NHE) and the redox potential of $Fe(CN)_6^{3-/4-}$ (+0.5 V NHE; **Figure 4.5**).[39] Mi and co-workers have previously measured the performance of GaN/n^+-p Si photocathode and obtained a reproducible photovoltage up to 0.6 V.[40] When combined, the overall photovoltage of the system would be sufficient to directly charge the 2,6-DHAQ/$Fe(CN)_6^{4-}$ redox systems (cell voltage 1.2 V), without the need for external bias.

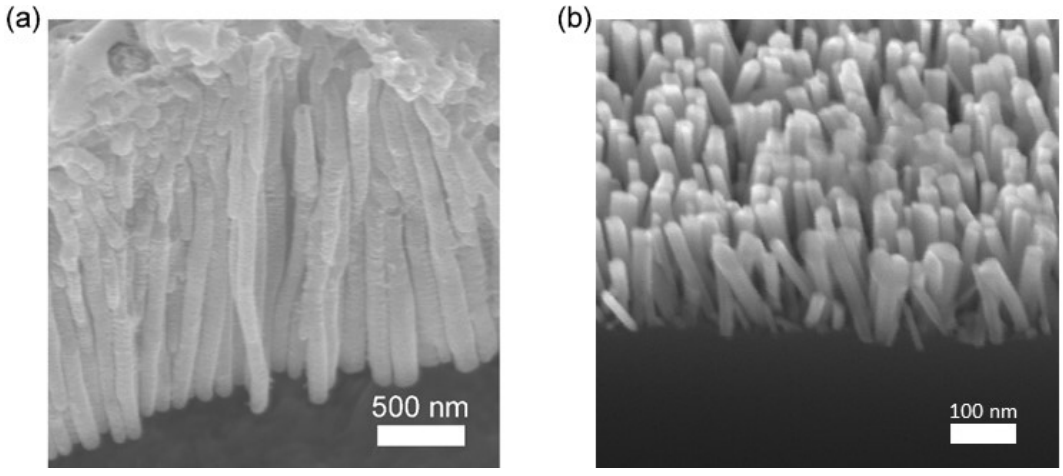

Figure 4.3 SEM characterizations of the photoelectrodes. (a) Ta_3N_5 nanotubes; (b) GaN nanowires.

4.3.2 Evaluation of the alignment of the electronic energies

Guided by these considerations, we next evaluate the alignment of the electronic energies of the various components of the system. On the anode side, it is desired to have a more positive potential than the formal oxidation potential of $Fe(CN)_6^{4-}$ (+0.5 V vs. NHE). As shown in **Figure 4.4**, the valence band edge position of Ta_3N_5 based on literature reports and our own measurements is indeed more positive.[39,43] On the cathode side, it is desired to have a more negative potential than the formal reduction potential of 2,6-DHAQ (-0.7 V vs. NHE; **Figure 4.5**), which is satisfied by the conduction band edge position of GaN. The charge flow under illumination (during recharge) is schematically illustrated in **Figure 4.4**, where photogenerated holes migrate to the surface of Ta_3N_5 to oxidize $K_4[Fe(CN)_6]$ to $K_3[Fe(CN)_6]$, and photogenerated electrons inject from Si to GaN to reduce 2,6-DHAQ to 2,6-reDHAQ (anthracene-2,6,9,10-tetrakis(olate)).[36] The net result of the process is that the energy delivered by light is effectively harvested by the photoelectrodes and stored in $K_3[Fe(CN)_6]$ and 2,6-reDHAQ in the form of positive and negative charges. When needed, the system can be discharged by reversing athe redox reactions on carbon paper electrodes.

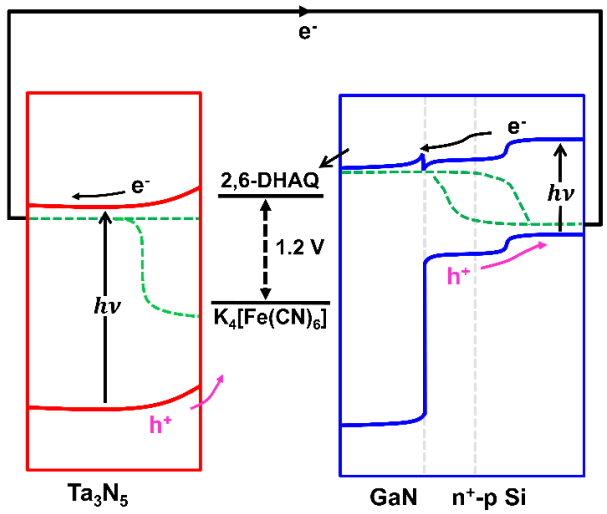

Figure 4.4 The energy band diagram under illumination showing the charge separation and flow charts of the system.

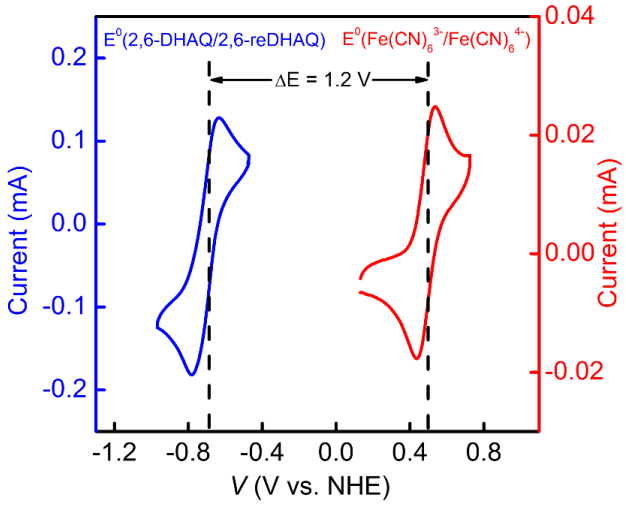

Figure 4.5 CV of 20 mM 2,6-DHAQ in pH 14 KOH solution (blue curve) and 2 mM $K_4[Fe(CN)_6]$ in pH 12 KOH solution (red curve) scanned at 100 mV/s on a glassy carbon electrode.

4.3.3 Assessment of the stability and light absorption of the electrolytes

With the suitability of the photoelectrodes established, we next assess the stability of the electrolytes, including the redox pairs. Previous research by Gordon and co-workers strong support that the $K_4Fe(CN)_6$ and 2,6-DHAQ electrolyte system exhibits outstanding chemical and electrochemical stabilities in 1 M KOH.[36] The key difference between previous approaches and the present work is the introduction of light. As such, we are most concerned with the stability of the system under illumination. For this purpose, we compared the portion of the electrolyte containing 2,6-DHAQ before and after 10 hr illumination (100 mW/cm^2, AM 1.5 simulated solar light) by proton nuclear magnetic resonance (^{1}H NMR) and found no measureable difference (**Figure 4.6**). The result supports that 2,6-DHAQ features outstanding stability with or without illumination. The light absorption by $K_4Fe(CN)_6$, on the other hand, presented a minor challenge. It was discovered that at pH 14 ($K_4Fe(CN)_6$ concentration >0.1 M), precipitation formed within the solution after <5 min of illumination. By comparison, no precipitation was observed for the same solution in dark up to 7 days of continuous electrochemical measurements. The phenomenon is consistent with previous reports.[36] While the detailed mechanisms of this light-induced precipitation remain unknown, it was found that the issue can be circumvented by reducing the pH to 12. No precipitation was observed up to 15 hr of illumination for a concentration up to 0.4 M. It is noted that because the formal oxidation potential of $K_4Fe(CN)_6$ is pH independent, the change of the pH does not lead to reduction of the cell voltage when combined with 2,6-DHAQ.

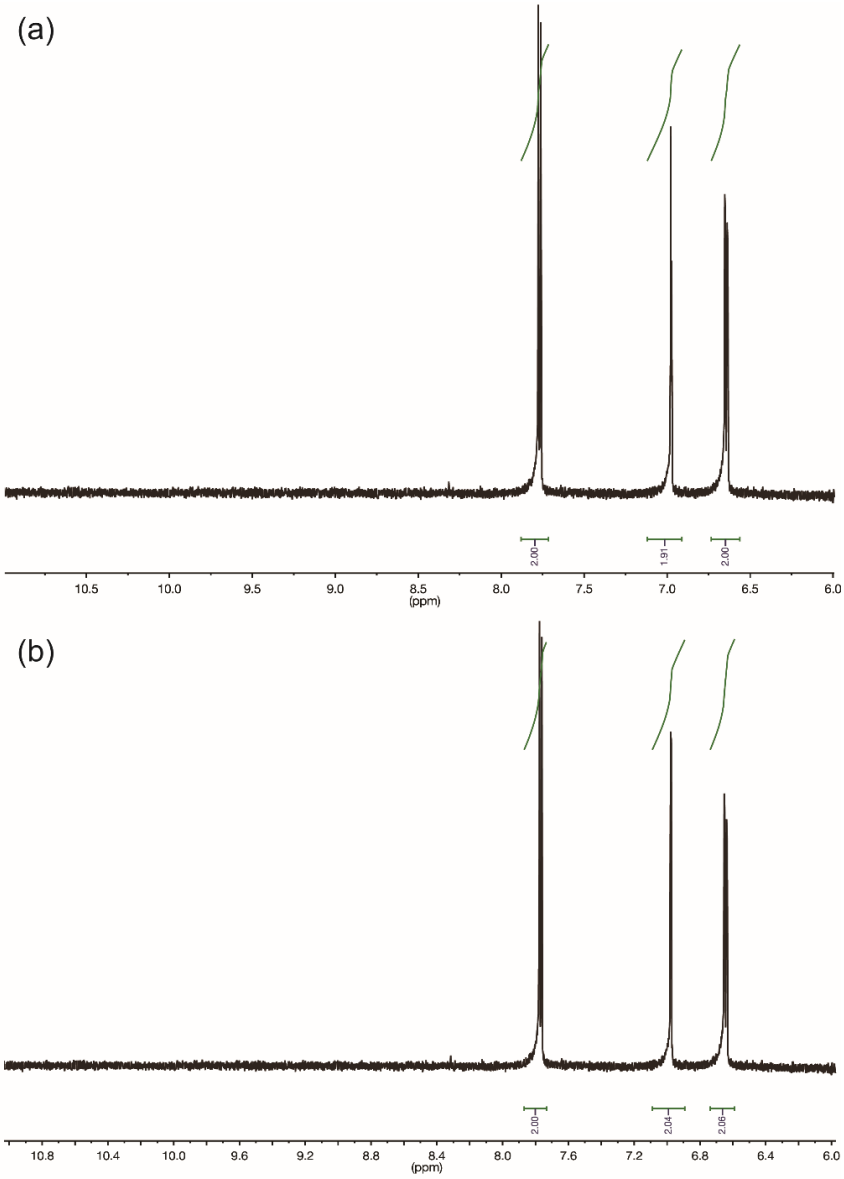

Figure 4.6 NMR spectrum of 2,6-DHAQ solution before (a) and after (b) 10 hr illumination.

Another issue which had to be addressed was the light absorption by the electrolyte (**Figure 4.7**), which would reduce the light intensity reaching the photoelectrode and, hence, the efficiency of the system. Our strategy was to minimize the optical path by pressing the photoelectrode close to the transparent window. Additionally, the light intensity was calibrated at the position where the photoelectrodes were placed in the solution using an immersed photodiode to compensate for the lost photons. As a result, the reported intensity (100 mW/cm^2) reflects the true intensity of light absorbed by the photoelectrodes, although spectra correction to compensate for electrolyte absorption was not conducted.

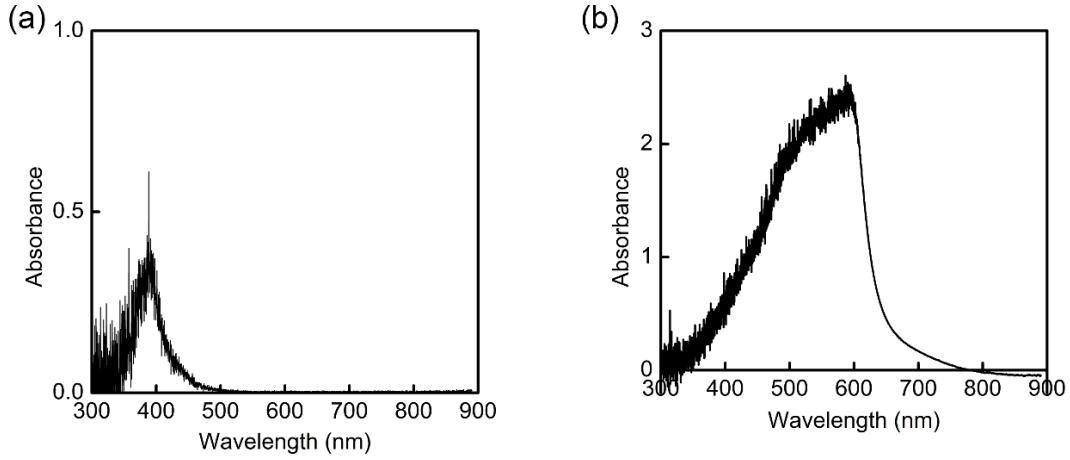

Figure 4.7 UV-vis absorption spectrum the electrolytes (a) 0.1 M $K_4[Fe(CN)_6]$; (b) 25 mM 2,6-DHAQ.

4.3.4 Photoelectrochemical performance of the photoanode and the photocathode

In **Figure 4.8**, the photoelectrochemical (PEC) data of the photoanode and the photocathode is presented. Several features of this set of data are worth highlighting. First, it can be seen from **Figure 4.8a** that the saturation current of the photoanode depends on the redox concentration. This feature is understood as the dependence of the saturation current on the mass-transport.[44] When the concentration of $K_4Fe(CN)_6$ is greater than 0.1 M, the saturation current reaches a maximum of up to ca. 12 mA/cm^2, which is limited by the photogenerated hole concentration in Ta_3N_5. For optimum performance, it is beneficial to use a high concentration of $K_4Fe(CN)_6$, to ensure all photogenerated charges can be readily collected. It is noted that the solubility of $K_4Fe(CN)_6$ in alkaline solutions limits the concentration to ca. 0.4 M. Similarly, the saturation current of the photocathode depends on the concentration of 2,6-DHAQ (**Figure 4.8c**), and the highest concentration as limited by its solubility is 0.4 M. Noted that the pH of 2,6-DHAQ solution needs to be kept at 14 to achieve an appreciable 2,6-DHAQ concentration. Second, both systems feature reasonable stability, with the photoanode performance decayed 10.9% (from 10.1 mA/cm^2 to 9.0 mA/cm^2 in 15 hr; **Figure 4.8b**) and the photocathode decayed 33.3% (from -40.5 mA/cm^2 to -27.0 mA/cm^2 in 5 hr; **Figure 4.8d**). It is noted that a thin (ca. 25 nm) TiO_2 passivation layer was already deposited on the GaN/Si photocathode by atomic layer deposition (ALD) to improve its stability.[41] Further enhancement of stability requires the improvement of the uniformity and optimization of the thickness of TiO_2 surface protection layer or the exploration of other surface passivation layers and/or cocatalysts.[45] Nonetheless, the performance as shown in **Figure 4.8** is adequate for the proof-of-concept

demonstration as reported here. Third, the Ta_3N_5 photoanode performance decayed rapidly in the absence of $K_4Fe(CN)_6$ (current density dropped from 3.9 mA/cm^2 to 0.15 mA/cm^2 in <5 min). The results support that the observed performance in $K_4Fe(CN)_6$ corresponds to the oxidation of $K_4Fe(CN)_6$ but not water oxidation. The observation is consistent with our recent report on the system.[39] Similarly, no activity was measured on the GaN/Si photocathode in the absence of 2,6-DHAQ, supporting that hydrogen evolution does not contribute to the measured performance as shown in **Figure 4.8c** and **4.8d**. Additionally, the cyclic voltammetries of both photoelectrodes in the presence of redox pairs display the obvious redox peaks, which are specific to the desired redox reactions instead of water splitting (**Figure 4.9**). Lastly, it is noted that if the photovoltage is defined as the difference between the on-set potential and the formal oxidation (or reduction) potential of the redox pairs, a photovoltage of 0.8 V was measured on the Ta_3N_5 photoanode and 0.6 V was measured on the GaN/Si photocathode.[46] The combined cell voltage (1.4 V) is slightly lower than the predicted 1.5 V from open circuit potential measurements. Possible reasons include the decrease of Ta_3N_5 photovoltage caused by the positive shift of the conduction band edge of Ta_3N_5 in pH 12 compared to pH 14 (59 mV/pH unit; **Figure 4.10**).[27,31]

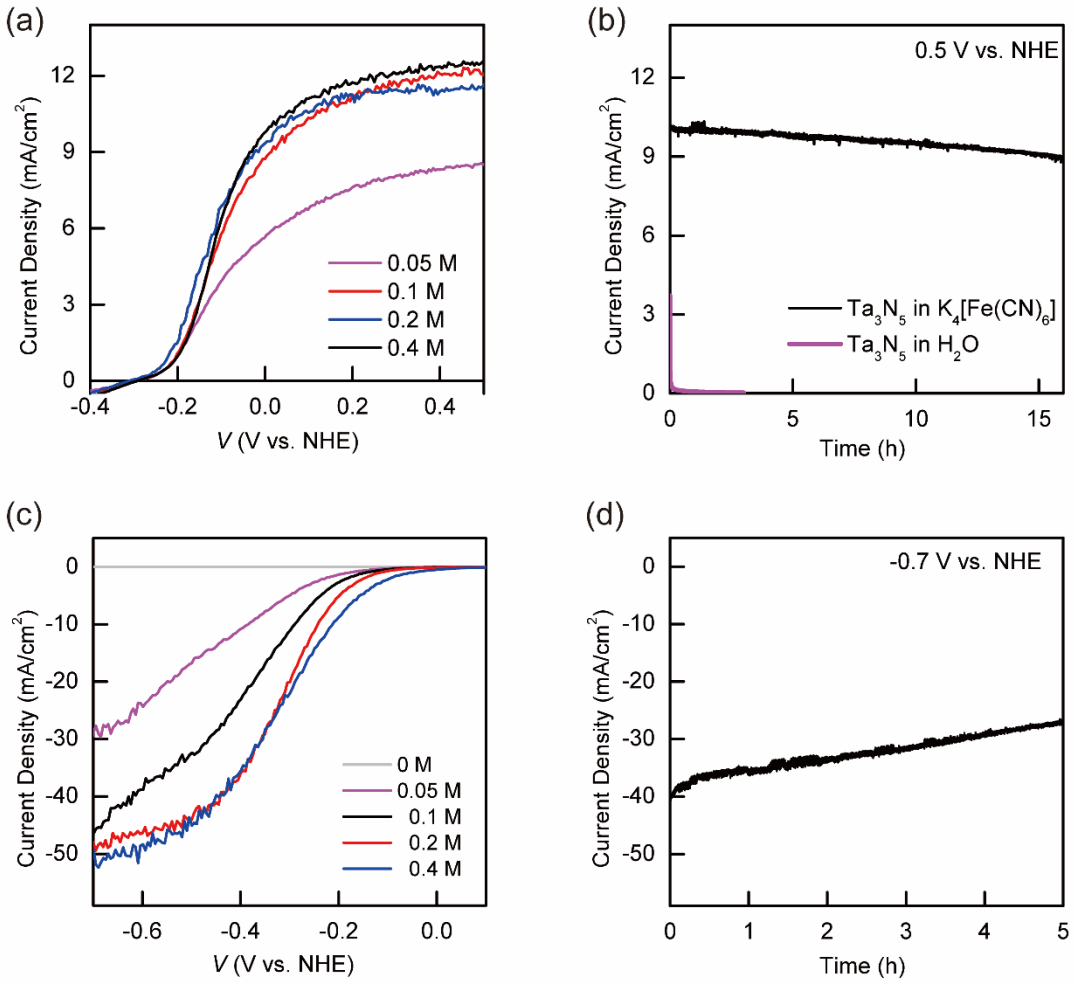

Figure 4.8 Photoelectrochemical performance of the system. (a) J-V curves of Ta_3N_5 photoanode over different concentrations of $K_4[Fe(CN)_6]$ in KOH solution (pH 12). (b) Chronoamperometry of Ta_3N_5 for PEC oxidation in 0.4 M $K_4[Fe(CN)_6]$/KOH solution in comparison to KOH solution (pH 12). (c) J-V curves of GaN/Si photocathode over different concentrations of 2,6-DHAQ in KOH solution (pH 14). (d) Chronoamperometry of GaN/Si for PEC reduction in 0.1 M 2,6-DHAQ/KOH solution (pH 14).

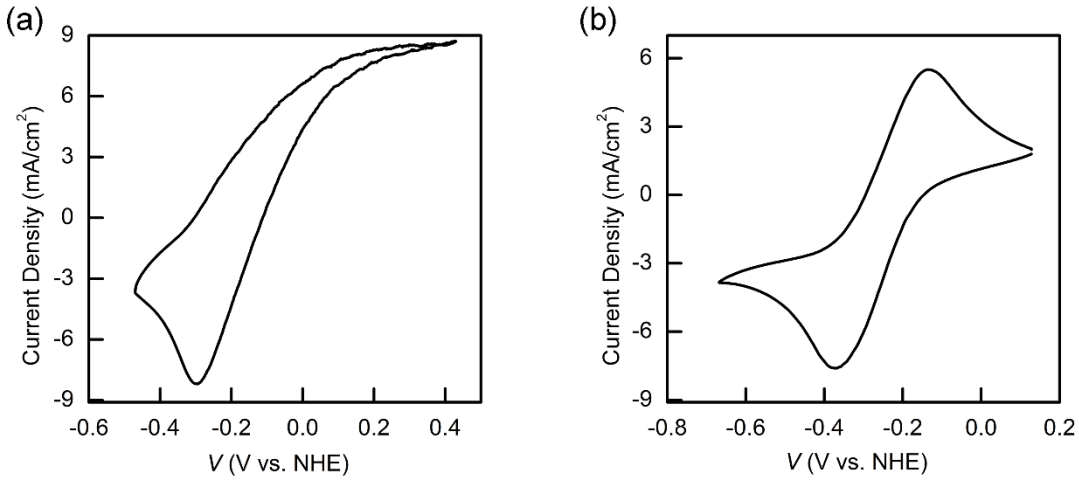

Figure 4.9 CVs of the photoelectrodes in the redox electrolytes (a) Ta_3N_5 in 0.4 M $K_4[Fe(CN)_6]$/KOH solution (pH 12), scan rate: 100 mV/s, scan direction: from negative to positive, then to negative again; (b) TiO_2/GaN/Si in 0.025 M 2,6-DHAQ/KOH solution (pH 14, unstirred), scan rate: 20 mV/s, scan direction: from positive to negative, then to positive again.

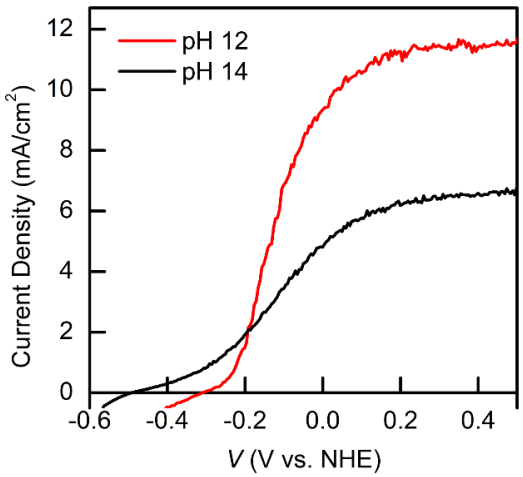

Figure 4.10 J-V curves of Ta_3N_5 in 0.4 M $K_4[Fe(CN)_6]$/KOH solution with different pH values.

More detailed PEC characterizations are presented in **Figure 4.11**, where it is evaluated whether mass transport or charge transfer is the limiting factor for both the photoanode and the photocathode. As shown in **Figure 4.11a**, while the saturation current for the Ta_3N_5 photoanode does increase with the stirring speed, the dependence is relatively insignificant. For instance, the saturation current density only increased 14.7% (from 10.2 mA/cm^2 to 11.7 mA/cm^2) when the system was changed from without stirring to a maximum of 1100 rpm. The result suggests that mass-transport of $K_4Fe(CN)_6$ is not a limiting factor in defining the overall PEC performance of the photoanode, which is also supported by the chopped light J-V study (**Figure 4.12**). Important to this discussion, a near linear dependence was observed of the saturation current on the light intensity (5.2 mA/cm^2 for 50 mW/cm^2; 11.7 mA/cm^2 for 100 mW/cm^2; 16.9 mA/cm^2 for 150 mW/cm^2; and 26.9 mA/cm^2 for 200 mW/cm^2; **Figure 4.11b**). It is worth noting that the saturation photocurrents approach the theoretical photocurrent densities at the corresponding light intensities, which supports that both the mass transport of $K_4Fe(CN)_6$ from the bulk solution to Ta_3N_5 surface and the $Ta_3N_5/K_4Fe(CN)_6$ interface charge transfer are not limiting factors in defining the overall PEC performance of Ta_3N_5.[42] By contrast, the near linear dependence of the saturation current of the GaN/Si photocathode on the stirring speed (**Figure 4.11c**) and the weak correlation of the saturation current with the light intensity above 100 mW/cm^2 (**Figure 4.11d**) suggest that mass transport of 2,6-DHAQ is a limiting factor. In addition, the obvious photocurrent spikes in the GaN/Si chopped light J-V curve also indicated the limited mass transfer of 2,6-DHAQ (**Figure 4.12**). Fluidic management is needed to actualize the full potentials of the photocathode system. Further

enhancement of the mass transfer properties of the quinone-based redox pairs requires a fundamental understanding of their diffusion properties and the exploration of new types of quinone-based redox pairs.[47-50] Moreover, the photovoltage (0.6 V) and the photocurrent density (40 mA/cm^2) at -0.7 V vs. NHE measured on the photocathode are close to what is theoretically possible for Si and comparable to what was measured on the GaN/Si system for reactions such as hydrogen evolution reaction (HER) or CO_2 reduction.[40,51] While encouraging and proving the feasibility of using the system for the photoreduction of 2,6-DHAQ, the relatively poor charge collection as shown in the poor fill factors if it were characterized as a photovoltaic device indicate that future research should focus on studying the benefit of applying co-catalyst such as carbon.

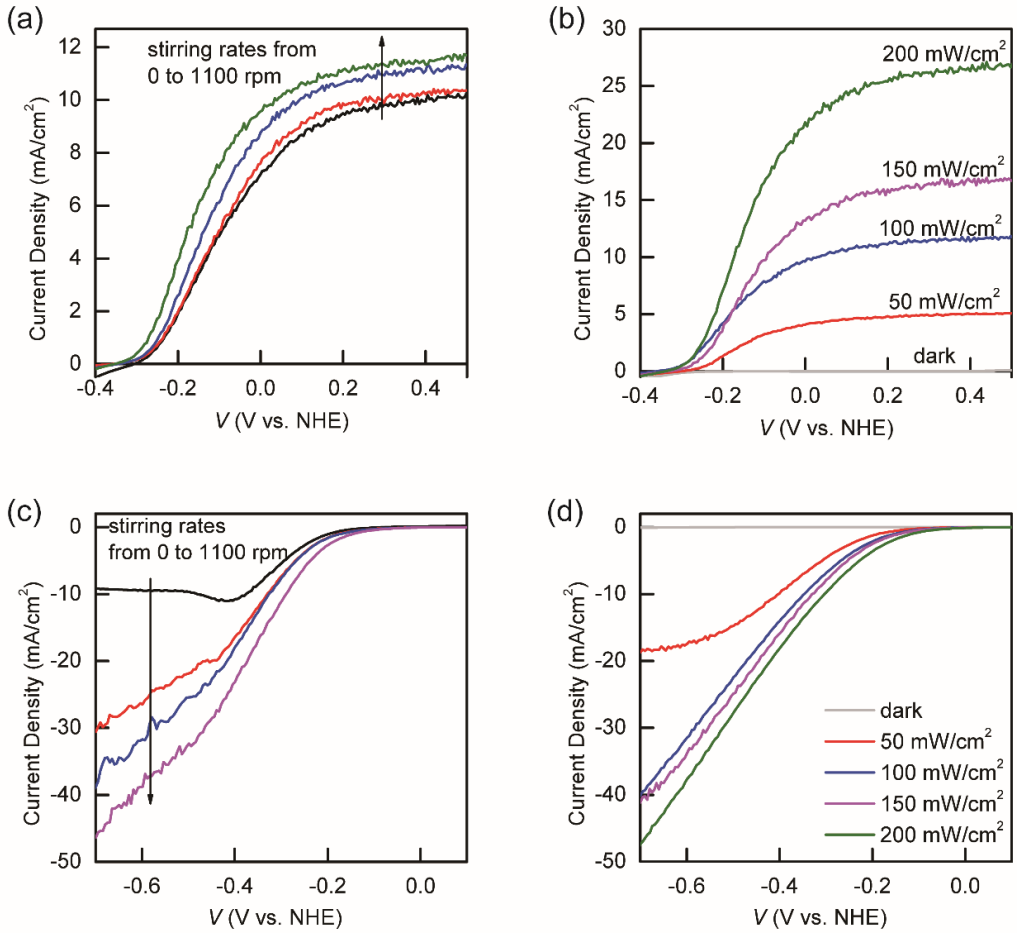

Figure 4.11 PEC characterization with different stirring rates and different light intensities. (a) J-V curves of Ta_3N_5 photoanode in 0.4 M $K_4[Fe(CN)_6]$/KOH solution (pH 12) at different stirring speeds, (b) and under different light intensities. (c) J-V curves of TiO_2/GaN/Si photocathode in 0.1 M 2,6-DHAQ/KOH solution (pH 14) at different stirring speeds, (d) and under different light intensities.

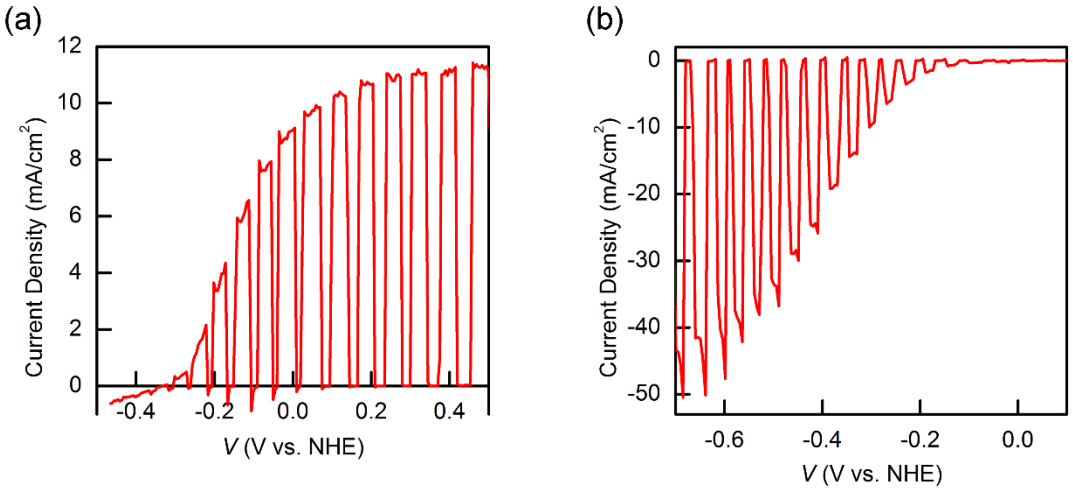

Figure 4.12 Chopped light J-V studies of the photoelectrodes in redox electrolytes. (a) Ta_3N_5 in 0.4 M $K_4Fe(CN)_6$/KOH solution (pH 12); (b) TiO_2/GaN/Si in 0.1 M 2,6-DHAQ/KOH solution (pH 14).

4.3.5 Electrochemical performances of the 2,6-DHAQ/K_4[Fe(CN)$_6$] battery

Next, the electrochemical performances of the 2,6-DHAQ/K4[Fe(CN)$_6$] battery was studied. The 2,6-DHAQ (pH 14)/$K_4Fe(CN)_6$ (pH 12) battery was built using 0.4 M $K_4Fe(CN)_6$ (pH 12 KOH) catholyte and 0.1 M 2,6-DHAQ (pH 14 KOH) anolyte, a Nafion 212 membrane, and two carbon paper electrodes. The lower Colombic efficiency of our battery compared to 2,6-DHAQ (pH 14)/$K_4Fe(CN)_6$ (pH 14) battery indicates that the proton concentration gradient in our battery does present a challenge in terms of proton management and the associated chemical potential drop at the membrane (**Figure 4.13a & 4.13b**). These problems are expected to be solved by the application of other types of

membranes such as bipolar ones.[52] The measured near linear relationship of the current ramp study indicates that the iR drop of the overall cell rather than the kinetics of the redox species on electrodes is the main reason for the observed overpotential (**Figure 4.13c**). The Nyquist plot from EIS measurements shows that the high frequency area-specific resistance is as high as 38.3 Ω cm^2 (**Figure 4.13d**). This high resistance is mainly due to our H-cell configuration (**Figure 4.1**) and is the main limitation for our battery performance.

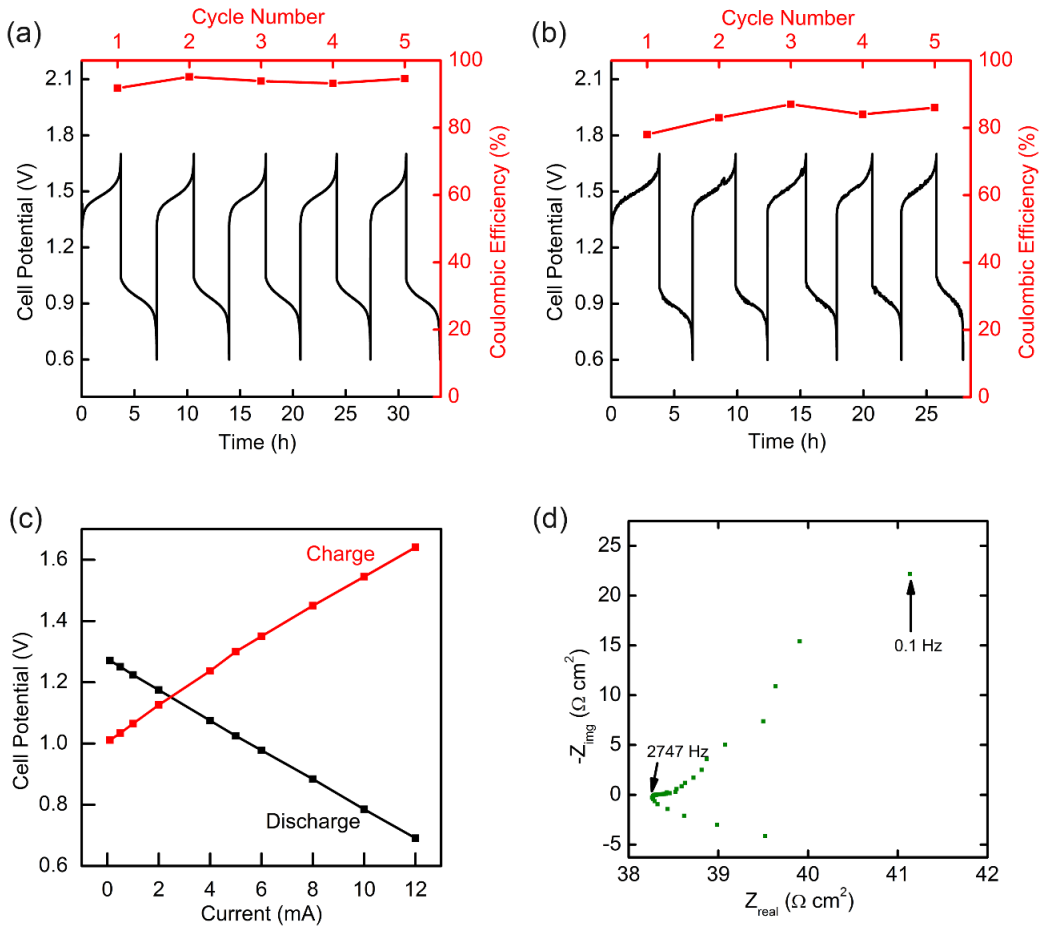

Figure 4.13 Electrochemical performance of 2,6-DHAQ/K4Fe(CN)6 battery (a) Cycling performance of the 2,6-DHAQ (pH 14)/K4Fe(CN)6 (pH 14) battery, (b) and the 2,6-DHAQ

(pH 14)/K4Fe(CN)6 (pH 12) battery. (c) charge/discharge voltage vs the current studies (electrode area: 1 cm2). (d) Nyquist plot of Electrochemical Impedance Spectrum in fully discharged electrolytes at open-circuit potential

4.3.6 Investigation of the Integrated System

Our last task for this body of research was to investigate the integrated system. We approached the problem in two steps. During the first step, we compared the photooxidation and photoreduction performance as measured separately, and the data are plotted in **Figure 4.14a**. As is seen, when characterized separately in a 3-electrode configuration, the two curves overlap to yield an intersection point where 5 mA/cm^2 photocurrent is expected. Note that here each photoelectrode was illuminated by light of the same intensity (100 mW/cm^2). By assuming the equilibrium potential of 1.2 V, it is estimated that the overall solar-to-chemical energy conversion efficiency of 3.0%. Such an efficiency is high when compared with solar-to-hydrogen conversion efficiencies in similar solar water splitting systems.[53-55] It is also high among photo-rechargeable redox batteries.[4,28,29] Given that in principle the two photoelectrodes can be arranged in tandem, there is plenty of room to further improve the efficiency in the future.[56]

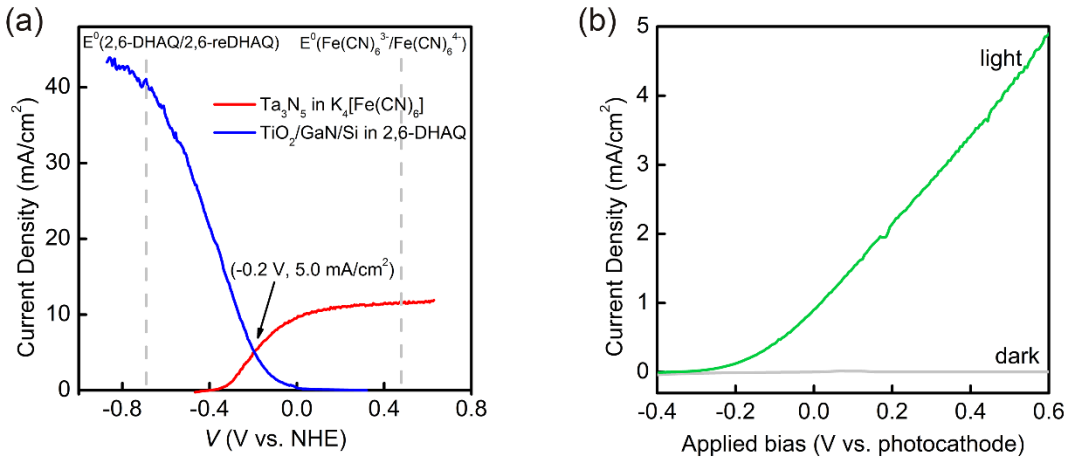

Figure 4.14 Integration of the Ta_3N_5 photoanode and the GaN/Si photocathode. (a) The overlay of the reduction and oxidation curves. The dotted vertical lines represent the formal reduction and oxidation potentials of the redox system. (b) J-V characteristics of a two-electrode configuration under light (green) and dark (gray) conditions. The projected areas of Ta_3N_5 and TiO_2/GaN/Si are 0.78 cm^2 and 0.54 cm^2, respectively.

During the second step, the system was studied in a truly integrated fashion by connecting the two photoelectrodes in a single cell (separated by a Nafion membrane). As shown in **Figure 4.14b**, a linear sweep voltammogram of the dual-photoelectrode shows an average photocurrent density of 0.93 mA/cm^2 at V_{app}= 0 V, indicating that the unassisted photocharge could be achieved in a single cell experimentally. Note that the photocurrent is normalized to the average working area due to the different areas of the two photoelectrodes. During the photocharge process, the photoelectrodes are directly short-

circuited without external bias and the photocurrent-time curve is monitored by a potentiostat. When the cell was discharged using two carbon paper electrodes independent of the photoelectrodes, a high discharge voltage (~1 V) and a modest capacity (200 mAh/L) were obtained, which corresponded to 22% of the recharge capacity (**Figure 4.15**). Separate electrochemical characterizations suggest that the low Coulombic efficiency may be due to the low current densities. As detailed in **Figure 4.16a**, >92% Coulombic efficiencies were consistently obtained when the charge current density was at 5 mA/cm^2 or higher. At 0.5 mA/cm^2, however, the efficiency was reduced to 35% (**Figure 4.16b**). Thus it is concluded that it is not specific to the photocharge but an inherent issue to the system at low charge current densities. Possible reasons include the crossover of the active material through the membrane and the aggravated side reactions such as oxygen reduction reaction at low current densities. It is envisioned that switching from the stirred H-cell design (**Figure 4.1**) to a practical flow battery configuration for better deaeration of 2,6-DHAQ redox electrolyte and improved electrolyte mass transfer could further improve the Coulombic efficiency. These strategies may be combined with efforts focused on improving the photocharge performance for significantly improved overall photocharge-discharge performance in the future.

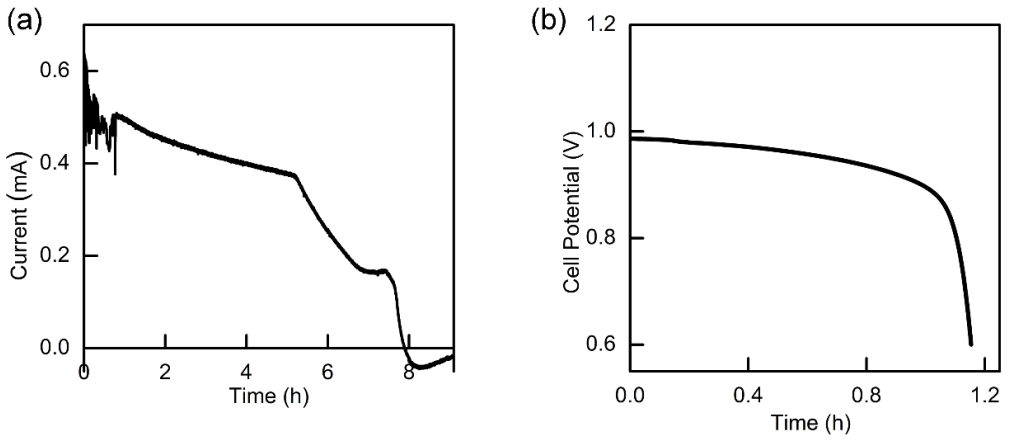

Figure 4.15 Unassisted photocharge and discharge performance of the 2,6-DHAQ/ $K_4[Fe(CN)_6]$ battery (a) photocurrent-time data during photocharge process (b) discharge voltage-time profile after photocharge with the applied current of 0.5 mA (current density: 0.5 mA/cm^2).

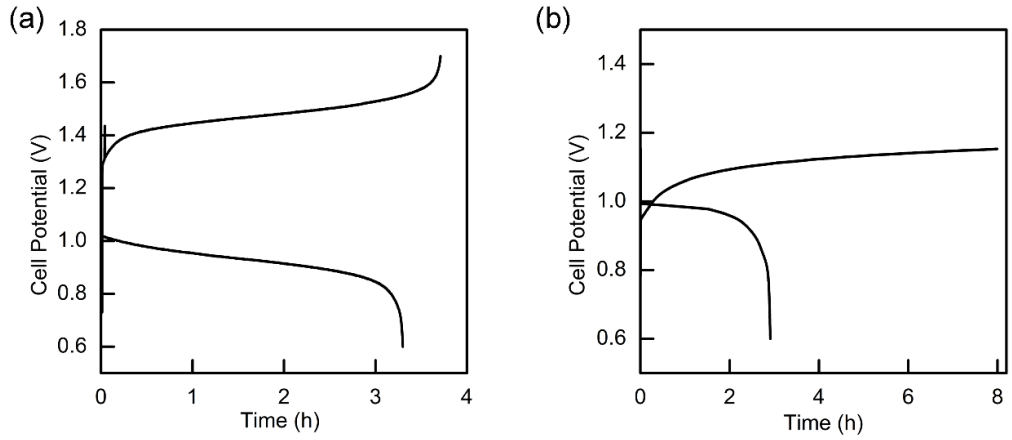

Figure 4.16 Electrochemical performance of 2,6-DHAQ/$K_4[Fe(CN)_6]$ battery at different applied current conditions (both catholyte and anolyte are in pH 14 KOH solution) (a) 5 mA/cm^2 applied current density; (b) 0.5 mA/cm^2 applied current density.

4.4 Conclusions

In conclusion, we have successfully demonstrated a 1.2 V solar rechargeable redox battery based on the integration of Ta_3N_5 nanotube photoanode and GaN nanowire/Si photocathode with the 2,6-DHAQ/$K_4[Fe(CN)_6]$ redox pairs. The good solar-to-charge conversion performance of the individual photoelectrodes enabled the measurement of high photovoltages (>1.4 V), making it possible to photorecharge the redox battery without externally applied potentials. The optimal solar-to-chemical conversion efficiency was estimated up to 3.0%. We envision that this efficiency would be readily improved when the two photoelectrodes are arranged in tandem. Other competing PEC reactions such as water splitting are negligible in our system, even though the redox potentials of $Fe(CN)_6^{3-}$ /$Fe(CN)_6^{4-}$ and 2,6-DHAQ/2,6-reDHAQ are close to water oxidation and reduction potentials. The integrated battery was successfully photocharged and then discharged with a stable voltage output of up to 1 V. Our demonstration opens up a new door to photochargeable high-voltage redox (flow) batteries.

4.5 References

[1] Lewis, N. S., Research opportunities to advance solar energy utilization. *Science* **2016,** *351*, 353.
[2] Dunn, B.; Kamath, H.; Tarascon, J.-M., Electrical Energy Storage for the Grid: A Battery of Choices. *Science* **2011,** *334*, 928.
[3] Grätzel, M., Photoelectrochemical cells. *Nature* **2001,** *414*, 338.
[4] Schmidt, D.; Hager, M. D.; Schubert, U. S., Photo-Rechargeable Electric Energy Storage Systems. *Adv. Energy Mater.* **2016,** *6*, 1500369.
[5] Guo, W.; Xue, X.; Wang, S.; Lin, C.; Wang, Z. L., An Integrated Power Pack of Dye-Sensitized Solar Cell and Li Battery Based on Double-Sided TiO2 Nanotube Arrays. *Nano Lett.* **2012,** *12*, 2520.
[6] Xu, J.; Chen, Y.; Dai, L., Efficiently photo-charging lithium-ion battery by perovskite solar cell. *Nat. Commun.* **2015,** *6*, 8103.
[7] Yang, Z.; Zhang, J.; Kintner-Meyer, M. C. W.; Lu, X.; Choi, D.; Lemmon, J. P.; Liu, J., Electrochemical Energy Storage for Green Grid. *Chem. Rev.* **2011,** *111*, 3577.
[8] Kim, D.; Sakimoto, K. K.; Hong, D.; Yang, P., Artificial Photosynthesis for Sustainable Fuel and Chemical Production. *Angew. Chem. Int. Ed.* **2015,** *54*, 3259.
[9] Zhang, P.; Gao, L.; Song, X.; Sun, J., Micro-and Nanostructures of Photoelectrodes for Solar‐Driven Water Splitting. *Adv. Mater.* **2015,** *27*, 562.
[10] Asadi, M.; Kim, K.; Liu, C.; Addepalli, A. V.; Abbasi, P.; Yasaei, P.; Phillips, P.; Behranginia, A.; Cerrato, J. M.; Haasch, R.; Zapol, P.; Kumar, B.; Klie, R. F.; Abiade, J.; Curtiss, L. A.; Salehi-Khojin, A., Nanostructured transition metal dichalcogenide electrocatalysts for CO_2 reduction in ionic liquid. *Science* **2016,** *353*, 467.
[11] Liu, C.; Colón, B. C.; Ziesack, M.; Silver, P. A.; Nocera, D. G., Water splitting-biosynthetic system with CO_2 reduction efficiencies exceeding photosynthesis. *Science* **2016,** *352*, 1210.
[12] Schreier, M.; Curvat, L.; Giordano, F.; Steier, L.; Abate, A.; Zakeeruddin, S. M.; Luo, J.; Mayer, M. T.; Grätzel, M., Efficient photosynthesis of carbon monoxide from CO2 using perovskite photovoltaics. *Nat. Commun.* **2015,** *6*, 7326.
[13] Chalk, S. G.; Miller, J. F., Key challenges and recent progress in batteries, fuel cells, and hydrogen storage for clean energy systems. *J. Power Sources* **2006,** *159*, 73.
[14] Seitz, L. C.; Dickens, C. F.; Nishio, K.; Hikita, Y.; Montoya, J.; Doyle, A.; Kirk, C.; Vojvodic, A.; Hwang, H. Y.; Norskov, J. K.; Jaramillo, T. F., A highly active and stable $IrO_x/SrIrO_3$ catalyst for the oxygen evolution reaction. *Science* **2016,** *353*, 1011.
[15] Cabán-Acevedo, M.; Stone, M. L.; Schmidt, J. R.; Thomas, J. G.; Ding, Q.; Chang, H.-C.; Tsai, M.-L.; He, J.-H.; Jin, S., Efficient hydrogen evolution catalysis using ternary pyrite-type cobalt phosphosulphide. *Nat. Mater.* **2015,** *14*, 1245.
[16] Gewirth, A. A.; Thorum, M. S., Electroreduction of Dioxygen for Fuel-Cell Applications: Materials and Challenges. *Inorg. Chem.* **2010,** *49*, 3557.
[17] Pellow, M. A.; Emmott, C. J. M.; Barnhart, C. J.; Benson, S. M., Hydrogen or batteries for grid storage? A net energy analysis. *Energy Environ. Sci.* **2015,** *8*, 1938.

[18] Soloveichik, G. L., Flow Batteries: Current Status and Trends. *Chem. Rev.* **2015,** *115*, 11533.
[19] Sharon, M.; Veluchamy, P.; Natarajan, C.; Kumar, D., Solar rechargeable battery-principle and materials. *Electrochim. Acta* **1991,** *36*, 1107.
[20] Hodes, G.; Manassen, J.; Cahen, D., Photoelectrochemical energy conversion and storage using polycrystalline chalcogenide electrodes. *Nature* **1976,** *261*, 403.
[21] Liu, P.; Cao, Y. l.; Li, G. R.; Gao, X. P.; Ai, X. P.; Yang, H. X., A Solar Rechargeable Flow Battery Based on Photoregeneration of Two Soluble Redox Couples. *ChemSusChem* **2013,** *6*, 802.
[22] Yan, N. F.; Li, G. R.; Gao, X. P., Solar rechargeable redox flow battery based on Li2WO4/LiI couples in dual-phase electrolytes. *J. Mater. Chem. A* **2013,** *1*, 7012.
[23] Wei, Z.; Liu, D.; Hsu, C.; Liu, F., All-vanadium redox photoelectrochemical cell: An approach to store solar energy. *Electrochem. Commun.* **2014,** *45*, 79.
[24] Li, N.; Wang, Y.; Tang, D.; Zhou, H., Integrating a Photocatalyst into a Hybrid Lithium–Sulfur Battery for Direct Storage of Solar Energy. *Angew. Chem. Int. Ed.* **2015,** *54*, 9271.
[25] Kim, G.; Oh, M.; Park, Y., Solar-rechargeable battery based on photoelectrochemical water oxidation: Solar water battery. *Sci. Rep.* **2016,** *6*, 33400.
[26] Yu, M.; Ren, X.; Ma, L.; Wu, Y., Integrating a redox-coupled dye-sensitized photoelectrode into a lithium–oxygen battery for photoassisted charging. *Nat. Commun.* **2014,** *5*, 5111.
[27] McCulloch, W. D.; Yu, M.; Wu, Y., pH-Tuning a Solar Redox Flow Battery for Integrated Energy Conversion and Storage. *ACS Energy Lett.* **2016,** *1*, 578.
[28] Liao, S.; Zong, X.; Seger, B.; Pedersen, T.; Yao, T.; Ding, C.; Shi, J.; Chen, J.; Li, C., Integrating a dual-silicon photoelectrochemical cell into a redox flow battery for unassisted photocharging. *Nat. Commun.* **2016,** *7*, 11474.
[29] Li, W.; Fu, H. C.; Li, L.; Cabán−Acevedo, M.; He, J. H.; Jin, S., Integrated Photoelectrochemical Solar Energy Conversion and Organic Redox Flow Battery Devices. *Angew. Chem. Int. Ed.* **2016,** *55*, 13104.
[30] Azevedo, J.; Seipp, T.; Burfeind, J.; Sousa, C.; Bentien, A.; Araújo, J. P.; Mendes, A., Unbiased solar energy storage: Photoelectrochemical redox flow battery. *Nano Energy* **2016,** *22*, 396.
[31] Wedege, K.; Azevedo, J.; Khataee, A.; Bentien, A.; Mendes, A., Direct Solar Charging of an Organic–Inorganic, Stable, and Aqueous Alkaline Redox Flow Battery with a Hematite Photoanode. *Angew. Chem. Int. Ed.* **2016,** *55*, 7142.
[32] Yu, M.; McCulloch, W. D.; Huang, Z.; Trang, B. B.; Lu, J.; Amine, K.; Wu, Y., Solar-powered electrochemical energy storage: an alternative to solar fuels. *J. Mater. Chem. A* **2016,** *4*, 2766.
[33] Sivula, K.; van de Krol, R., Semiconducting materials for photoelectrochemical energy conversion. *Nat. Rev. Mater.* **2016,** *1*, 15010.
[34] Fujishima, A.; Honda, K., Electrochemical Photolysis of Water at a Semiconductor Electrode. *Nature* **1972,** *238*, 37.

[35] Walter, M. G.; Warren, E. L.; McKone, J. R.; Boettcher, S. W.; Mi, Q.; Santori, E. A.; Lewis, N. S., Solar Water Splitting Cells. *Chem. Rev.* **2010,** *110*, 6446.
[36] Lin, K.; Chen, Q.; Gerhardt, M. R.; Tong, L.; Kim, S. B.; Eisenach, L.; Valle, A. W.; Hardee, D.; Gordon, R. G.; Aziz, M. J.; Marshak, M. P., Alkaline quinone flow battery. *Science* **2015,** *349*, 1529.
[37] Kibria, M. G.; Mi, Z., Artificial photosynthesis using metal/nonmetal-nitride semiconductors: current status, prospects, and challenges. *J. Mater. Chem. A* **2016,** *4*, 2801.
[38] Kibria, M. G.; Qiao, R.; Yang, W.; Boukahil, I.; Kong, X.; Chowdhury, F. A.; Trudeau, M. L.; Ji, W.; Guo, H.; Himpsel, F. J.; Vayssieres, L.; Mi, Z., Atomic−Scale Origin of Long−Term Stability and High Performance of p−GaN Nanowire Arrays for Photocatalytic Overall Pure Water Splitting. *Adv. Mater.* **2016,** *28*, 8388.
[39] He, Y.; Thorne, James E.; Wu, Cheng H.; Ma, P.; Du, C.; Dong, Q.; Guo, J.; Wang, D., What Limits the Performance of Ta_3N_5 for Solar Water Splitting? *Chem* **2016,** *1*, 640.
[40] Fan, S.; AlOtaibi, B.; Woo, S. Y.; Wang, Y.; Botton, G. A.; Mi, Z., High Efficiency Solar-to-Hydrogen Conversion on a Monolithically Integrated InGaN/GaN/Si Adaptive Tunnel Junction Photocathode. *Nano Lett.* **2015,** *15*, 2721.
[41] Dai, P.; Li, W.; Xie, J.; He, Y.; Thorne, J.; McMahon, G.; Zhan, J.; Wang, D., Forming Buried Junctions to Enhance the Photovoltage Generated by Cuprous Oxide in Aqueous Solutions. *Angew. Chem. Int. Ed.* **2014,** *53*, 13493.
[42] Liu, G.; Ye, S.; Yan, P.; Xiong, F.; Fu, P.; Wang, Z.; Chen, Z.; Shi, J.; Li, C., Enabling an integrated tantalum nitride photoanode to approach the theoretical photocurrent limit for solar water splitting. *Energy Environ. Sci.* **2016,** *9*, 1327.
[43] Chun, W.-J.; Ishikawa, A.; Fujisawa, H.; Takata, T.; Kondo, J. N.; Hara, M.; Kawai, M.; Matsumoto, Y.; Domen, K., Conduction and Valence Band Positions of Ta_2O_5, TaON, and Ta_3N_5 by UPS and Electrochemical Methods. *J. Phys. Chem. B* **2003,** *107*, 1798.
[44] Kageshima, Y.; Kumagai, H.; Hisatomi, T.; Minegishi, T.; Kubota, J.; Domen, K., Photoelectrochemical Solar Cells Consisting of a Pt-Modified CdS Photoanode and an $Fe(ClO_4)_2/Fe(ClO_4)_3$ Redox Shuttle in a Nonaqueous Electrolyte. *J. Phys. Chem. C* **2016,** *120*, 10781.
[45] Liu, R.; Zheng, Z.; Spurgeon, J.; Yang, X., Enhanced photoelectrochemical water-splitting performance of semiconductors by surface passivation layers. *Energy Environ. Sci.* **2014,** *7*, 2504.
[46] Zhou, X.; Liu, R.; Sun, K.; Papadantonakis, K. M.; Brunschwig, B. S.; Lewis, N. S., 570 mV photovoltage, stabilized n-Si/CoO_x heterojunction photoanodes fabricated using atomic layer deposition. *Energy Environ. Sci.* **2016,** *9*, 892.
[47] Yang, B.; Hoober-Burkhardt, L.; Wang, F.; Surya Prakash, G. K.; Narayanan, S. R., An Inexpensive Aqueous Flow Battery for Large-Scale Electrical Energy Storage Based on Water-Soluble Organic Redox Couples. *J. Electrochem. Soc.* **2014,** *161*, A1371.
[48] Ding, Y.; Li, Y.; Yu, G., Exploring Bio-inspired Quinone-Based Organic Redox Flow Batteries: A Combined Experimental and Computational Study. *Chem* **2016,** *1*, 790.
[49] Ding, Y.; Yu, G., A Bio-Inspired, Heavy-Metal-Free, Dual-Electrolyte Liquid Battery towards Sustainable Energy Storage. *Angew. Chem.* **2016,** *128*, 4850.

[50] Zhao, Y.; Ding, Y.; Li, Y.; Peng, L.; Byon, H. R.; Goodenough, J. B.; Yu, G., A chemistry and material perspective on lithium redox flow batteries towards high-density electrical energy storage. *Chem. Soc. Rev.* **2015,** *44*, 7968.
[51] Wang, Y.; Fan, S.; AlOtaibi, B.; Wang, Y.; Li, L.; Mi, Z., A Monolithically Integrated Gallium Nitride Nanowire/Silicon Solar Cell Photocathode for Selective Carbon Dioxide Reduction to Methane. *Chem. Eur. J.* **2016,** *22*, 8809.
[52] Weng, G.-M.; Li, C.-Y. V.; Chan, K.-Y., High Voltage Vanadium-Metal Hydride Rechargeable Semi-Flow Battery. *J. Electrochem. Soc.* **2013,** *160*, A1384.
[53] AlOtaibi, B.; Fan, S.; Vanka, S.; Kibria, M. G.; Mi, Z., A Metal-Nitride Nanowire Dual-Photoelectrode Device for Unassisted Solar-to-Hydrogen Conversion under Parallel Illumination. *Nano Lett.* **2015,** *15*, 6821.
[54] Jang, J.-W.; Du, C.; Ye, Y.; Lin, Y.; Yao, X.; Thorne, J.; Liu, E.; McMahon, G.; Zhu, J.; Javey, A.; Guo, J.; Wang, D., Enabling unassisted solar water splitting by iron oxide and silicon. *Nat. Commun.* **2015,** *6*, 7447.
[55] Liu, G.; Du, K.; Haussener, S.; Wang, K., Charge Transport in Two‐Photon Semiconducting Structures for Solar Fuels. *ChemSusChem* **2016,** *9*, 2878.
[56] Prévot, M. S.; Sivula, K., Photoelectrochemical Tandem Cells for Solar Water Splitting. *J. Phys. Chem. C* **2013,** *117*, 17879.